

Thermal and flow characteristics of nonequilibrium monatomic, diatomic, and polyatomic gases in cylindrical Couette flow based on second-order non-Navier–Fourier constitutive model

T. Chourushi¹, A. Rahimi², S. Singh³, O. Ejtehad⁴, T. K. Mankodi⁵, R. S. Myong^{1*}

¹ *School of Mechanical and Aerospace Engineering and ACTRC, Gyeongsang National University, Jinju, Gyeongnam 52828, South Korea*

² *Department of Engineering Science, University West, 461 86 Trollhättan, Sweden*

³ *School of Physical and Mathematical Sciences, Nanyang Technological University, 21 Nanyang Link 637371, Singapore*

⁴ *Supercomputing Modeling and Simulation Center, Korea Institute of Science and Technology Information (KISTI), Daejeon 305-806, South Korea*

⁵ *Department of Mechanical Engineering, Indian Institute of Technology Guwahati, Assam, 781039, India*

* Corresponding author: Tel: +82-55-772-1645. Email: myong@gnu.ac.kr.

Abstract: The thermal and flow characteristics of nonequilibrium monatomic, diatomic, and polyatomic gases in cylindrical Couette flow are investigated using first- and second-order Boltzmann–Curtiss-based constitutive models. The mixed modal discontinuous Galerkin scheme is used for solving the conservation laws in conjunction with the Maxwell velocity-slip and Smoluchowski temperature-jump boundary conditions. Also derived are new analytic solutions for compressible cylindrical Couette gas flow including the temperature profile, and they are used to verify the numerical scheme. Further, the second-order non-Navier–Fourier constitutive relations are derived for the cylindrical coordinates. Various abnormal behavior is found in the second-order constitutive model, such as non-zero normal stress and excess normal stress, non-zero tangential heat flux, and flattened pressure and density profiles. The physical mechanisms behind this abnormal behavior are found to be similar to the Knudsen layer in planar Couette gas flow, and the curvature of the cylindrical geometry does not affect the fundamental second-order physics. Moreover, two new abnormal mechanisms are found in diatomic and polyatomic gases: (i) the subtle interplay of excess normal stress (and bulk viscosity) with the nonlinear coupled constitutive relation, and (ii) the combined role of the bulk viscosity ratio and the specific heat ratio.

Keywords: Rarefied and microscale gases; heat transfer; diatomic and polyatomic gases; non-Navier-Fourier laws; slip and jump conditions

1. Introduction

Understanding the flow dynamics and thermal characteristics of gas flows is crucial when designing devices with rarefied gases near vacuum [1,2], vehicles flying at high altitude or in a low-density atmosphere such as that on Mars [3,4], microscale heat exchangers, motors, and sensors in microfluidics [5-11], and vapor deposition methods for semiconductors and displays [12,13]. Assessing the thermofluidic characteristics accurately enables efficient prediction of the system performance in these applications, such as the aerothermodynamic loads exerted on re-entry vehicles, the thermal management system in spacecraft, the thermofluidic performance in micro-electromechanical systems, and the deposition of nano-layers in organic light-emitting devices (OLED). In these applications, gas flows in channels, tubes, exchangers, motors, sensors, and ducts driven by the pressure and temperature gradients in the flow direction are common. The performance of shear-driven devices with moving components is also affected significantly by the rarefaction of gas [1,2,5,7].

Consequently, it is critical to model the molecular motion of rarefied gas particles close to solid surfaces, which is known as the Knudsen layer (or kinetic boundary layer) [14]. In the gaseous Knudsen layer, continuum assumptions based on no-slip and linear constitutive relations such as the Navier-Fourier laws may no longer be valid because the gas flow is no longer near a local thermodynamic equilibrium (LTE) [15-20]. Moreover, relative motion between multiple surfaces further complicates the problem because it introduces nonlinearity and nonisothermal behavior in the gas flow, which is known as the classical Couette flow problem [21,22].

Gaseous cylindrical Couette flow (CCF) is shown schematically in Fig. 1. A finite amount of gas (monatomic, diatomic, or polyatomic) is confined between two concentric cylinders separated by a characteristic length ($L = r_o - r_i$) and rotating relative to each other at different temperatures. Because of the larger surface-to-volume ratio of the domain, phenomena such as viscous friction and dissipation and heat transfer are dominant. The first diagram in Fig. 1 shows the experimental setup of concentric cylinders rotating with relative speed, wherein the outer cylinder is held stationary. The inner cylinder is rotated using an air turbine and, to prevent the shaft from whirling, vibration dampers are placed below in the vacuum chamber. In 1971, Alofs *et al.* [7] conducted an experiment using this setup to investigate rarefied gas

flow between concentric cylinders. They reported the radial density profile (redistributed by the motion of the inner cylinder) and the values of tangential momentum and thermal accommodation coefficients from the measurement for aluminum cylinders. However, their work was limited to monatomic argon gas, and no information on diatomic and polyatomic gases and the thermal characteristics was given.

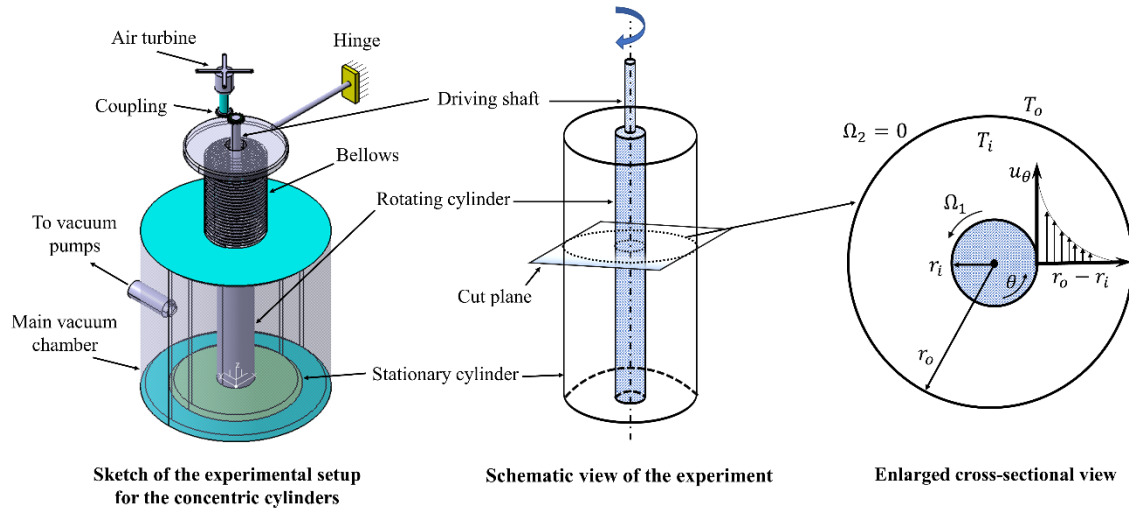


Fig. 1. Schematic of cylindrical Couette flow (CCF) and computational domain in present study.

Because of its simplicity and diverse applications to practical problems, gaseous CCF has been extensively investigated. For instance, previous studies [20,23-27] reported the velocity inversion phenomenon in which the tangential velocity increases in the radial direction when the inner cylinder is rotating and the outer one is stationary. Other studies [28-33] investigated the effects of the radius ratio and gas–surface interactions on the tangential velocity profiles and the shear stress and torque exerted on the cylinders. Those studies used various theoretical and computational methods such as the Navier–Stokes equations with Langmuir and Maxwell slip conditions [20,25], the power-law wall-scaling approach [28,29], the Bhatnagar–Gross–Krook (BGK) model [26], the regularized 13-moment equations [34], the Boltzmann equation [35], and direct simulation Monte Carlo (DSMC) [29-32,36-40].

Independently of the aforementioned methods, Myong [14] investigated the Knudsen layer close to the wall surface for planar Couette flows of monatomic gases, using the so-called

second-order nonlinear coupled constitutive relations (NCCR) together with gas–surface molecular interaction models [41-46]. The NCCR, which is a thermodynamically consistent hydrodynamic model for high-Knudsen-number gas flows, was proposed first by Myong in 1999 [47] and it has been studied since by other researchers [3,48-53] as a novel alternative to previous moment-based approaches [54]. However, there is still room for improvement in our understanding of this important flow problem.

To date, most studies have focused on the mechanical characteristics of rarefied and microscale gases in CCF, such as the velocity profile, tangential shear stress, and torque, whereas very few studies have been devoted to thermal characteristics (temperature, density, and heat transfer). Note that mechanical and thermal properties are in general tightly coupled in nonequilibrium flow fields of rarefied and microscale gases. Therefore, complete understanding of nonequilibrium gases in CCF requires full treatment of the mechanical and thermal aspects. The present study aims to achieve that goal: full description of all conserved variables (not only velocity and pressure but also density and temperature) and non-conserved variables (not only tangential shear stress and normal heat flux but also normal shear stress and tangential heat flux).

Most previous studies considered monatomic gases only in the analysis. In gas molecules, the internal energy is stored in various modes, such as translational, rotational, and vibrational. Diatomic and polyatomic gas molecules possess rotational and vibrational modes, which are associated with the rotation of atoms around an axis and vibration of atoms along an inter-nuclear axis, respectively. Because the vibrational mode becomes relevant only in high-temperature gases beyond 1000 K, it is usually neglected in the analysis. However, to treat diatomic and polyatomic gases such as nitrogen and carbon dioxide rigorously, theoretical and computational models developed initially for monatomic gases must be modified significantly. For example, the Stokes' hypothesis introduced in the two-century old Navier–Stokes equations must be abandoned, and the Boltzmann kinetic equation and DSMC must be extended to include the rotational mode of gas molecules in both kinematic and collisional descriptions. Otherwise, the rotational mode of gas molecules is accounted for only in the equilibrium level (through the specific heat ratio), completely neglecting additional nonequilibrium effects associated with the excess normal stress and the bulk viscosity present

in diatomic and polyatomic gases.

The literature contains some kinetic models for diatomic and polyatomic gases [8,55-65] and experimental studies of heat exchange between fine filaments and a rarefied gas [66,67]. However, these studies were limited to pure experimental study, simple geometries such as planar Couette and Poiseuille, or a stationary rarefied gas confined between non-rotating concentric cylinders. The present study attempts to fill this gap by focusing on nonequilibrium diatomic and polyatomic gases in rotating CCF.

The second-order constitutive model for diatomic and polyatomic gases can be derived systematically from the Boltzmann–Curtiss kinetic equation [68] based on Eu’s modified moment method [69,70] and Myong’s closing-last balanced closure [71]. The Boltzmann–Curtiss kinetic equation additionally introduces the angular momentum and azimuth angle associated with the rotational mode of molecules to the kinetic formulation and thus smoothly extends the original Boltzmann kinetic equation to diatomic and (linear) polyatomic gases. In the second-order constitutive model, the constitutive relations between stresses (and heat flux) and the strain rate (and the temperature gradient) are generally nonlinear and coupled in states far from thermal equilibrium.

Implementing the second-order non-Navier–Fourier constitutive model numerically presents non-trivial challenges, particularly in the multi-dimensional problem. For example, the functional form of the second-order non-Navier–Fourier constitutive model is highly nonlinear and implicit and requires an additional computational algorithm. Among several possible numerical methods, the discontinuous Galerkin (DG) method [72-77] was used in the present study because of its ability to compute low- and high-Mach number flows with a single framework without resorting to the time-preconditioning techniques normally required for the finite-volume method. The implicit nature of the second-order constitutive model was treated by introducing an auxiliary variable, resulting in a mixed-type DG method. This type of multi-dimensional DG scheme of the second-order constitutive model has an advantage in solving various practical problems, such as the three-dimensional experimental configuration of rotating CCF shown in Fig. 1. It has also been applied successfully to some challenging problems of nonequilibrium diatomic and polyatomic gas flows, such as shock vortex interactions [76,77].

Here, based on the DG scheme of the second-order non-Navier–Fourier constitutive model and the gas–surface molecular interaction models, both the fluid dynamic and thermal characteristics of nonequilibrium diatomic and polyatomic gases in rotating CCF are investigated. Section 2 outlines the problem statement for solving rotating CCF, and Sec. 3 presents the governing equations, slip and jump conditions DG method, and verification and validation of the numerical code. Section 4 presents the second-order non-Navier–Fourier constitutive relations in the cylindrical coordinates. Using theoretical and computational results, the thermo-physical behavior of nonequilibrium monatomic, diatomic, and polyatomic gases in rotating CCF is investigated. Section 5 provides some concluding remarks and discusses issues of further development in this topic. Finally, the Appendix presents new analytic solutions for CCF of a compressible gas flow with the Navier–Fourier constitutive laws and the Maxwell slip and Smoluchowski jump conditions including the temperature profile.

2. Formulation of rotating cylindrical Couette flow with focus on thermal effects

The computational domain comprises inner (r_i) and outer (r_o) radii rotating with their respective angular velocities Ω_i and Ω_o , as shown in Fig. 1. The rotational axes of these cylinders coincide with the z -axis of the Cartesian coordinate system. The cylinders are assumed to be of infinite length and variations in the axial direction (end effects) are neglected. Consecutively, there exists a temperature distribution in only the radial direction. In this study, the non-dimensional radial distance is defined as $(r - r_i)/(r_o - r_i)$. For consistency with the literature, all the numerical simulations were performed with constant angular speed at the inner cylinder and keeping the outer cylinder stationary. Note that no velocity inversion (non-linear behavior) occurs in the opposite scenario, i.e., rotating outer and stationary inner cylinders [25].

To analyze thermal effects in CCF, two sets of Dirichlet temperature boundary conditions were considered for the walls: (i) isothermal walls (where the gas and cylinder walls are at the same temperature), and (ii) non-isothermal walls (where a higher temperature is imposed on the inner wall).

To characterize the temperature distribution in CCF, the dimensionless parameter,

$$\beta = \frac{T_i - T_o}{T_r} = \frac{T_{w_1} - T_{w_2}}{T_r}, \quad (1)$$

is introduced, where $T_i (= T_{w_1})$ and $T_o (= T_{w_2})$ are the temperatures of the inner and outer cylinders, respectively. The reference temperature T_r is defined as the initial temperature of the gas (273 K).

To measure the degree of rarefaction in the nonequilibrium flow regime, the Knudsen number defined as [71,78],

$$\text{Kn} = \frac{\lambda}{r_o - r_i} = \frac{M}{\text{Re}} \sqrt{\frac{\gamma\pi}{2}}, \quad (2)$$

is introduced, where λ is the mean-free-path, M is the Mach number, Re is the Reynolds number. The specific heat ratio γ of the gas has different values depending on the type of gas molecules (monatomic, diatomic, or polyatomic), as summarized in Table I. The specific heat ratio is assumed to be 5/3 for argon, 7/5 for nitrogen, and 1.312 for methane. In Eq. (2), the variable-hard-sphere model is used for the interactions of the gas molecules [47].

Table I. Physical parameters for monatomic, diatomic, and polyatomic gases [79].

Gas parameters	Monatomic (Ar)	Diatomic (N ₂)	Polyatomic (CH ₄)
Viscosity ratio (f_b)	0.0	0.8	1.33
Degrees of freedom (ζ)	3	5	6.4
Heat capacity ratio (γ)	1.667	1.4	1.312
Gas constant (R)	208.24	296.913	518.45
Heat capacity (c_p)	519.04	1039.19	2177.49
Viscosity (μ)	2.117×10^{-5}	1.656×10^{-5}	1.024×10^{-5}
Viscosity index (s)	0.81	0.74	0.84
Prandtl number (Pr)	0.667	0.7368	0.7706
Thermal conductivity	0.01725	0.02335	0.02893

In passing, note that the Knudsen number alone cannot represent the degree of thermal nonequilibrium in the macroscopic description of rotating CCF. The reason for this is that the Knudsen number is a pure thermodynamic quantity and provides no average-velocity information in the present dynamic gas flow. Rather, a combination of the Knudsen and Mach numbers, specifically $\text{Kn} \times M$, should be used to measure the degree of thermal nonequilibrium [42].

3. Mathematical formulation and numerical procedure

3.1. Governing equations for nonequilibrium diatomic and polyatomic gases

3.1.1. Boltzmann–Curtiss kinetic equation for diatomic and polyatomic gases

In case of no external force field, the Boltzmann–Curtiss kinetic equation for diatomic (and linear polyatomic) molecules with a moment of inertia I_m and an angular momentum j can be expressed as follows [68-70,77],

$$\left(\frac{\partial}{\partial t} + \mathbf{v} \cdot \nabla + \frac{j}{I_m} \frac{\partial}{\partial \psi} \right) f(\mathbf{v}, \mathbf{r}, \mathbf{j}, \psi, t) = R[f], \quad (3)$$

where f , \mathbf{v} , \mathbf{r} , ψ , j , and $R[f]$ represents the distribution function of the population of molecules, the particle velocity, the particle position, the azimuthal angle associated with the orientation of the molecules, the magnitude of the angular momentum vector \mathbf{j} , and the collision integral, respectively. When ignoring the angular momentum of the molecule related to the rotational mode from equation (3), the original Boltzmann kinetic equation for a monatomic gas is recovered [80-82],

$$\left(\frac{\partial}{\partial t} + \mathbf{v} \cdot \nabla \right) f(\mathbf{v}, \mathbf{r}, t) = C[f], \quad (4)$$

where $C[f]$ refers to the Boltzmann collision integral of the interaction between two particles.

The macroscopic quantities, conserved variables (ρ , $\rho \mathbf{u}$, ρE) and non-conserved variables ($\mathbf{\Pi}$, Δ , \mathbf{Q}), can be defined using the following statistical relationships:

$$\phi^{(h)} = \langle h^{(k)} f \rangle, \quad (5)$$

where the angular bracket denotes the integration over the velocity space \mathbf{v} and the azimuthal

angle \mathbf{j} . The $h^{(k)}$ indicates the molecular expression of the h -th moments of the distribution function and $\phi^{(h)}$ denotes the corresponding macroscopic quantity. The leading elements of the sets of the conserved and non-conserved variables (in the statistical form) are defined as [69],

$$\begin{aligned}\phi^{(1)} &= \rho, \quad \phi^{(2)} = \rho \mathbf{u}, \quad \phi^{(3)} = \rho E, \\ \phi^{(4)} &= \mathbf{\Pi} = [\mathbf{P}]^{(2)}, \quad \phi^{(5)} = \Delta = \frac{1}{3} \text{Trace } \mathbf{P} - p, \quad \phi^{(6)} = \mathbf{Q},\end{aligned}\quad (6)$$

where ρ , \mathbf{u} , and E are the density, velocity vector, and total energy density, respectively. Non-conserved variables $\mathbf{\Pi}$, Δ , \mathbf{P} , and \mathbf{Q} denote the shear stress tensor, the excess normal stress, the total stress tensor, and the heat flux, respectively. The corresponding molecular expressions to this set read as

$$\begin{aligned}h^{(1)} &= m, \quad h^{(2)} = m\mathbf{v}, \quad h^{(3)} = \frac{1}{2}mC^2 + H_{rot}, \\ h^{(4)} &= [m\mathbf{C}\mathbf{C}]^{(2)}, \quad h^{(5)} = \frac{1}{3}mC^2 - p/n, \quad h^{(6)} = \left(\frac{1}{2}mC^2 + H_{rot} - m\hat{h}\right)\mathbf{C}.\end{aligned}\quad (7)$$

Here m is the molecular mass of gas, $\mathbf{C} = \mathbf{v} - \mathbf{u}$ is the peculiar velocity of the molecule, n is the number density per unit mass, \hat{h} is the enthalpy density per unit mass, and $H_{rot} = j^2/(2I_m)$ is the rotational Hamiltonian of the particle.

The pressure p and temperature T are related through the equation of state, $p = \rho RT$. The total stress tensor (\mathbf{P}) is decomposed into the hydrostatic pressure (p), the viscous shear stress ($\mathbf{\Pi}$), and excess normal stress (Δ) through the relation,

$$\mathbf{P} = \frac{1}{3} \text{Tr}(\mathbf{P})\mathbf{I} + [\mathbf{P}]^{(2)} = (p + \Delta)\mathbf{I} + \mathbf{\Pi}, \quad (8)$$

where \mathbf{I} is the unit second rank tensor and the symbol $[\mathbf{P}]^{(2)}$ denotes the traceless symmetric part of the second rank stress tensor \mathbf{P} .

The conservation laws of mass, momentum, and total energy for diatomic and polyatomic gases can be derived directly from the Boltzmann–Curtiss kinetic equation by noting collision invariants, that is, $\langle h^{(1,2,3)} R[f] \rangle = 0$. After differentiating the statistical definition of the conserved variables with time and combining them with the Boltzmann–Curtiss kinetic

equation, the following conservation laws, all of which are an exact consequence of the Boltzmann–Curtiss kinetic equation, can be derived [70],

$$\frac{\partial}{\partial t} \begin{bmatrix} \rho \\ \rho \mathbf{u} \\ \rho E \end{bmatrix} + \nabla \cdot \begin{bmatrix} \rho \mathbf{u} \\ \rho \mathbf{u} \mathbf{u} + p \mathbf{I} \\ (\rho E + p) \mathbf{u} \end{bmatrix} + \nabla \cdot \begin{bmatrix} 0 \\ \mathbf{\Pi} + \Delta \mathbf{I} \\ (\mathbf{\Pi} + \Delta \mathbf{I}) \mathbf{u} + \mathbf{Q} \end{bmatrix} = 0. \quad (9)$$

Here the total energy E is given as

$$E = \frac{1}{2} \mathbf{u} \cdot \mathbf{u} + \frac{p}{(\gamma - 1)\rho}. \quad (10)$$

It is convenient to express the conservation laws (9) in dimensionless form for computational purpose. We introduce the following dimensionless variables and parameters

$$\begin{aligned} t^* &= \frac{t}{(L/u_r)}, \quad \mathbf{x}^* = \frac{\mathbf{x}}{L}, \quad \nabla^* = L \nabla, \quad \rho^* = \frac{\rho}{\rho_r}, \quad \mathbf{u}^* = \frac{\mathbf{u}}{u_r}, \quad p^* = \frac{p}{p_r}, \quad T^* = \frac{T}{T_r}, \\ E^* &= \frac{E}{u_r^2}, \quad c_p^* = \frac{c_p}{c_{pr}}, \quad \mu^* = \frac{\mu}{\mu_r}, \quad k^* = \frac{k}{k_r}, \\ \mathbf{\Pi}^* &= \frac{\mathbf{\Pi}}{(\mu_r u_r / L)}, \quad \Delta^* = \frac{\Delta}{(\mu_b u_r / L)}, \quad \mathbf{Q}^* = \frac{\mathbf{Q}}{(k_r \Delta T / L)}, \end{aligned} \quad (11)$$

where the subscript r denotes the reference state, L denotes the characteristic length, c_p is the heat capacity per unit mass at constant pressure, and the terms μ , μ_b , and k represent the Chapman–Enskog shear viscosity, bulk viscosity, and thermal conductivity, respectively. The non-dimensional conservation laws for diatomic and polyatomic gases can be written as [70],

$$\frac{\partial \mathbf{U}^*}{\partial t^*} + \nabla^* \cdot \mathbf{F}_{inv}^* (\mathbf{U}^*) + \nabla^* \cdot \mathbf{F}_{vis}^* (\mathbf{U}^*, \mathbf{\Pi}^*, \Delta^*, \mathbf{Q}^*) = 0, \quad (12)$$

where \mathbf{U}^* , \mathbf{F}_{inv}^* , \mathbf{F}_{vis}^* represent the conserved variables, inviscid flux vector, and viscous flux vector, respectively, defined as,

$$U = \begin{bmatrix} \rho^* \\ \rho^* \mathbf{u}^* \\ \rho^* E^* \end{bmatrix}, \mathbf{F}_{inv} = \begin{bmatrix} \rho^* \mathbf{u}^* \\ \rho^* \mathbf{u}^* \mathbf{u}^* + \frac{1}{\gamma M^2} p^* \mathbf{I} \\ \left(\rho^* E^* + \frac{1}{\gamma M^2} p^* \right) \mathbf{u}^* \end{bmatrix}, \mathbf{F}_{vis} = \frac{1}{\text{Re}} \begin{bmatrix} 0 \\ \Pi^* + f_b \Delta^* \mathbf{I} \\ \left(\Pi^* + f_b \Delta^* \mathbf{I} \right) \cdot \mathbf{u}^* + \frac{1}{\text{EcPr}} \mathbf{Q}^* \end{bmatrix}, \quad (13)$$

Here Mach, Reynolds, Eckert (Ec), Prandtl (Pr) numbers are defined as follows,

$$M \equiv \frac{u_r}{\sqrt{\gamma R T_r}}, \quad \text{Re} \equiv \frac{\rho_r u_r L}{\mu_r}, \quad \text{Ec} \equiv \frac{(\gamma - 1) M^2}{\Delta T / T_r}, \quad \text{Pr} \equiv \frac{c_p \mu_r}{k_r}, \quad c_p = \frac{\gamma R}{\gamma - 1}, \quad f_b = \frac{\mu_{br}}{\mu_r}. \quad (14)$$

If the reference temperature ΔT in the Eckert number is defined as T_r (the initial temperature of the gas 273 K), it is reduced to $\text{Ec} = (\gamma - 1) M^2$. The factor $f_b = \mu_{br} / \mu$ is the ratio of the bulk viscosity to the shear viscosity. Its value is experimentally determined using a sound wave adsorption measurement [83]. The value of f_b is assumed to be 0.0 for argon, 0.8 for nitrogen, and 1.33 for methane, as summarized in Table I. The value of the Prandtl number may be calculated through Eucken's relation,

$$\text{Pr} = \frac{4\gamma}{9\gamma - 5}. \quad (15)$$

3.1.2. First-order (Navier–Fourier) Boltzmann–Curtiss based constitutive model

The first-order constitutive model (also termed as Navier–Fourier) of non-conserved variables can be derived by differentiating the statistical definition of the non-conserved variables with time and combining them with the Boltzmann–Curtiss kinetic equation. Using these formulations, the shear stress tensor, the excess normal stress, and heat flux vector can be obtained,

$$\Pi_0 = -2\mu [\nabla \mathbf{u}]^{(2)}, \quad \Delta_0 = -\mu_b \nabla \cdot \mathbf{u}, \quad \mathbf{Q}_0 = -k \nabla T. \quad (16)$$

Here the subscript 0 represents the first-order Navier–Fourier constitutive model. During this process, the first-order balanced closure was applied [71]. In the first-order constitutive model (16), the following Chapman–Enskog linear transport coefficients can be employed,

$$\mu = T^s, \mu_b = f_b \mu, k = T^s, \text{ where } s = \frac{1}{2} + \frac{1}{\nu - 1} \quad (17)$$

In this expression, the superscript s stands for the index of the inverse power laws of gas molecules, and the parameter ν is the exponent of the inverse power laws for the gas-particle interaction potentials. The value of s is assumed to be 0.81 for the argon, 0.78 for the nitrogen, and 0.84 for the methane gas, as summarized in Table I.

Once the Stokes' hypothesis is applied, that means $\mu_b = 0$, the first-order Navier–Fourier model (16) reduced to the well-known two-century old Navier–Stokes–Fourier (NSF) equation,

$$\mathbf{\Pi}_0 = -2\mu[\nabla\mathbf{u}]^{(2)}, \quad \mathbf{Q}_0 = -k\nabla T. \quad (18)$$

Note that, because of zero bulk viscosity, the dilatational term $\nabla \cdot \mathbf{u}$ does not play any role in the level of the constitutive equation of viscous stress in the NSF equation, even though it may play a significant role in the level of conservation laws, like shock-dominated compressible gas flows. While the Stokes hypothesis can be regarded legitimate for monatomic gases like argon (or at least the value of the bulk viscosity is very small), there is ever increasing evidence that now indicates this is not the case for diatomic and polyatomic gases—like nitrogen (or air), hydrogen, methane, and carbon dioxide [69,70,76,77,83].

3.1.3. Second-order Boltzmann–Curtiss constitutive model

Similarly, we can derive the second-order constitutive model by first differentiating the statistical definition of the non-conserved variables $h^{(4,5,6)}$ with time and then combining them with the Boltzmann–Curtiss kinetic equation [82]. However, it turns out that the derivation of the second-order constitutive model (also referred to as nonlinear coupled constitutive relations (NCCR)) is extremely difficult, mainly due to two fundamental issues [84,85]: the so-called closure problem and accurate treatment of the dissipation terms $\langle h^{(4,5,6)} R[f] \rangle$.

Myong in 2014 proposed a new closure theory [71], known as “closing-last balanced closure,” from a keen observation of the essence of the closure problem in a complex system. On the other hand, to accurately calculate the dissipation terms while making the underlying theory compatible with the second law of thermodynamics, Eu in 1980 proposed cumulant expansion

based on the canonical distribution function in the exponential form for the explicit calculation of the dissipation term [82,84].

Furthermore, the temporal dependence in the equations can be neglected, owing to the very short relaxation times of the non-conserved variables, being on the order of 10^{-10} seconds [47,82], compared to those for conserved variables and the characteristic times of the flow process. These so-called adiabatic approximations simplify the partial differential equation into a set of algebraic equations, which significantly reduces the numerical complexities involved in solving the constitutive equations.

Once these tenets—Myong’s closing-last balanced closure and Eu’s cumulant expansion for the explicit calculation of the dissipative term—are applied and after introducing the adiabatic approximation, the following second-order constitutive model for diatomic and polyatomic gases [70,77,86] can be derived,

$$\begin{aligned}\hat{\Pi}q_{2\text{nd}}(c\hat{R}) &= [\hat{\Pi} \cdot \nabla \hat{\mathbf{u}}]^{(2)} + (1 + f_b \hat{\Delta}) \hat{\Pi}_0, \\ \hat{\Delta}q_{2\text{nd}}(c\hat{R}) &= \frac{3}{2} (\hat{\Pi} + f_b \hat{\Delta} \mathbf{I}) : \nabla \hat{\mathbf{u}} + \hat{\Delta}_0, \\ \hat{\mathbf{Q}}q_{2\text{nd}}(c\hat{R}) &= \hat{\Pi} \cdot \hat{\mathbf{Q}}_0 + (1 + f_b \hat{\Delta}) \hat{\mathbf{Q}}_0,\end{aligned}\tag{19}$$

where

$$q_{2\text{nd}}(c\hat{R}) = \frac{\sinh(c\hat{R})}{c\hat{R}}.\tag{20}$$

All terms in equations (19) are normalized by introducing following variables and parameters,

$$\begin{aligned}\hat{\Pi} &\equiv \frac{\Pi}{p} = \frac{N_\delta}{p^*} \Pi^*, \quad \hat{\Delta} \equiv \frac{\Delta}{p} = \frac{N_\delta}{p^*} \Delta^*, \quad \hat{\mathbf{Q}} \equiv \frac{\mathbf{Q}}{p \sqrt{\frac{C_p T}{2 \text{Pr}}}} = \frac{N_\delta}{p^*} \frac{\mathbf{Q}^*}{\sqrt{T^*/(2\varepsilon)}}, \\ \nabla \hat{\mathbf{u}} &\equiv \frac{-2\mu \nabla \mathbf{u}}{p} = -2\mu^* \frac{N_\delta}{p^*} \nabla^* \mathbf{u}^*, \quad N_\delta \equiv \frac{\mu_r u_r / L}{p_r} = \frac{\gamma M^2}{\text{Re}} = \text{Kn} M \sqrt{\frac{2\gamma}{\pi}}, \quad \varepsilon \equiv \frac{1}{Ec \text{Pr}} \frac{1}{T_r / \Delta T}.\end{aligned}\tag{21}$$

Here the caret (^) over a symbol represents the ratio of the stress Π to the pressure p and the ratio of the heat flux \mathbf{Q} to a quantity $p(C_p T / 2 \text{Pr})^{1/2}$. The values of $\hat{\Pi}_0$, $\hat{\Delta}_0$, and $\hat{\mathbf{Q}}_0$ are

determined by the linear Newtonian law of shear and bulk viscosity, and the linear Fourier law of heat conduction, respectively, given in equation (16). The constant c , which is given by $c = \left[\frac{2\sqrt{\pi}}{5} A_2(\nu) \Gamma(4 - \frac{2}{\nu-1}) \right]^{1/2}$, has a value between 1.0138 (Maxwellian) and 1.2232 ($\nu = 3$); for instance, 1.018 for the nitrogen gas molecule [70]. The tabulated values of $A_2(\nu)$ are available in the literature [87].

The Rayleigh-Onsager dissipation function \hat{R} appearing in (19) and (20) can be expressed as [70]

$$\hat{R} = \left[\hat{\Pi} : \hat{\Pi} + 2\gamma' f_b \hat{\Delta}^2 + \hat{\mathbf{Q}} \cdot \hat{\mathbf{Q}} \right]^{1/2}, \quad (22)$$

where $\gamma' = (5 - 3\gamma) / 2$. Note that, once $q_{2nd}(c\hat{R})$ is taken first-order closure, that is, $q_{1st} = 1$, all the coupled terms in the left-hand side of equations (19) are neglected, the corresponding constitutive models exactly recover the first-order Navier–Fourier model (16), ensuring the smooth extension from the first-order to the second-order.

Constitutive equations (or relations) in fluid dynamics describe the thermo-fluidic behavior of fluid under certain thermodynamic driving forces like spatial gradients of velocity and temperature. Fig. 2 shows the topology of the second-order solution of the Boltzmann-Curtiss-based constitutive model in the velocity-shear flow problem in a phase space (Π_{xx}, Π_{xy}, p) [88]. The topological representation of the constitutive relations can provide new information and fascinating insight into the physics of fluids, which otherwise is not obtainable.

The topology of the Boltzmann–Curtiss-based constitutive model in the velocity-shear flow problem varies from an ellipse (at small f_b) to a circle, to a parabola, and then finally to a hyperbola (at large f_b) with the bulk viscosity ratio in diatomic and polyatomic gases. Such topologies are very similar to orbits of planets and comets in the Solar system governed by the two-body Kepler’s laws. The bulk viscosity associated with the rotational mode of gas particles in reference to the shear viscosity plays exactly the same role in the energy associated with the angular motion of the planets and comets in reference to the gravitational potential energy [88]. Moreover, as the pressure decreases, the ellipse cone (at $f_b = 0$) keeps its topology, whereas the hyperboloid (at $f_b = 1.0$) approaches a different topology of straight lines, as shown in

Fig. 2. All these properties indicate critical roles of the rotational mode of diatomic and polyatomic gases in the thermo-fluidic behavior of nonequilibrium gases under thermodynamic driving forces.

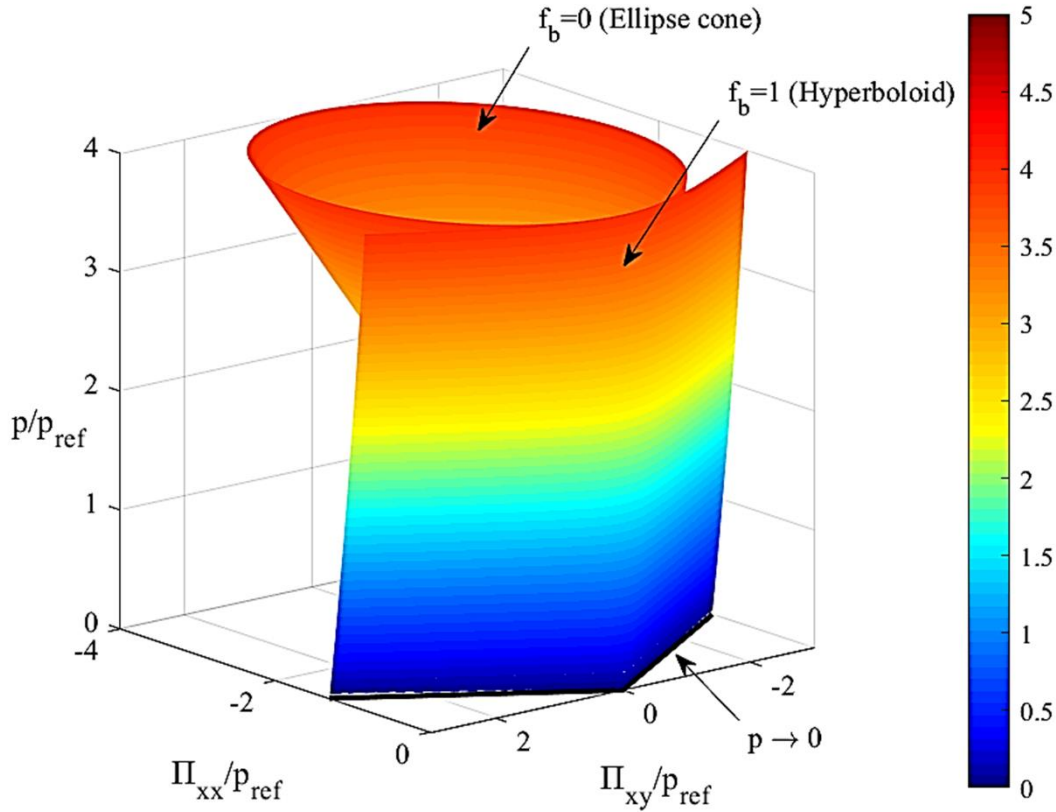


Fig. 2. Topology of the second-order Boltzmann–Curtiss-based constitutive model in the velocity shear flow problem in a phase space (Π_{xx}, Π_{xy}, p) for $f_b = 0.0, 1.0$. (Reproduced with permission from Singh et al., “Topology of the second-order constitutive model based on the Boltzmann–Curtiss kinetic equation for diatomic and polyatomic gases,” *Phys. Fluids* 32, 026104 (2020). Copyright 2020 AIP).

Fig. 3 shows the general features of the first- and second-order constitutive models for monatomic and diatomic gases in the compression-expansion and velocity shear flows. In the case of rapid compression and expansion of gas, the second-order constitutive model shows non-linear asymmetric relation of the normal stress, as illustrated in Fig. 3(a). Although slight differences are observed in the profile of second-order constitutive models for monatomic and diatomic gases, the general pattern remains the same.

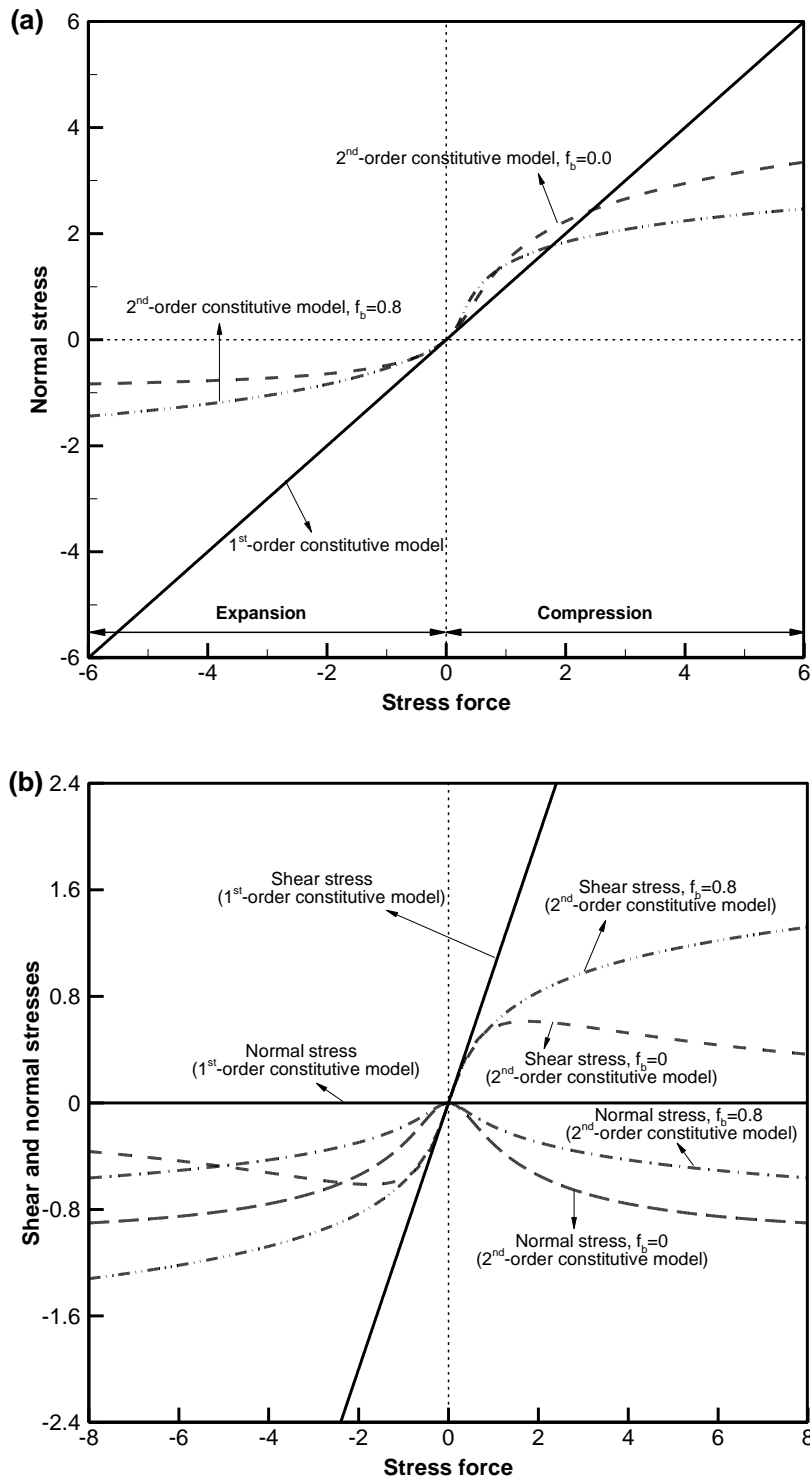


Fig. 3. First-order and second-order solutions of the Boltzmann–Curtiss-based constitutive model for monatomic ($f_b = 0.0$) and diatomic ($f_b = 0.8$) gases in (a) compression - expansion flow, (b) velocity shear flow.

In the case of velocity shear flow, which is directly related to the present cylindrical Couette flow, the viscous shear stress $\hat{\Pi}_{xy}$ obtained using the second-order constitutive model recovers the first-order model near the origin, but it becomes highly nonlinear as the stress force (shear velocity gradient) increases, as illustrated in Fig. 3(b). The second-order constitutive model displays shear-thinning characteristics, yielding a smaller shear stress compared to the first-order constitutive model. Furthermore, it produces non-zero normal stress values for a velocity gradient in the velocity shear flow, which is in stark contrast with vanishing normal stress of the first-order constitutive model.

3.1.4. Conservation laws in compressible one-dimensional cylindrical Couette flow

The conservation laws of mass, momentum and total energy given in (9) reduce to the following forms for the steady-state one-dimensional CCF of a compressible gas:

$$\begin{aligned}
\frac{1}{r} \frac{d}{dr} (r \rho u_r) &= 0, \\
\rho \left(u_r \frac{du_r}{dr} - \frac{u_\theta^2}{r} \right) + \frac{d(p + \Delta)}{dr} + \frac{d\Pi_{rr}}{dr} + \frac{\Pi_{rr} - \Pi_{\theta\theta}}{r} &= 0, \\
\rho \left(u_r \frac{du_\theta}{dr} + \frac{u_r u_\theta}{r} \right) + \frac{1}{r^2} \frac{d}{dr} (r^2 \Pi_{r\theta}) + \frac{\Pi_{r\theta} - \Pi_{\theta r}}{r} &= 0, \\
\rho u_r \frac{dE}{dr} + \frac{1}{r} (p + \Delta) u_r + \Pi_{\theta r} \frac{du_\theta}{dr} - \frac{\Pi_{r\theta}}{r} u_\theta + \frac{\Pi_{\theta\theta}}{r} u_r + \frac{1}{r} \frac{d(rQ_r)}{dr} &= 0,
\end{aligned} \tag{23}$$

where u_r and u_θ are the velocity components in r and θ directions, respectively. Note that these equations are exact physical conservation laws, not the Navier–Fourier equations, and so they hold for any flow situation irrespective of the Knudsen or Mach number, the type of gas, or the boundary conditions.

The radial velocity vanishes by the solid wall boundary condition ($u_r=0$) in one-dimensional CCF. However, the normal stresses Π_{rr} and $\Pi_{\theta\theta}$ remain finite in states away from thermal equilibrium, as indicated in Fig. 3 (b). Because the viscous stress tensor $\mathbf{\Pi}$ is symmetric, the shear stresses $\Pi_{r\theta}$ and $\Pi_{\theta r}$ are the same. Note that the radial heat flux Q_r appears in the conservation law of total energy, whereas the tangential heat flux Q_θ does not, because the tangential heat flux has no dependence in the circumferential direction θ . However,

the tangential heat flux Q_θ itself remains finite in states away from thermal equilibrium.

3.1.5. Description of important physical quantities

To characterize the mechanical and thermal characteristics of gases in CCF, the following physical quantities are often used.

3.1.5.1 Torque

The constant angular speed of the rotating cylinder exerts a torque on its wall, which is represented in terms of wall shear stress as [29,89]

$$\tau = 2\pi r^2 |\Pi_{r\theta}|, \quad (24)$$

where $\Pi_{r\theta}$ is the shear stress acting on the wall and r is the radius of the cylinder.

3.1.5.2 Torque coefficient

The torque coefficient measures the ratio of the torque exerted on the cylinder wall to the power of the bulk gas flow, and it is expressed as [29,89]

$$C_\tau = \frac{\tau}{0.5\rho_r u_{\theta_w}^2 \cdot \pi r^2}, \quad (25)$$

where u_{θ_w} is the rotational speed of the inner cylinder.

3.1.5.3 Stanton number

The Stanton number (St) is the ratio of the amount of heat transfer of the gas to its thermal capacity, and the sign of the heat flux determines the sign of the Stanton number. This number characterizes the intensity of energy dissipation in a gas flow and is expressed as [89,90],

$$\text{St} = \frac{Q_r}{\rho_r c_p |u_{\theta_w}| T_{w_1}}. \quad (26)$$

3.2. Discontinuous Galerkin method

The standard DG method cannot handle the spatial discretization of the conservation laws (12) in conjunction with the second-order constitutive relations (19), because of the highly non-linear and implicit form of the second-order constitutive relations. To overcome this

computational difficulty, we employ an in-house, mixed modal discontinuous Galerkin (DG) code developed by Myong and co-researchers [73,76,77,80,86,91]. In this mixed formulation, an additional auxiliary variable “ Θ ” is introduced to handle the second-order derivatives appearing in the conservation laws due to the implicit constitutive relations of viscous stress and heat flux. This auxiliary variable can be defined as the derivative of either primitive or conservative variables. To apply the mixed DG formulation, the conservation laws (12) (with the asterisks omitted for notational brevity) can be expressed as a coupled system for \mathbf{U} and Θ as,

$$\begin{aligned} \Theta - \nabla \mathbf{U} &= 0, \\ \frac{\partial \mathbf{U}}{\partial t} + \nabla \cdot \mathbf{F}_{inv}(\mathbf{U}) + \nabla \cdot \mathbf{F}_{vis}(\mathbf{U}, \Theta) &= 0. \end{aligned} \quad (27)$$

These coupled systems of equations are solved by discretizing the computational domain into the unstructured triangular elements. These discretized coupled systems of equations over the domain Ω are approximated by Ω_h such that $\Omega_h \rightarrow \Omega$ as $h \rightarrow 0$. The approximated domain Ω_h is then tessellated into a collection of non-overlapping elements Ω_e such that $\mathcal{T}_h = \{\Omega_e\}$. Finally, over this domain Ω_h , we introduce the piecewise polynomial space of the functions $v_h: \Omega_h \mapsto \mathcal{R}$ such that,

$$V_h = \left\{ v_h \in L_2(\Omega_h) : v_h|_{\Omega_e} \in P^k(\Omega_e), \forall \Omega_e \in \mathcal{T}_h \right\}, \quad (28)$$

where $L_2(\Omega_h)$ denotes the space function of the squared Lebesgue integrable over the domain Ω_h and $P^k(\Omega_e)$ denotes the space of polynomial functions of degree at most k in element Ω_e . Thereafter, the exact solutions of \mathbf{U} and Θ are approximated by the DG polynomial approximations of $\mathbf{U}_h \in V_h(\mathcal{T}_h)$ and $\Theta_h \in V_h(\mathcal{T}_h)$, respectively,

$$\begin{aligned} \mathbf{U}_h(\mathbf{x}, t) &= \sum_{i=0}^{N_k} \mathbf{U}_h^i(t) b_i(\mathbf{x}), \\ \Theta_h(\mathbf{x}, t) &= \sum_{i=0}^{N_k} \Theta_h^i(t) b_i(\mathbf{x}), \quad \mathbf{x} \in \Omega_e. \end{aligned} \quad (29)$$

Here $\hat{\mathbf{U}}_h^i$, $\hat{\Theta}_h^i$ are the local degrees of freedom of \mathbf{U} and Θ , $b_i(\mathbf{x})$ is the basis function for the finite element space, and N_k is the number of required basis functions for the k - exact DG approximation. In this work, we employ the second-order modal basis functions of Dubiner

[92] for unstructured triangular elements. Furthermore, the mixed system of equations (27) is multiplied with the test function, which is considered the same as the basis function b_h , and then integrated by parts over an element Ω_e , resulting in weak formulation of the mixed system,

$$\begin{aligned} \int_{\Omega_e} \Theta_h b_h dV + \int_{\Omega_e} \nabla b_h \cdot \mathbf{U}_h dV - \int_{\partial\Omega_e} b_h \mathbf{U}_h \cdot \mathbf{n} d\Gamma &= 0, \\ \frac{\partial}{\partial t} \int_{\Omega_e} \mathbf{U}_h b_h dV - \int_{\Omega_e} \nabla b_h \cdot \mathbf{F}_{inv} dV + \int_{\partial\Omega_e} b_h \mathbf{F}_{inv} \cdot \mathbf{n} d\Gamma - \int_{\Omega_e} \nabla b_h \cdot \mathbf{F}_{vis} dV + \int_{\partial\Omega_e} b_h \mathbf{F}_{vis} \cdot \mathbf{n} d\Gamma &= 0, \end{aligned} \quad (30)$$

where \mathbf{n} is the outward normal vector, V and Γ are the volume and boundary integral of the element, respectively.

The Gaussian–Legendre quadrature rule has been employed for the calculation of both boundary and volume integrals using $2k$ and $2k + 1$ order accurate Gauss quadrature formula, respectively [93]. The number of Gaussian quadrature points increases with the order of accuracy of the DG approximations. In the present case, $k = 1$ (DG polynomial “ $p1$ ”) is used [91]. The inviscid and viscous fluxes in equation (30) are formulated using the local Lax–Friedrichs (LLF) flux and BR1 schemes, respectively [80]. The monotone LLF flux is commonly used in the DG method owing to its computational efficiency. Although it is the most dissipative flux, it improves the stability of the DG numerical approximation. On the other hand, the BR1 flux is used as the numerical fluxes to calculate the auxiliary and viscous fluxes at the elemental interfaces. All these flux formulations can be written as,

$$\begin{aligned} \mathbf{F}_{inv} \cdot \mathbf{n} &\approx \mathbf{H}_{inv}(\mathbf{U}_h^-, \mathbf{U}_h^+) = \frac{1}{2} [\mathbf{F}_{inv}(\mathbf{U}_h^-) + \mathbf{F}_{inv}(\mathbf{U}_h^+) - \alpha(\mathbf{U}_h^+ - \mathbf{U}_h^-)], \\ \mathbf{U}_h \cdot \mathbf{n} &\approx \mathbf{H}_{aux}(\mathbf{U}_h^-, \mathbf{U}_h^+) = \frac{1}{2} [\mathbf{U}_h^- + \mathbf{U}_h^+], \\ \mathbf{F}_{vis} \cdot \mathbf{n} &\approx \mathbf{H}_{vis}(\mathbf{U}_h^-, \Theta_h^-, \mathbf{U}_h^+, \Theta_h^+) = \frac{1}{2} [\mathbf{F}_{vis}(\mathbf{U}_h^-, \Theta_h^-) + \mathbf{F}_{vis}(\mathbf{U}_h^+, \Theta_h^+)], \\ \alpha &= \max(|\mathbf{U}_h^-| + a_s^-, |\mathbf{U}_h^+| + a_s^+). \end{aligned} \quad (31)$$

Here $a_s = \sqrt{T}/M$ is the speed of sound at an elemental interface, and the superscripts (+) and (−) denote the left and right states of the element interface. The weak formulation of the mixed form equation (30) then becomes

$$\begin{aligned}
& \int_{\Omega_e} \Theta_h b_h dV + \int_{\Omega_e} \nabla b_h \cdot \mathbf{U}_h dV - \int_{\partial\Omega_e} b_h \mathbf{H}_{aux} d\Gamma = 0, \\
& \frac{\partial}{\partial t} \int_{\Omega_e} \mathbf{U}_h b_h dV - \int_{\Omega_e} \nabla b_h \cdot \mathbf{F}_{inv} dV + \int_{\partial\Omega_e} b_h \mathbf{H}_{inv} d\Gamma - \int_{\Omega_e} \nabla b_h \cdot \mathbf{F}_{vis} dV + \int_{\partial\Omega_e} b_h \mathbf{H}_{vis} d\Gamma = 0.
\end{aligned} \tag{32}$$

Finally, assembling all the elemental contributions yields a system of ordinary differential equations in time for each element [80,94],

$$\frac{\partial \mathbf{U}_h}{\partial t} = \mathbf{M}^{-1} \mathbf{R}(\mathbf{U}_h). \tag{33}$$

Here \mathbf{M} , $\mathbf{R}(\mathbf{U}_h)$ represent the elemental orthogonal mass matrix and the residual vector of the system of equations, respectively. To solve the system of equations (33), we employ an explicit three-stage, third-order accurate strong stability preserving Runge–Kutta method (TVD-RK) proposed by Shu and Osher [95].

3.3. Implementation of velocity-slip and temperature-jump conditions

The velocity-slip and temperature-jump conditions on solid surfaces are necessary for describing rarefied and micro- and nano-scale gas flows accurately [14,42,96]. To date, extensive studies have been conducted to derive the proper velocity-slip and temperature-jump conditions near a solid surface [97]. The present study uses both the Langmuir and Maxwell–Smoluchowski slip and jump conditions.

3.3.1. Langmuir slip and jump conditions

In the Langmuir slip and jump conditions, the gas molecules (the adsorbate) are assumed to be adsorbed to the surface (the adsorbent) [98–101]. The amount of adsorbate on the adsorbent is proportional to the pressure at a constant temperature and can be determined by the Langmuir adsorption isotherm [20,42]. This gas–surface interaction process is then expressed based on the fraction α ($0 \leq \alpha \leq 1$) of surface covered at equilibrium in dimensional form [42]:

$$\alpha = \begin{cases} \frac{\bar{\beta} p}{1 + \bar{\beta} p}, & \text{for monatomic gas,} \\ \frac{\sqrt[n]{\bar{\beta} p}}{1 + \sqrt[n]{\bar{\beta} p}}, & \text{for diatomic } (n=2) \text{ and polyatomic } (n \geq 2) \text{ gas,} \end{cases} \tag{34}$$

where the equilibrium constant $\bar{\beta}$ is given by

$$\bar{\beta} = \frac{1}{4\omega\text{Kn}} \frac{1}{p_r} \quad (35)$$

$$\text{where } \omega = \sqrt{\frac{2}{\pi}} \frac{4c^2}{\pi} \left(\frac{T_{\text{wall}}}{T_{\text{ref}}} \right)^{s+1/2} \exp\left(\frac{-D_e}{k_B T_{\text{wall}}} \right).$$

Note that $\bar{\beta}$ depends on the wall temperature as well as an interfacial interaction parameter D_e , which is the heat of adsorption; e.g., $D_e = 5,255$ J/mol for the N_2 -Al molecular interaction model. In these equations, the slip coefficient ω varies with the type of gas, and its value can be taken from previous work [20]. The role of ω is similar to that of the slip coefficient $\omega_M = \frac{2-\sigma_u}{\sigma_u}$ in the Maxwell slip model (σ_u being a momentum accommodation coefficient). In the incompressible limit, Eq. (34) simplifies into

$$\alpha = \begin{cases} \frac{1}{1+4\omega\text{Kn}}, & \text{for monatomic gas,} \\ \frac{1}{1+\sqrt[3]{4\omega\text{Kn}}}, & \text{for diatomic } (n=2) \text{ and polyatomic } (n \geq 2) \text{ gas.} \end{cases} \quad (36)$$

Finally, with the information about the fraction α of surface covered at equilibrium, the velocity slip and temperature jump conditions are written in dimensional form as

$$\begin{aligned} \mathbf{u} &= \alpha \mathbf{u}_{\text{wall}} + (1-\alpha) \mathbf{u}_g, \\ T &= \alpha T_{\text{wall}} + (1-\alpha) T_g, \end{aligned} \quad (37)$$

where the subscript g denotes the local value adjacent to the wall, \mathbf{u}_{wall} is the velocity vector of the solid surface, and T_{wall} is the temperature of the solid surface.

For CCF with a cylinder rotating at an angular velocity Ω , the gas velocity on the cylinders in the Langmuir slip model is expressed as [20]

$$u_\theta = \alpha \Omega r + (1-\alpha) u_\theta(\bar{r}) \frac{r}{\bar{r}}, \quad (38)$$

where u_θ is the tangential velocity, r is the radial coordinate, and \bar{r} is the radius of the reference position defined as

$$\bar{r}^2 = r_o \left[r_i + (r_o - r_i) \left(1 - \frac{r_i}{r_o} \right) \right]. \quad (39)$$

3.3.2. Maxwell velocity slip condition

In 1879, Maxwell [41] derived a velocity slip boundary condition known as the Maxwell velocity slip condition. The slip in tangential velocity near a solid surface is related to the tangential shear stress and the tangential heat flux at the wall; in dimensional form, we have

$$\mathbf{u}_{\text{slip}} - \mathbf{u}_{\text{wall}} = -\omega_M \frac{\lambda}{\mu} \mathbf{\Pi}_{\text{tan}} - \frac{3 \text{Pr}(\gamma - 1)}{4 \gamma p} \mathbf{Q}_{\text{tan}}, \quad (40)$$

where $\omega_M = \left(\frac{2 - \sigma_u}{\sigma_u} \right)$ is the slip coefficient; $\mathbf{\Pi}_{\text{tan}}$ and \mathbf{Q}_{tan} are the tangential shear stress and tangential heat flux at the wall, respectively, and are defined in general coordinates at the surface as

$$\begin{aligned} \mathbf{\Pi}_{\text{tan}} &= (\mathbf{n} \cdot \mathbf{\Pi}) \cdot \mathbf{S}, \\ \mathbf{Q}_{\text{tan}} &= \mathbf{Q} \cdot \mathbf{S}. \end{aligned} \quad (41)$$

Here \mathbf{S} is the surface vector from which the normal component is removed, which is defined mathematically as $\mathbf{S} = \mathbf{I} - \mathbf{n} \otimes \mathbf{n}$ using the dyadic product (\otimes). Note that the tangential heat flux term in Eq. (40) vanishes for the first-order constitutive model (18), so that the following linear Maxwell slip condition in Cartesian coordinates is recovered [14,20,79,102]:

$$u_{\text{slip}} - u_{\text{wall}} = \omega_M \lambda \frac{\partial u}{\partial y}. \quad (42)$$

Interestingly, a previous study by Myong *et al.* [20] showed the existence of a common point (at the golden ratio $\chi=0.382$) at which both the Langmuir and Maxwell slip models yield exactly the same solutions. Furthermore, if the relationship,

$$\omega_M = f \omega, \text{ equivalently } \alpha_M = \frac{\alpha}{\alpha + f(1 - \alpha)}, \quad (43)$$

holds between the Langmuir and Maxwell slip models [20], where $f = 2\chi/(1 - \chi + \chi^2)$, then the two models yield exactly the same solutions.

3.3.3. Smoluchowski temperature jump condition

By analogy with the Maxwell velocity slip condition and introducing a thermal accommodation coefficient (σ_T), the following Smoluchowski jump boundary condition can be developed [14,43]; in dimensional form, we have

$$T_{\text{slip}} - T_{\text{wall}} = -\omega_T \frac{\lambda}{k} \frac{2\gamma}{(\gamma+1)} \frac{1}{\text{Pr}} \mathbf{Q}_{\text{normal}}, \quad (44)$$

where $\omega_T = \left(\frac{2-\sigma_T}{\sigma_T}\right)$ is the jump coefficient and $\mathbf{Q}_{\text{normal}}$ is the normal heat flux. If the constitutive relation for the heat flux is taken as being linear with the first-order Fourier law (18), then the jump condition (44) simplifies in Cartesian coordinates to

$$T_{\text{slip}} - T_{\text{wall}} = \omega_T \lambda \frac{2\gamma}{(\gamma+1)} \frac{1}{\text{Pr}} \frac{\partial T}{\partial y}. \quad (45)$$

3.4. Verification and validation of DG code

The present DG code and its variants have been verified and validated extensively in various contexts, including high-Mach-number in non-equilibrium flows [72,73,77,91,103] and multiphase dusty gas flows [104,105]. This section describes a verification and validation analysis specific to the rotating CCF problem.

3.4.1 Grid sensitivity analysis and verification using analytical solutions

First, the relative error norms of the computational results for conserved and non-conserved variables are compared against previous analytical solutions for the rotating CCF [20]. These analytical solutions were derived with isothermal and incompressible assumptions and with the Langmuir and Maxwell slip models. Comparison is also made with new analytical solutions derived for non-isothermal compressible CCF with Maxwell slip and Smoluchowski jump conditions, which are summarized in the Appendix A.

To minimize the computation time, the flow domain was reduced to one twelfth of the full geometry, and rotational periodic boundary conditions were applied on the interfaces between sub-domains. The number of grid points was varied uniformly in the radial direction, and the relative error norm was calculated by

$$L_2 \text{ norm} = \frac{1}{N_p} \sqrt{\frac{\sum_{i=1}^{N_p} (u_a - u_n)^2}{\sum_{i=1}^{N_p} u_a^2}}, \quad (46)$$

where u_a and u_n are the analytical and numerical values of the flow variables, respectively, and N_p is the total number of grid points in the radial direction.

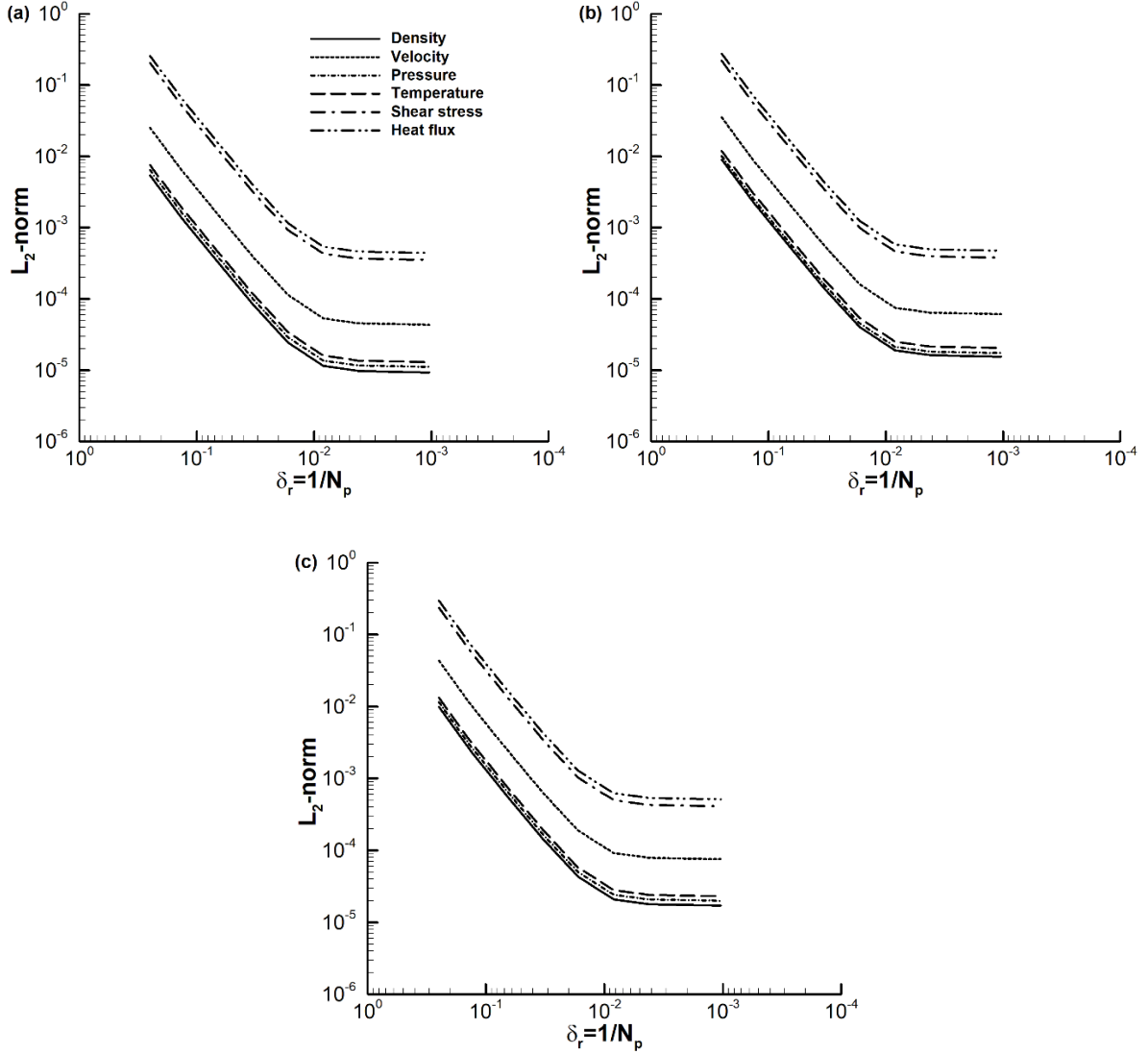


Fig. 4. Relative error norms of conserved and non-conserved variables for different nonequilibrium parameters of argon gas using first-order constitutive model without slip and jump conditions ($M = 0.5$): (a) $N_\delta = 0.001$ ($\text{Kn} = 0.002$); (b) $N_\delta = 0.025$ ($\text{Kn} = 0.05$); (c) $N_\delta = 0.25$ ($\text{Kn} = 0.5$).

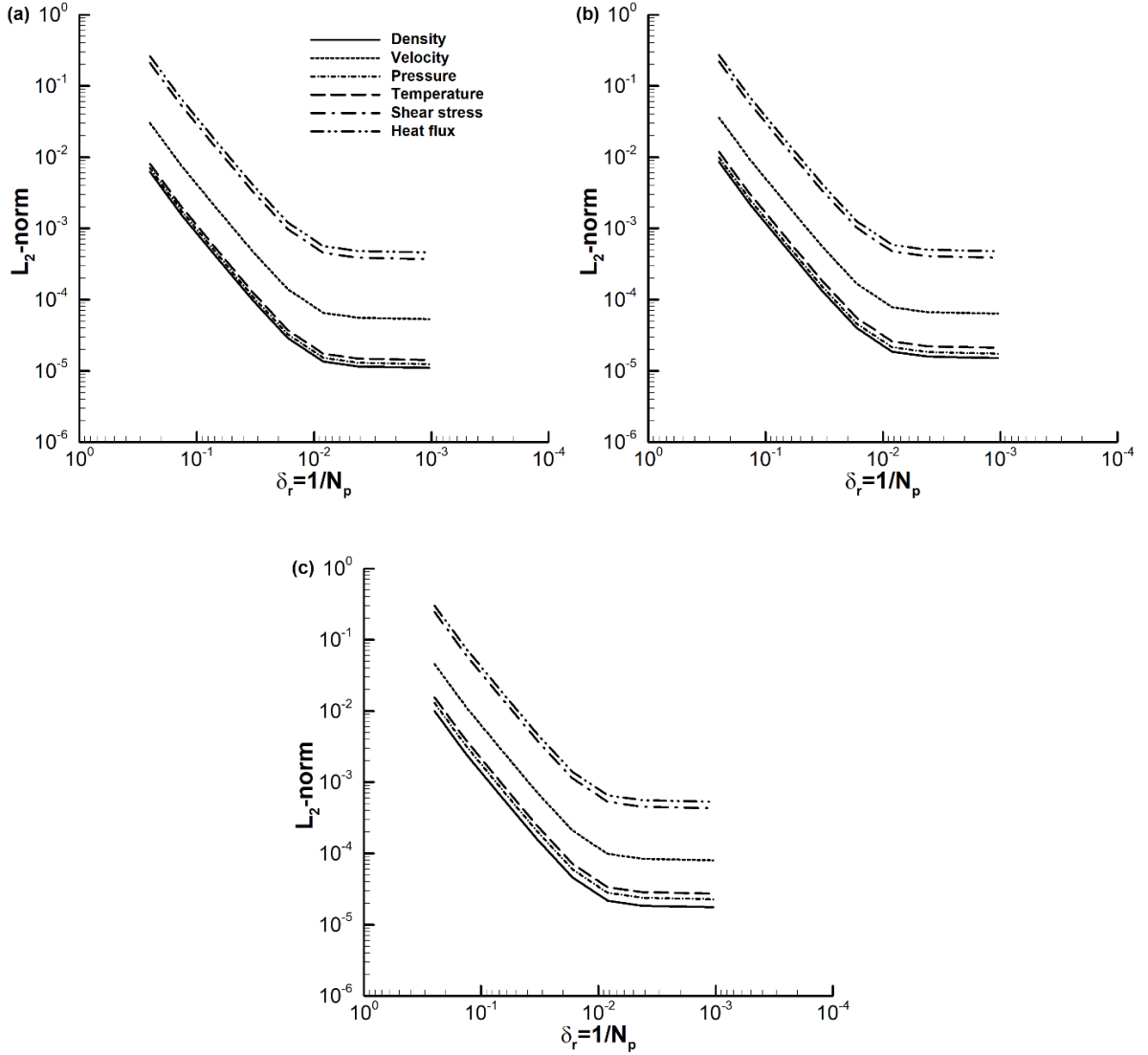


Fig. 5. Relative error norms of conserved and non-conserved variables for different nonequilibrium parameters of argon gas using first-order constitutive model with Maxwell slip and Smoluchowski jump conditions ($M = 0.5$): (a) $N_\delta = 0.001$ (Kn = 0.002); (b) $N_\delta = 0.025$ (Kn = 0.05); (c) $N_\delta = 0.25$ (Kn = 0.5).

To make the computation consistent with the analytic solutions, the flow solutions for monatomic argon gas were computed based on constant fluid properties. A computational domain with an outer-to-inner radius ratio of 2 was considered, and the non-equilibrium parameter ($N_\delta = M \cdot \text{Kn}$) was varied from 0.001 to 0.25. The cylinder walls were assumed to be isothermal, and the temperature of the confined gas was set initially to be that of the walls

(273 K). The momentum and thermal accommodation coefficients were assumed to be unity, meaning fully diffusive walls. The relative error norms were calculated for two sub-problems: (i) the first-order constitutive model without slip and jump conditions, and (ii) the first-order constitutive model with Maxwell slip and Smoluchowski jump conditions.

Figure 4 compares the relative error norms of the flow variables for different N_δ using the first-order constitutive model without slip and jump conditions. Irrespective of the values of N_δ , the relative error norms of the conserved variables remained smaller than those of the non-conserved variables. In addition, the relative error norms of the flow variables increased marginally with the nonequilibrium parameter. The non-conserved variables showed higher relative error norms than those of the conserved variables, because the former involves spatial gradients. Furthermore, note that the L_2 - norms for the flow variables attained asymptotic values with more grid points in the radial direction, making the numerical solutions close to being accurate. In the present case, the asymptote reached at the grid points with $1/N_p \leq 8.34 \times 10^{-3}$.

Figure 5 shows a similar trend in the relative error norms of the flow variables using the first-order constitutive model with the Maxwell slip and Smoluchowski jump conditions. Moreover, a further decrease in the cell size ($1/N_p$) did not affect the relative error norms, and so the results can be assumed to be accurate. Thus, this study adopted the minimum cell size of $\delta_r = 8.3334 \times 10^{-3}$ for all numerical computations.

3.4.2 Validation of numerical scheme, constitutive models, and slip and jump conditions

The present DG code was also validated with three different cases based on existing experimental data and DSMC results [7,23,29].

(a) Case I. Figure 6 compares computed results with three different data sets for density profiles (normalized with the central value): i) experimental data from Alofs *et al.* [7]; ii) DSMC results from Nanbu [32]; iii) numerical results from ANSYS FLUENT computational fluid dynamics software obtained using a user-defined function to include the Maxwell slip and Smoluchowski jump conditions. The chosen flow domain was the same as that of an experiment study conducted by Alofs *et al.* [7], where the outer-to-inner radius ratio (r_o/r_i) was taken as 1.25. The working gas was monatomic argon gas and was described based on

variable-hard-sphere molecules [47]. The initial temperatures at the inner and outer cylinders were assumed to be 303 and 311 K, respectively. Considered were three different values of the Knudsen number (0.382, 0.0819, and 0.109) with a constant Mach number of 0.9917. In the simulations, the momentum and thermal accommodation coefficients at the surfaces for the slip and jump conditions were assumed to be unity.

Figure 6 shows that at a low Knudsen number, inertial effects dominate, leading to an increase and decrease of density at the outer and inner cylinders, respectively. However, as the Knudsen number increases, confined gas is no longer entrained by the rotating inner cylinder, leading to inertial effects decaying. Consequently, gas tends to accumulate near the inner cylinder and the normalized density increases near the inner cylinder.

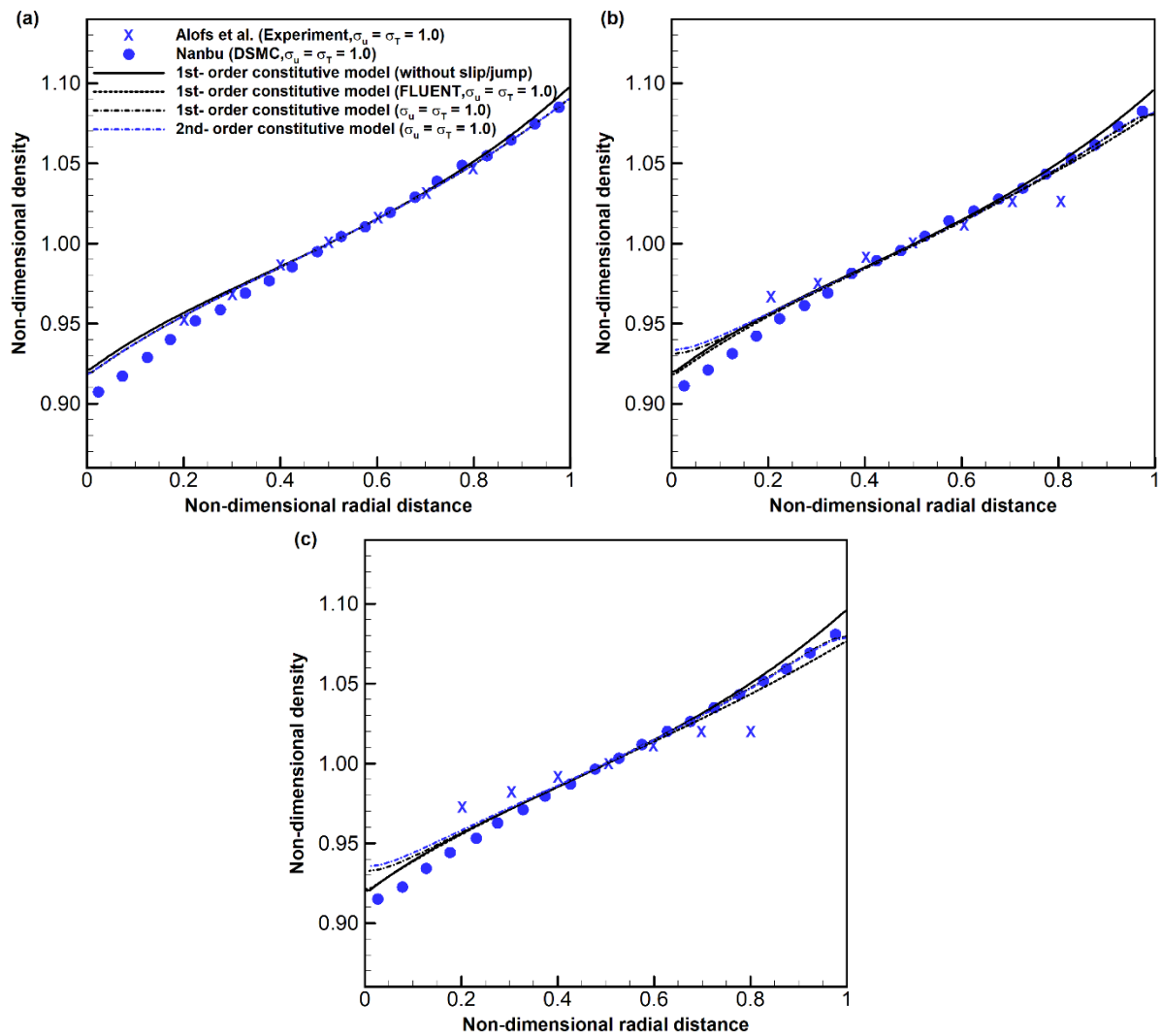


Fig. 6. Normalized density of argon gas in radial direction for three different values of Knudsen number with $M = 0.9917$: (a) $Kn = 0.0426$; (b) $Kn = 0.0819$; (c) $Kn = 0.109$.

Such behavior was discussed in detail by Khayat *et al.* [21]. According to Khayat *et al.* [21] and Nanbu [32], as the Knudsen number increases further beyond unity, there is a weak minimum in density in the vicinity of the rotating inner cylinder. The present first- and second-order constitutive models with slip and jump conditions showed no such minimum but a similar tendency near the inner cylinder with increasing Knudsen number. However, it is still the subject of debate whether a weak minimum in density indeed exists near the rotating inner cylinder in gaseous CCF.

The DSMC data obtained by Nanbu [32] in 1984 are the only simulation results available in the literature, and because of the limited computing resources available in 1984, they may suffer from nonnegligible computational errors (statistical and decomposition) manifested in the DSMC simulation [21, 32, 106]. Moreover, the experiment by Alofs *et al.* [7] suffered from a low aspect ratio (the ratio of cylinder length to diameter assumed to be one), that might add to discrepancies caused by nonnegligible three-dimensional end effects.

The first-order constitutive model without slip and jump conditions cannot predict any of these features. In addition, slight differences were found between the results of the first- and second-order constitutive models because of the non-linearity and shear-thinning feature of the second-order constitutive model.

(b) Case II. The velocity profiles are compared with the DSMC results of Tibbs *et al.* [23]. The numerical simulations were performed with a computational domain and flow parameters similar to those used for the DSMC results; $\sigma_u = 1.0$ and $\sigma_T = 0.98$ were used for the momentum and thermal accommodation coefficients, respectively, of the Maxwell and Smoluchowski slip and jump conditions. The working gas was chosen as monatomic argon gas (as tabulated in Table).

Figure 7 compares the contours and profiles (measured in radial direction) of the normalized tangential velocity obtained using the first- and second-order constitutive models with the slip and jump conditions (Langmuir and Maxwell–Smoluchowski) against the existing DSMC results [23]. As expected, the tangential velocity decreases in the radial direction. Interestingly,

the reduction in the velocity slip is smaller at the inner cylinder than at the outer cylinder. Overall, the second-order constitutive model with the slip and jump conditions matches better with the DSMC results.

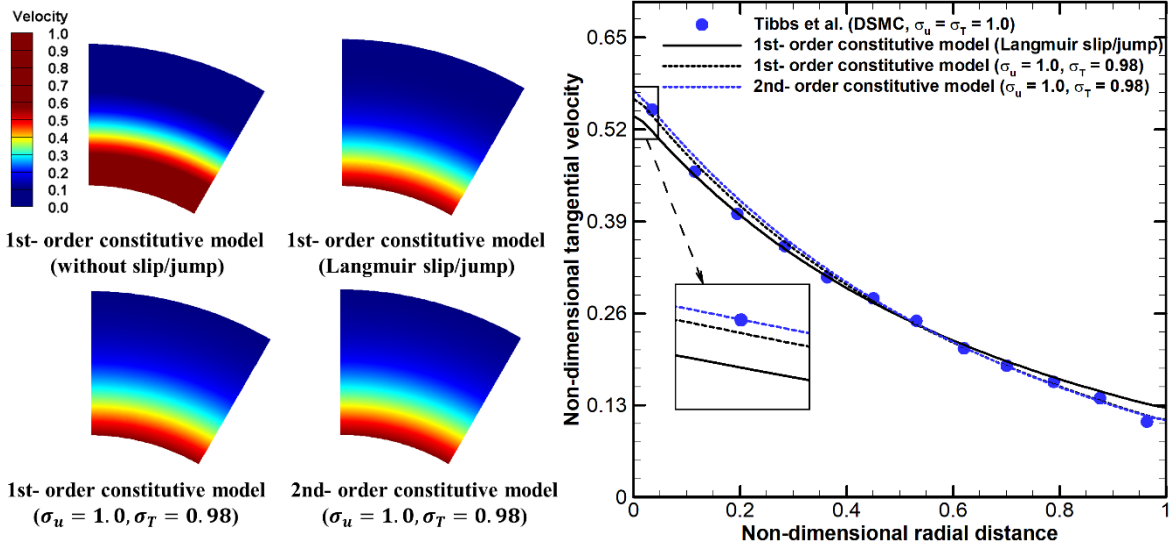


Fig. 7. Tangential velocity profiles of argon gas in radial direction for $r_0/r_i = 1.67$, $\text{Kn} = 0.5$, and $M = 0.3$.

(c) **Case III.** Computed results are compared with other DSMC results by Akhlaghi *et al.* [29]. This time, an integrated quantity is considered, i.e., the normalized torque at the inner rotating cylinder, rather than a snapshot quantity such as the velocity profile. The flow domain was defined by the outer-to-inner radius ratio $r_o/r_i = 2$. The same temperatures were assumed for the argon gas and the cylinder surfaces (273 K), and the Mach number at the inner rotating wall was selected as 0.1. Values of 0.01, 0.1, and 1.0 for the Knudsen number were considered to evaluate the performance of the first- and second-order models.

Figure 8 compares the normalized torque of argon gas at the inner rotating cylinder for varying Knudsen number with the existing DSMC results [29]. As expected, as the accommodation coefficients decrease, so does the normalized torque, particularly at high Knudsen number, because the momentum exchange with the solid surface reduces at low accommodation coefficients. As can be seen, the results of the second-order constitutive model agree better with the DSMC results [29], and this can be explained by the shear-thinning characteristics of the second-order constitutive model, which lead to reduced shear stress acting

over the cylinder surface compared to that with the first-order constitutive model [14].

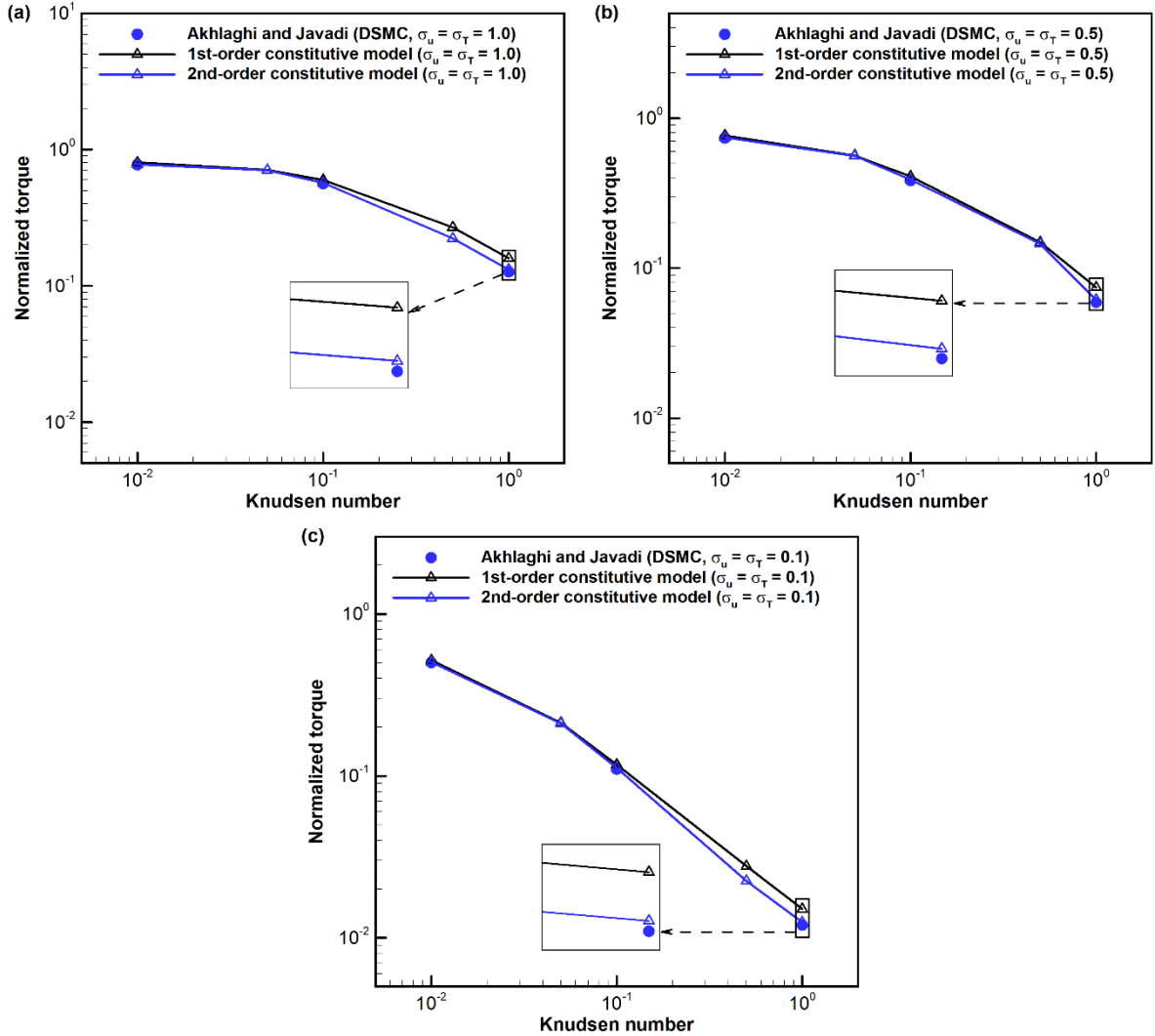


Fig. 8. Normalized torque of argon gas at inner rotating cylinder for varying Knudsen number with different values of momentum and thermal accommodation coefficients in Maxwell-Smoluchowski slip and jump conditions ($M = 0.1$): (a) $\sigma_u = \sigma_T = 1.0$; (b) $\sigma_u = \sigma_T = 0.5$; (c) $\sigma_u = \sigma_T = 0.1$.

4. Results and discussion: thermo-physical behavior of nonequilibrium diatomic and polyatomic gases in cylindrical Couette flow

This section investigates the thermo-physical characteristics of nonequilibrium monatomic, diatomic and polyatomic gases using three gases: argon ($f_b = 0.0$), nitrogen ($f_b = 0.8$), and methane ($f_b = 1.33$). The outer-to-inner radius ratio is assumed to be 2. The inner cylinder rotates with a Mach number of 0.5, while the outer cylinder is held stationary. Thus, the degree

of thermal nonequilibrium is expected to be higher near the inner cylinder.

Considered first is the role of power-law indices and gas–surface interaction parameters in the context of the first-order constitutive model. Higher-order slip/jump models such as the second-order model presented in [107,108] and a second-order model [14] obtained using the second-order NCCR values for the viscous shear stress and heat flux in Eqs. (40) and (44) are not considered here because our focus is on the effect of the second-order constitutive model on CCF. Considered next are non-classical effects of the second-order constitutive model, i.e., non-zero normal stress difference and tangential heat flux, which have been studied rarely to date. Considered finally are the effects of diatomic and polyatomic gases, i.e., nonequilibrium quantity (bulk viscosity ratio f_b) and equilibrium quantity (specific heat ratio γ).

4.1. Thermal characteristics of cylindrical Couette flow: first-order constitutive model

4.1.1 Temperature-dependent transport coefficients

To address the role of the inverse power-law index s in the transport coefficients [109], numerical simulations were performed using the first-order constitutive model with $s = 0, 0.5,$ and $1.0,$ equivalent to constant transport coefficients, hard-sphere molecules, and Maxwellian molecules, respectively. Both the momentum and thermal accommodation coefficients in the slip and jump conditions were assumed to be unity.

Figure 9 compares the profiles of normalized tangential velocity and temperature of argon gas ($f_b = 0$) with varying power-law index at values of the Knudsen number of $0.01, 0.1, 1.0$ and $\beta = 0.0$. At the low Knudsen number of $0.01,$ the tangential velocity remains insensitive to the value of s . However, when the Knudsen number is increased to $0.1,$ marginal differences are present because the effect of s is amplified far from equilibrium. A similar trend was found in the temperature profile.

Figure 10 shows the trends of the integrated quantities (torque coefficient and Stanton number at the inner rotating cylinder) of argon gas with varying power-law index ($s = 0.0, 0.5, 1.0$) and temperature difference ($\beta = 0.0, 0.05, 0.1$) for different values of the Knudsen number. The torque coefficient increases with increasing power-law index because of the enhanced intermolecular interactions. In addition, as the Knudsen number is increased, the torque coefficient increases significantly, because of the drastic reduction in

dynamic pressure $(0.5\rho u_{\theta_w}^2)$ over the total torque acting on the cylinders. Also noticed is a rise in the torque coefficient in the case of a heated inner cylinder with higher β .

The Stanton number also increases with increasing power-law index (s). As with the torque coefficient, the Stanton number increases significantly with increasing Knudsen number because of the drastic reduction in the thermal capacity of the gas $(\rho c_p u_{\theta_w} (T_{W_2} - T_{W_1}))$ over the heat flux on the inner rotating cylinder.

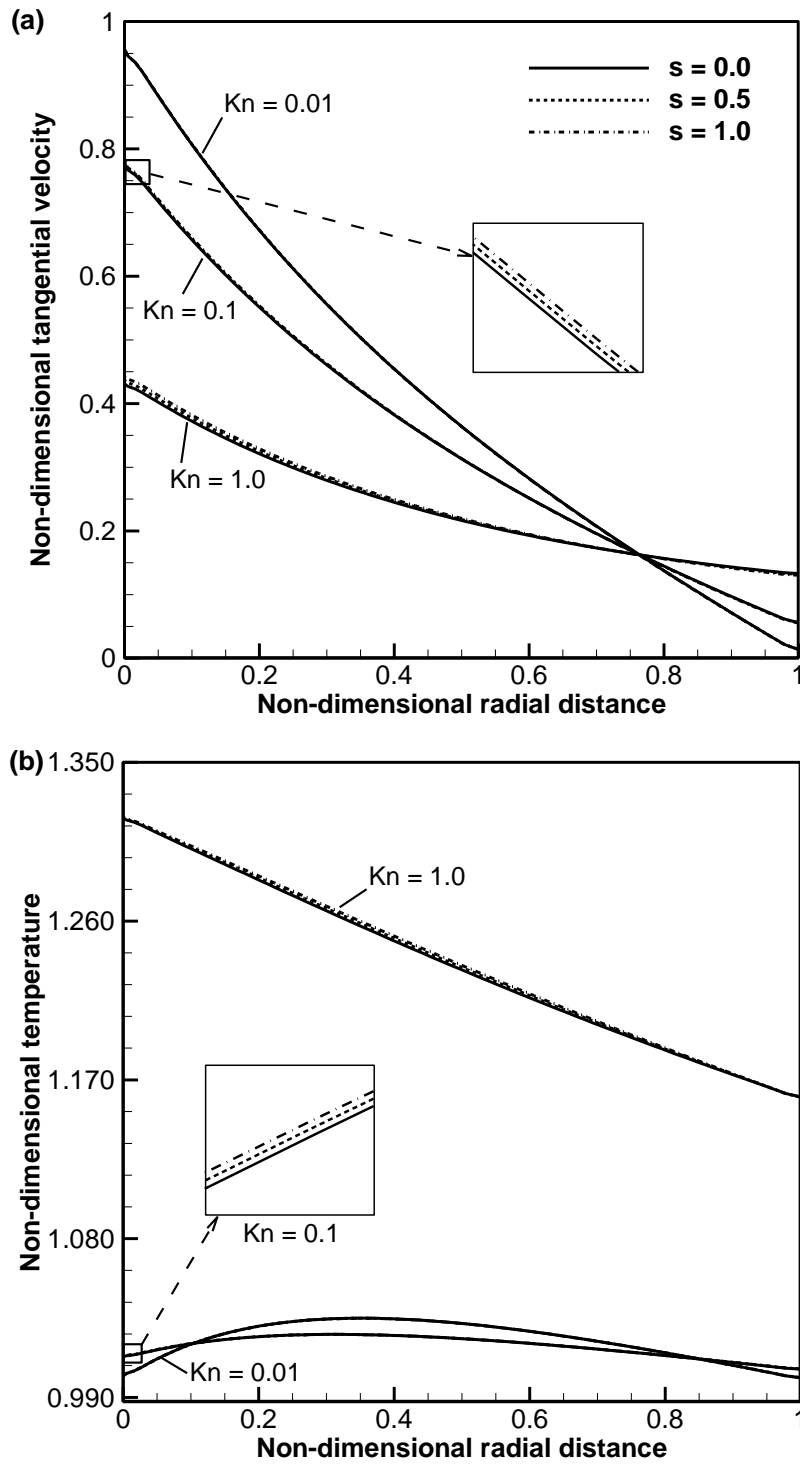


Fig. 9. Profiles of normalized (a) tangential velocity and (b) temperature of argon gas with varying power-law index ($s = 0.0, 0.5, 1.0$) in radial direction at $Kn = 0.01, 0.1, 1.0$, $\beta = 0.0$.

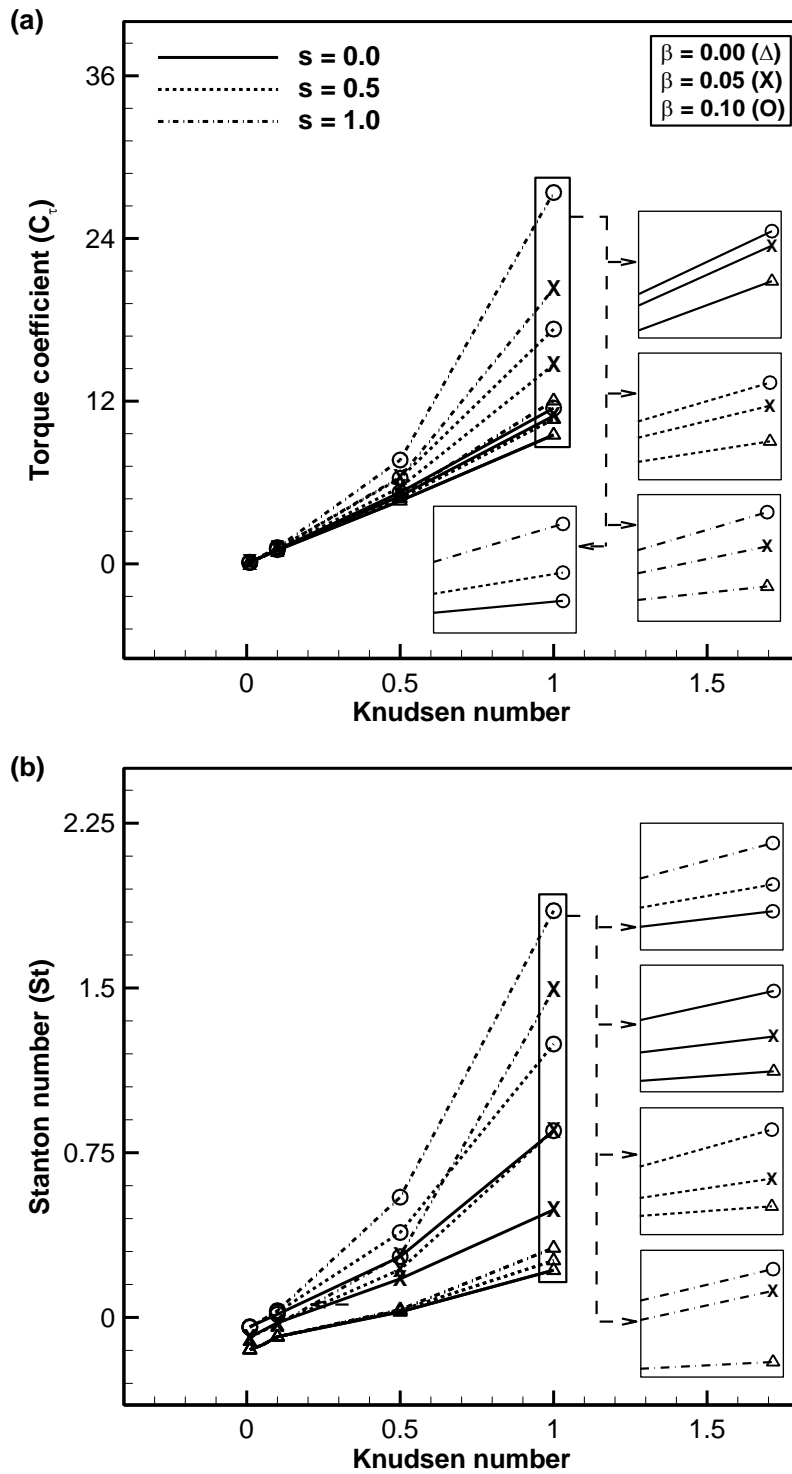


Fig. 10. Trends of integrated quantities of argon gas with varying power-law index ($s = 0.0, 0.5, 1.0$) and temperature difference ($\beta = 0.0, 0.05, 0.1$) for different values of Knudsen number (0.01, 0.05, 0.1, 0.5, 1.0): (a) torque coefficient; (b) Stanton number.

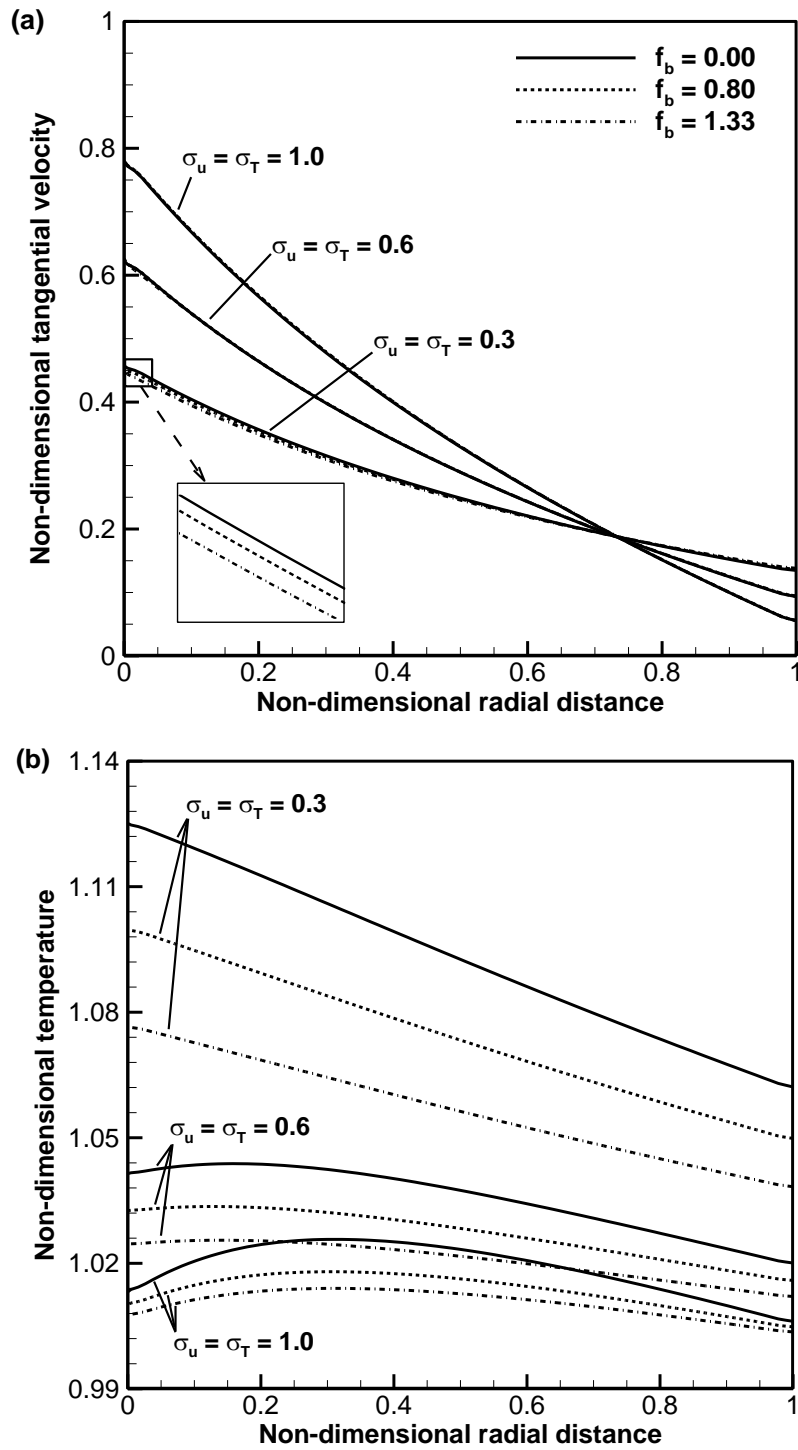


Fig. 11. Profiles of normalized tangential velocity and temperature of argon, nitrogen, and methane gases in radial direction for different accommodation coefficients at $Kn = 0.1$, $\beta = 0.0$: (a) tangential velocity; (b) temperature.

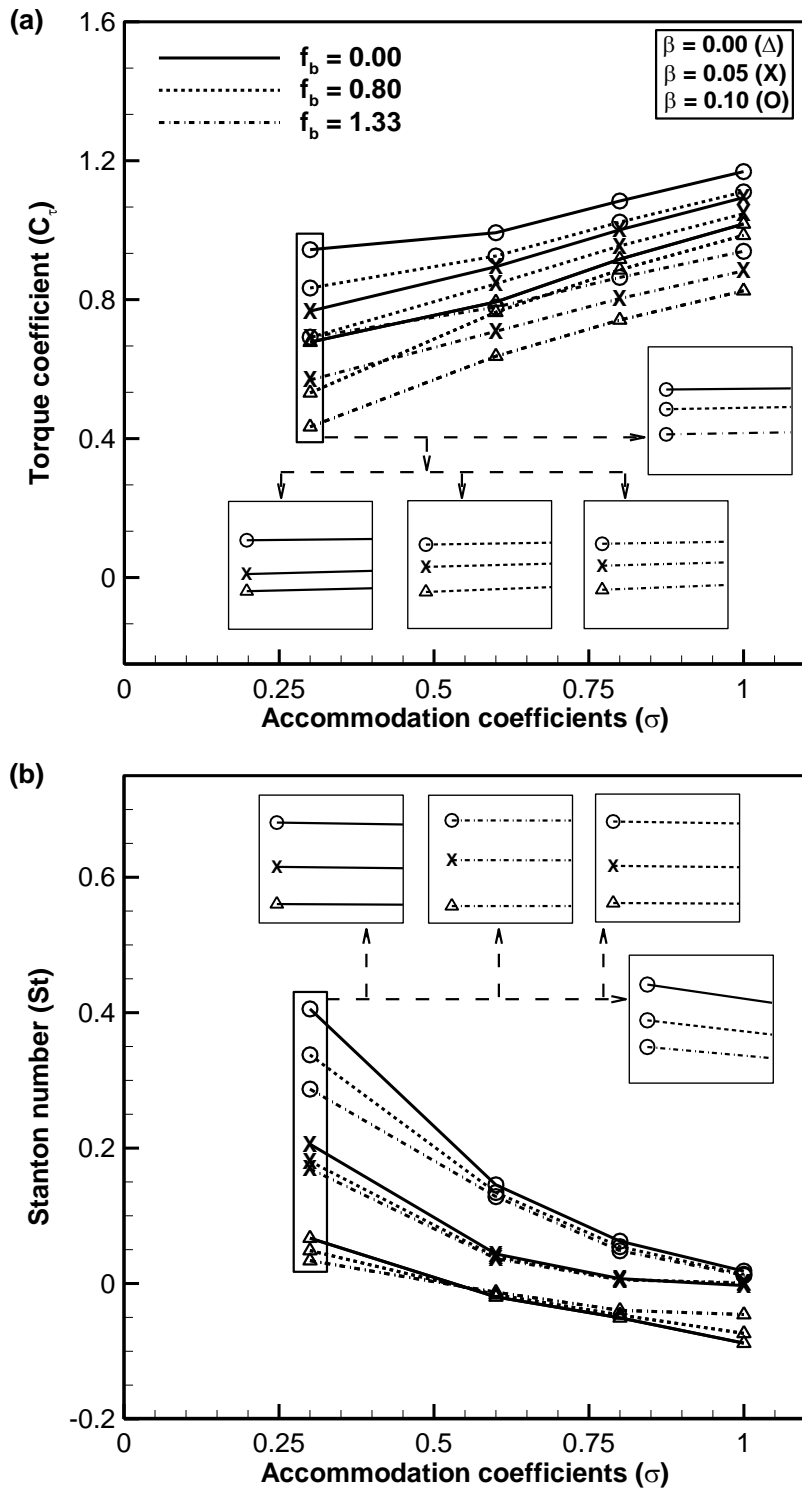


Fig. 12. Trends of integrated quantities of argon, nitrogen, and methane gases with varying accommodation coefficients ($\sigma_u = \sigma_T = 0.3, 0.6, 0.8, 1.0$) and temperature difference ($\beta = 0.0, 0.05, 0.1$) at $Kn = 0.1$: (a) torque coefficient; (b) Stanton number.

4.1.2 Gas–surface interactions including temperature jump

Investigated next is the effect of gas molecules interacting with the atoms of the solid surfaces by varying the surface accommodation coefficients. Four different momentum and thermal accommodation coefficients ($\sigma_u, \sigma_T = 0.3, 0.6, 0.8, 1.0$) are considered with the ratio of the thermal accommodation coefficient to the momentum one ($\bar{\sigma} = \sigma_T/\sigma_u$) kept at unity, thereby preserving the so-called Reynolds analogy under the slip-flow regime [96].

Figure 11 compares profiles of normalized tangential velocity and temperature of various gases with no wall temperature difference ($\beta = 0$) for different accommodation coefficients at the cylinder walls. As expected, as the accommodation coefficients decrease, the velocity slip increases at both cylinder walls. This increased velocity slip is responsible for the decrease and increase of the tangential velocity at the inner and outer cylinders, respectively, because of the reduced momentum exchange between the gas and the surface. Note also that as the accommodation coefficients are reduced to 0.3, the gas starts behaving in a specular manner and the tangential velocity deviates significantly from the actual applied velocity with $M=0.5$ [23]. The present study also confirmed the existence of a common point (around $(r - r_i)/(r_o - r_i) = 0.73$) through which all the tangential velocity profiles pass, irrespective of the value of the accommodation coefficients, which agrees with previous studies [20,23,25,28]. Moreover, note that in the case of small accommodation coefficients, some differences in the tangential velocity profiles emerge among the different gas types.

The temperature jump also increases at both cylinder walls as the accommodation coefficients decrease. Interestingly, the level of the temperature jump varies significantly with the gas type, with the monatomic gas showing the highest temperature jump because its pure translational mode contributes maximally to the heat transfer. Such variation is amplified with decreasing accommodation coefficients.

Figure 12 shows the trends of the integrated quantities (torque coefficient and Stanton number at the inner rotating cylinder) of different gases with varying accommodation coefficients and temperature difference at $Kn = 0.1$. As the accommodation coefficients decrease, so does the torque coefficient in each case because of the decreased gas surface interactions, as shown in Fig. 12 (a). Interestingly, the torque coefficient varies significantly with the gas type, with the monatomic gas having the highest value. This is because the viscous

shear stress of the monatomic gas near the inner wall contributes fully to the torque because of the absence of excess normal stress of the monatomic gas. Conversely, the substantial level of excess normal stress in diatomic and polyatomic gases takes some portion of the stress, thereby reducing the shear stress at the wall and ultimately decreasing the torque. The variation in the torque coefficient is amplified with decreasing accommodation coefficients.

The Stanton number varies significantly with the temperature difference β , as shown in Fig. 12 (b). As with the torque coefficient, its variation is amplified with decreasing accommodation coefficients. With the same wall temperature condition ($\beta = 0$), the Stanton number increases monotonically with decreasing accommodation coefficients because the heat flux Q_r at the inner wall appearing in the numerator of the definition of Stanton number is drastically increased at low accommodation coefficients. Moreover, the Stanton number decreases for diatomic and polyatomic gases because the heat capacity c_p appearing in the denominator of the definition of the Stanton number increases for diatomic and polyatomic gases.

4.2. Effects of second-order constitutive model in cylindrical Couette flow: non-zero normal stress difference and tangential heat flux

Investigated next are non-classical effects of the second-order constitutive model, specifically, non-zero normal stress difference and tangential heat flux. To the best of the author's knowledge, solutions of these quantities for diatomic and polyatomic gases using the second-order constitutive model and slip and jump conditions have not been reported previously. In the Maxwell slip and Smoluchowski jump conditions, both the momentum and thermal accommodation coefficients were assumed to be unity in all the simulations.

Before presenting the numerical results, the holistic picture of the non-classical effects is studied with the guidance of theoretical analysis of the second-order constitutive model in one-dimensional CCF in (r, θ) coordinates. After lengthy tensor manipulation, the second-order constitutive models (19), (20) reduce to the following instructive form in the present one-dimensional CCF problem ($u_r = \partial / \partial \theta = 0$) driven by the shear rate γ_s :

$$\begin{bmatrix} \hat{\Pi}_{rr} & \hat{\Pi}_{r\theta} & \hat{\Pi}_{rz} \\ \hat{\Pi}_{r\theta} & \hat{\Pi}_{\theta\theta} & \hat{\Pi}_{\theta z} \\ \hat{\Pi}_{rz} & \hat{\Pi}_{\theta z} & \hat{\Pi}_{zz} \end{bmatrix} q(c\hat{R}) = \begin{bmatrix} \underline{0} + 4\hat{\Pi}_{r\theta}/3 & \underline{1} + f_b\hat{\Delta} + \hat{\Pi}_{\theta\theta} & \underline{0} \\ \underline{1} + f_b\hat{\Delta} + \hat{\Pi}_{\theta\theta} & \underline{0} - 2\hat{\Pi}_{r\theta}/3 & \underline{0} \\ \underline{0} & \underline{0} & \underline{0} - 2\hat{\Pi}_{r\theta}/3 \end{bmatrix} \hat{\Pi}_{r\theta_0},$$

$$\hat{\Delta}q(c\hat{R}) = \underline{0} + 3\hat{\Pi}_{r\theta_0}\hat{\Pi}_{r\theta_0}, \tag{47}$$

$$\begin{bmatrix} \hat{Q}_r \\ \hat{Q}_\theta \\ \hat{Q}_z \end{bmatrix} q(c\hat{R}) = \begin{bmatrix} \underline{1} + f_b\hat{\Delta} + \hat{\Pi}_{rr} \\ \underline{0} + \hat{\Pi}_{r\theta} \\ \underline{0} \end{bmatrix} \hat{Q}_{r_0},$$

where

$$\hat{\Pi}_{r\theta_0} \equiv \frac{N_\delta}{p^*} \Pi_{r\theta_0}^* = \frac{\Pi_{r\theta_0}}{p} = \frac{-2\mu\gamma_s}{p}, \quad \gamma_s \equiv \frac{1}{2} \frac{d}{dr} \left(\frac{u_\theta}{r} \right) = \frac{1}{2} \left(\frac{du_\theta}{dr} - \frac{u_\theta}{r} \right)$$

$$\hat{Q}_{r_0} \equiv \frac{N_\delta}{p^*} \frac{Q_{r_0}^*}{\sqrt{T^*/(2\varepsilon)}} = \frac{Q_{r_0}}{p\sqrt{C_p T/(2\text{Pr})}} = \frac{-kdT/dr}{p\sqrt{C_p T/(2\text{Pr})}},$$

$$\hat{R}^2 \equiv \hat{\Pi}_{rr}^2 + \hat{\Pi}_{\theta\theta}^2 + \hat{\Pi}_{zz}^2 + 2\hat{\Pi}_{r\theta}^2 + 2\gamma' f_b \hat{\Delta}^2 + \hat{Q}_r^2 + \hat{Q}_\theta^2.$$

During the derivation, the second-order constitutive model (19) was cast in the Jaumann derivative form, which is required for constitutive equations co-rotational with the frame of reference [21]. Also included were the rotation-related terms newly appearing in the convective derivative of the shear stress tensor and the heat flux vector in (r, θ) coordinates. Here, the underlined terms $\underline{0}$, $\underline{1}$ represent the first-order driving forces in the present CCF and correspond to the Navier–Fourier constitutive relations. Note that when neglecting all coupled terms on the right-hand side of the equations (47), they reduce to the following first-order Navier–Fourier constitutive model (16):

$$\begin{bmatrix} \hat{\Pi}_{rr} & \hat{\Pi}_{r\theta} & \hat{\Pi}_{rz} \\ \hat{\Pi}_{r\theta} & \hat{\Pi}_{\theta\theta} & \hat{\Pi}_{\theta z} \\ \hat{\Pi}_{rz} & \hat{\Pi}_{\theta z} & \hat{\Pi}_{zz} \end{bmatrix} = \begin{bmatrix} 0 & 1 & 0 \\ 1 & 0 & 0 \\ 0 & 0 & 0 \end{bmatrix} \hat{\Pi}_{r\theta_0}, \quad \hat{\Delta} = 0, \quad \begin{bmatrix} \hat{Q}_r \\ \hat{Q}_\theta \\ \hat{Q}_z \end{bmatrix} = \begin{bmatrix} 1 \\ 0 \\ 0 \end{bmatrix} \hat{Q}_{r_0}. \tag{48}$$

Note from Eq. (47) that many second-order effects exist to cause the underlying physics to be governed beyond the first-order Navier–Fourier laws, such as the collisional term $q_{2nd}(c\hat{R})$

and the kinematic terms $\hat{\Pi}_{r\theta}\hat{\Pi}_{r\theta_0}$, $(f_b\hat{\Delta} + \hat{\Pi}_{\theta\theta})\hat{\Pi}_{r\theta_0}$, $(f_b\hat{\Delta} + \hat{\Pi}_{rr})\hat{Q}_{r_0}$, $\hat{\Pi}_{r\theta}\hat{Q}_{r_0}$.

Although Eq. (47) looks messy at first glance, it yields very enlightening relations among viscous stresses and heat fluxes after careful examination:

$$\begin{aligned}
\hat{\Pi}_{rr} &= -2\hat{\Pi}_{\theta\theta} = -2\hat{\Pi}_{zz}, \\
\hat{\Delta} &= -\frac{9}{2}\hat{\Pi}_{\theta\theta} \text{ or } \Delta = -\frac{9}{2}f_b\Pi_{\theta\theta}, \\
\frac{2}{3}\hat{\Pi}_{r\theta}^2 + \left[1 + \left(1 - \frac{9}{2}f_b\right)\hat{\Pi}_{\theta\theta}\right]\hat{\Pi}_{\theta\theta} &= 0, \\
\frac{\hat{Q}_r}{\hat{Q}_\theta} &= \frac{1 + f_b\hat{\Delta} + \hat{\Pi}_{rr}}{\hat{\Pi}_{r\theta}} = \frac{1 - (2 + 9f_b/2)\hat{\Pi}_{\theta\theta}}{\hat{\Pi}_{r\theta}}, \\
\hat{R}^2 &= 3\hat{\Pi}_{\theta\theta} \left\{ \left[1 + \frac{9}{2}f_b(1 + 3\gamma')\right]\hat{\Pi}_{\theta\theta} - 1 \right\} + \left[1 - \left(\frac{11}{2} + f_b\right)\hat{\Pi}_{\theta\theta} + \left(\frac{5}{2} + \frac{99}{4}f_b + \frac{81}{4}f_b^2\right)\hat{\Pi}_{\theta\theta}^2\right]\hat{Q}_{r_0}^2.
\end{aligned} \tag{49}$$

Note that all the constitutive relations can be expressed in terms of the driving forces $\hat{\Pi}_{r\theta_0}, \hat{Q}_{r_0}$, the (negative) normal stress $\hat{\Pi}_{\theta\theta}$, and the gas coefficients γ, c, f_b . Combining Eqs. (47) and (49) gives the implicit non-Navier–Fourier nonlinear coupled constitutive relations

$$\begin{aligned}
\hat{\Pi}_{\theta\theta} &= -\frac{2(1 + f_b\hat{\Delta})\hat{\Pi}_{r\theta_0}^2}{3q^2(c\hat{R}) + 2\hat{\Pi}_{r\theta_0}^2} = -\frac{2\hat{\Pi}_{r\theta_0}^2}{3q^2(c\hat{R}) + (2 - 9f_b)\hat{\Pi}_{r\theta_0}^2}, \\
\hat{\Pi}_{r\theta} &= \frac{3(1 + f_b\hat{\Delta})q(c\hat{R})\hat{\Pi}_{r\theta_0}}{3q^2(c\hat{R}) + 2\hat{\Pi}_{r\theta_0}^2} = \frac{3q(c\hat{R})\hat{\Pi}_{r\theta_0}}{3q^2(c\hat{R}) + (2 - 9f_b)\hat{\Pi}_{r\theta_0}^2}, \\
\hat{\Delta} &= \frac{9\hat{\Pi}_{r\theta_0}^2}{3q^2(c\hat{R}) + (2 - 9f_b)\hat{\Pi}_{r\theta_0}^2}, \\
\hat{Q}_r &= \frac{3\left(q(c\hat{R}) + 6\hat{\Pi}_{r\theta_0}^2/q(c\hat{R})\right)(1 + f_b\hat{\Delta})}{3q^2(c\hat{R}) + 2\hat{\Pi}_{r\theta_0}^2}\hat{Q}_{r_0} = \frac{3\left(q(c\hat{R}) + 6\hat{\Pi}_{r\theta_0}^2/q(c\hat{R})\right)}{3q^2(c\hat{R}) + (2 - 9f_b)\hat{\Pi}_{r\theta_0}^2}\hat{Q}_{r_0}, \\
\hat{Q}_\theta &= \frac{3(1 + f_b\hat{\Delta})\hat{\Pi}_{r\theta_0}}{3q^2(c\hat{R}) + 2\hat{\Pi}_{r\theta_0}^2}\hat{Q}_{r_0} = \frac{3\hat{\Pi}_{r\theta_0}}{3q^2(c\hat{R}) + (2 - 9f_b)\hat{\Pi}_{r\theta_0}^2}\hat{Q}_{r_0}.
\end{aligned} \tag{50}$$

Surprisingly, Eqs. (49) and (50) turn out to be the same as the second-order Boltzmann–

Curtiss-based constitutive model in the velocity shear flow problem in Cartesian coordinates [14,17,47,70,88] with the following correspondences:

$$\Pi_{r\theta} \leftrightarrow \Pi_{xy}, \Pi_{\theta\theta} \leftrightarrow \Pi_{xx}, \Pi_{rr} \leftrightarrow \Pi_{yy}.$$

Therefore, the signs and qualitative properties of the viscous stresses and heat fluxes remain essentially the same. In addition, most of the non-classical physics present in the velocity shear flow in Cartesian coordinates carries over to the present CCF in (r, θ) coordinates. For example, the third relation in Eq. (49) is nothing but the kinematic viscous stress constraint for diatomic gases first identified by Myong [70] in 2004. The existence of such a stress constraint, as shown in Fig. 2, means that when the diatomic and polyatomic gases with a specific value of f_b undergo velocity shear, the viscous shear and normal stress $(\Pi_{r\theta}, \Pi_{\theta\theta})$ (in reference to the hydrostatic pressure) are not independent at all and must be determined along a topological curve defined by a conic section (an ellipse for $f_b < 2/9$, a parabola at $f_b = 2/9$, or a hyperbola for $f_b > 2/9$) in the phase space [88].

4.2.1 Normal stress difference

Figure 13 (a) shows the profiles of the normalized tangential velocity u_θ and the normalized normal stress difference $(\Pi_{\theta\theta} - \Pi_{rr})$ of argon ($f_b = 0.0$) in radial direction. The first- and second-order constitutive models were used in conjunction with the Maxwell slip and Smoluchowski jump conditions ($\text{Kn} = 0.1, 1.0$).

As first noted in Fig. 8, the shear-thinning characteristic of the second-order constitutive model shown in Fig. 3 (b) is responsible for the smaller velocity slip and shear stress compared to those with the first-order constitutive model. Specifically, the second equation of Eq. (50) indicates that the second-order shear stress $\Pi_{r\theta}$ is smaller than the first-order shear stress $\Pi_{r\theta_0}$ because the following factor is always less than 1:

$$\frac{1}{3q(c\hat{R}) + (2 - 9f_b)\hat{\Pi}_{r\theta_0}^2 / 3 / q(c\hat{R})}.$$

This allows the tangential velocity profile to have a higher slope for a given driving force $\Pi_{r\theta_0} = -2\mu\gamma_s$, which in turn leads to a smaller velocity slip at the wall. The difference is amplified with increasing Knudsen or Mach number.

The bottom of Fig. 13 (a) shows an important non-classical second-order effect, i.e., a non-zero normal stress difference in states away from thermal equilibrium. The origin of this behavior is traced to the relation $\hat{\Pi}_{\theta\theta} - \hat{\Pi}_{rr} = 3\hat{\Pi}_{\theta\theta} = -2\hat{\Pi}_{r\theta}\hat{\Pi}_{r\theta_0}$ in Eqs. (47), (49), and (50), implying that it remains always negative (with a quadratic function near thermal equilibrium, $\hat{\Pi}_{r\theta_0}^2$) and does not vanish unless the shear driving force $\Pi_{r\theta_0} = -2\mu\gamma_s$ is absent. Again, the difference is amplified with increasing Knudsen or Mach number. In contrast, the first-order constitutive model cannot describe this abnormal property at all because all the second-order coupling effects were ignored from the outset.

Figure 13 (b) shows the profiles of the normalized tangential velocity and normal stress difference of gas with $f_b = 1.0$ in radial direction. The specific heat ratio was fixed as $\gamma = 5/3$ to isolate the effect of the bulk viscosity ratio. The qualitative trend remains the same as that for argon gas with $f_b = 0.0$, but the normal stress difference is increased substantially at $\text{Kn} = 1.0$.

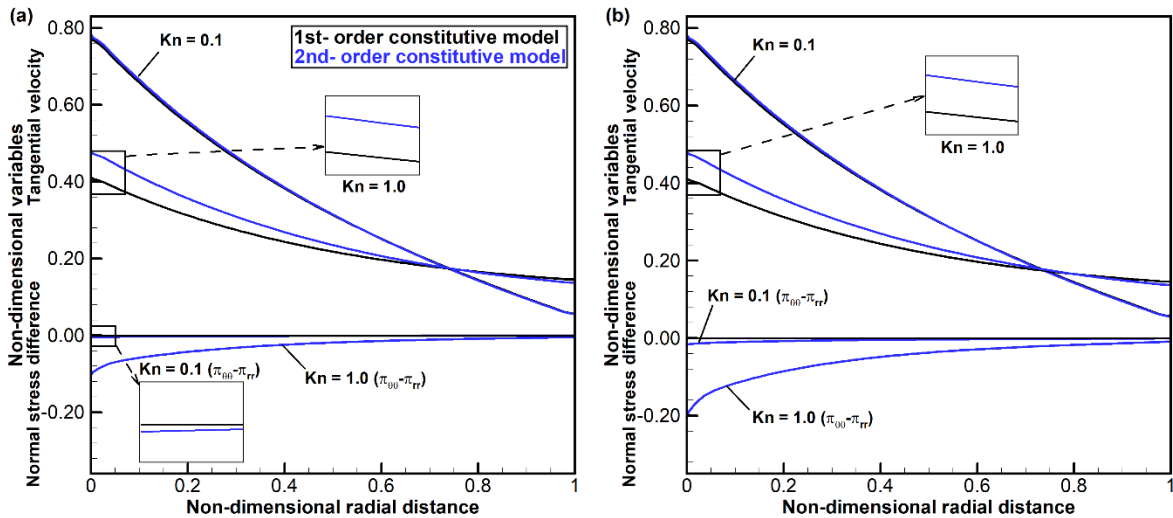


Fig. 13. Profiles of non-classical normal stress difference of gas ($\gamma = 5/3$) in the radial direction at $\text{Kn} = 0.1, 1.0$, $\beta = 0.0$: (a) $f_b = 0.0$; (b) $f_b = 1.0$.

4.2.2 Tangential heat flux

The top of Fig. 14 (a) shows profiles of the normalized temperature with the first- and second-order constitutive models. Even though the difference between the first- and second-order constitutive models is much smaller than that in the tangential velocity profiles, the slope

of the temperature profile with the second-order model is larger than that with the first-order model. This is again caused by the factor $[3q(c\hat{R}) + (2 - 9f_b)\hat{\Pi}_{r\theta}^2 / 3 / q(c\hat{R})]^{-1}$ in the second-order constitutive relation [the fifth equation of Eq. (50)].

The bottom of Fig. 14 (a) shows another important non-classical second-order effect, i.e., a non-zero tangential heat flux in states away from thermal equilibrium. The origin of this behavior is traced to the second-order coupling term on the right-hand side of the constitutive relation of the tangential heat flux, $\hat{Q}_\theta q(c\hat{R}) = \hat{\Pi}_{r\theta} \hat{Q}_{r_0}$, in Eqs. (47) and (50). Because the sign of the shear stress $\hat{\Pi}_{r\theta}$ is positive in the present flow with a rotating inner cylinder, the sign of the tangential heat flux \hat{Q}_θ is the same as that of the first-order radial heat flux \hat{Q}_{r_0} . As with other non-classical quantities, the tangential heat flux is amplified with increasing Knudsen or Mach number. In contrast, it remains strictly zero with the first-order constitutive model because the second-order coupling term was ignored from the outset.

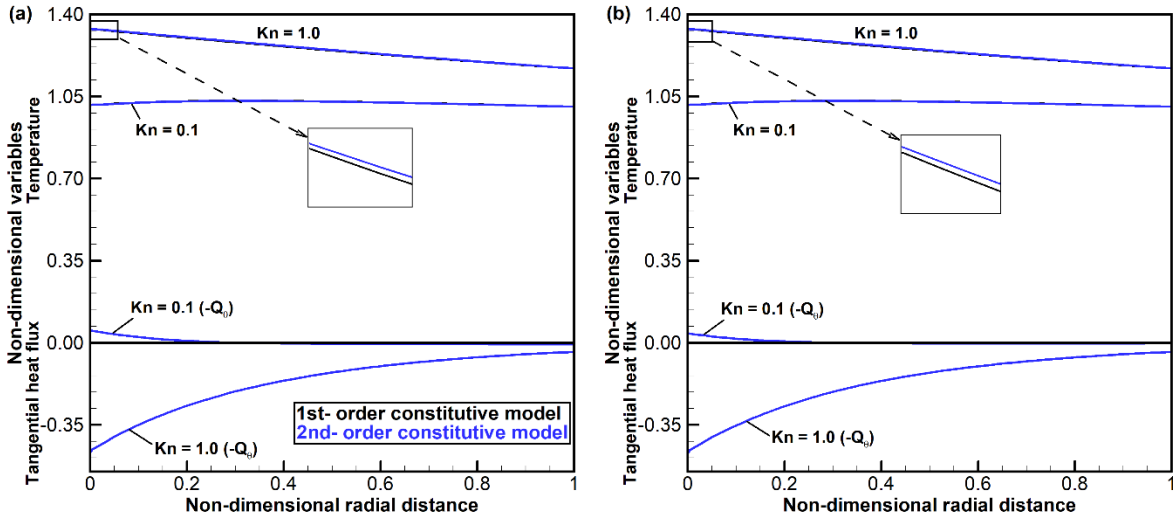


Fig. 14. Profiles of non-classical tangential heat flux of gas ($\gamma = 5/3$) in radial direction at $\text{Kn} = 0.1, 1.0$, $\beta = 0.0$: (a) $f_b = 0.0$; (b) $f_b = 1.0$.

Figure 14 (b) shows profiles of the normalized temperature and tangential heat flux of gas with $f_b = 1.0$ in radial direction. The specific heat ratio was fixed as $\gamma = 5/3$ to isolate the effect of the bulk viscosity ratio. The profiles remain almost the same as those for argon gas with $f_b = 0.0$ because the bulk viscosity affects the viscous stress directly but the heat flux

indirectly to a negligible degree.

4.2.3 Torque coefficient and Stanton number for varying Knudsen number and temperature difference

Figure 15 shows the trends of the integrated quantities (torque coefficient and Stanton number at the inner rotating cylinder) of argon gas obtained using the first- and second-order constitutive models for different values of the Knudsen number. The torque coefficient increases monotonically with the Knudsen number because of the drastic reduction in dynamic pressure over the total torque acting on the cylinder surface, irrespective of the temperature difference imposed on the cylinder walls. Interestingly, a reduction in the torque coefficient is observed in the second-order constitutive model. This is caused by the shear-thinning characteristic of the second-order constitutive model, which is shown in the second relation in Eq. (50).

The trends of the Stanton number are similar to those of the torque coefficient: it increases with the Knudsen number and decreases with the second-order constitutive model. The origin of this behavior can be traced to the reduced heat flux of the second-order constitutive model:

$$\frac{\hat{Q}_r}{\hat{Q}_{r_0}} = \frac{1 + 6\hat{\Pi}_{r\theta_0}^2 / q^2(c\hat{R})}{q(c\hat{R}) + 2\hat{\Pi}_{r\theta_0}^2 / 3 / q(c\hat{R})}.$$

As expected, a reduction in the torque coefficient and the Stanton number is amplified with increasing Knudsen number.

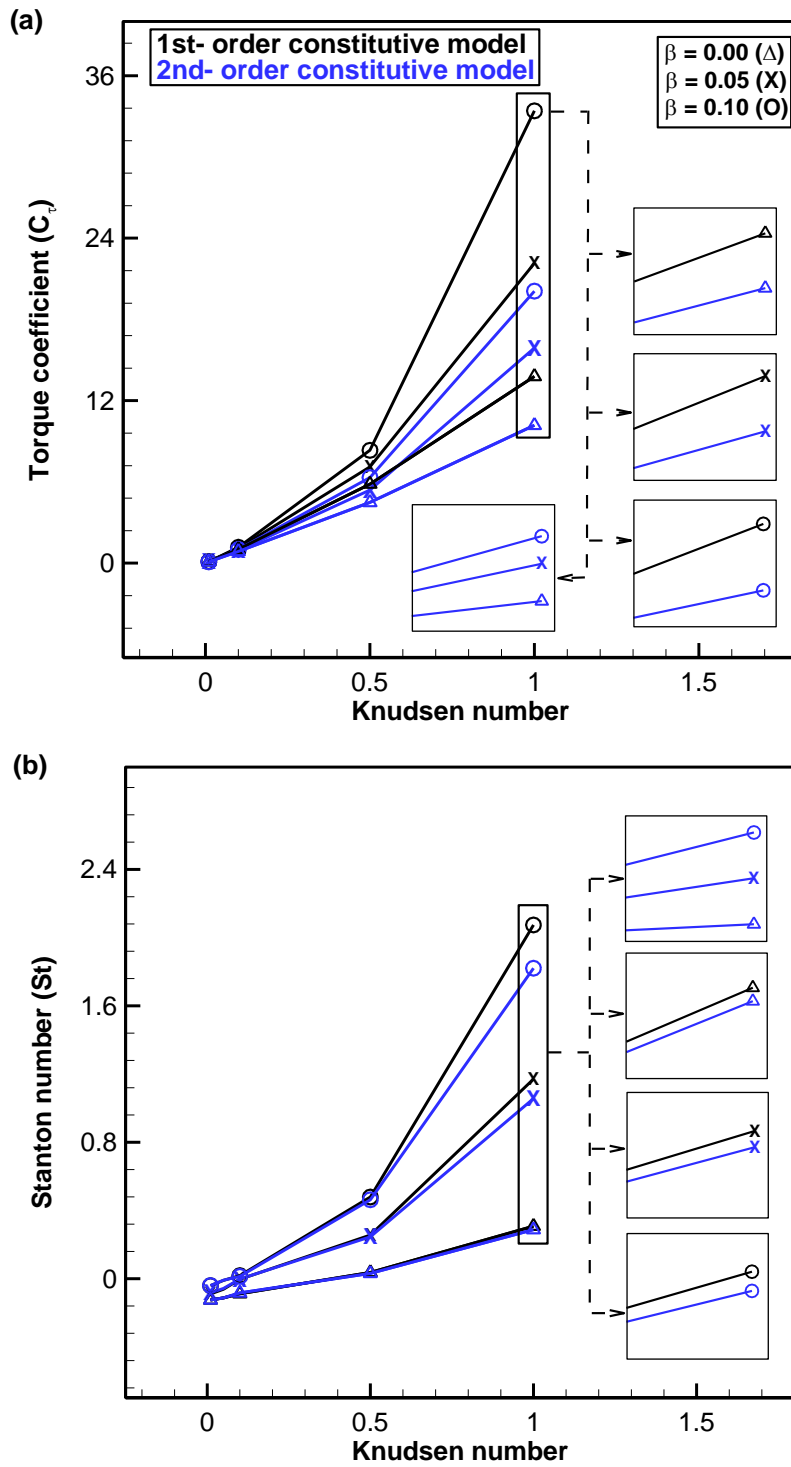


Fig. 15. Trends of integrated quantities of argon ($f_b = 0.0$) gas for different values of Knudsen number and temperature difference parameter ($\beta = 0.0, 0.05, 0.1$): (a) torque coefficient; (b) Stanton number.

4.3 Effects of diatomic and polyatomic gases in cylindrical Couette flow: non-equilibrium quantity f_b and equilibrium quantity γ

To investigate the effects of diatomic and polyatomic gases in CCF in a clearer way, the specific heat ratio is normalized between zero and one using the relationship

$$\bar{\gamma} = \frac{(5/3 - \gamma)}{2(\gamma_{(\text{bound})} - 5/3)} = \frac{(5/3 - \gamma)}{2(2 - 5/3)}, \quad (45)$$

where $\gamma_{(\text{bound})} = 2$ refers to the upper bounding limit for the specific heat ratio. This normalization bounds different gas types between monatomic and polyatomic gas molecules. All the other gas parameters are assumed to be the same as those for nitrogen gas. Table II summarizes the bulk viscosity coefficient (f_b) and normalized specific heat ratio ($\bar{\gamma}$) of the different gases considered in this study.

Table II. Bulk viscosity coefficient (f_b) and normalized specific heat ratio ($\bar{\gamma} = (5/3 - \gamma)/(2 \times (\gamma_{(\text{bound})} - 5/3))$) of different gases with $\gamma_{(\text{bound})} = 2$.

Gas parameter	Bulk viscosity coefficient (f_b)	Heat capacity ratio ($\bar{\gamma}$)
Gases (with varying f_b) Figs. 16, 17	$f_b = 0.0$	$\bar{\gamma} = 0.4$ ($\gamma = 7/5$)
	$f_b = 0.5$	(constant)
	$f_b = 1.0$	
Gases (with varying $\bar{\gamma}$) Figs. 18, 19	$f_b = 0.0$ (constant)	$\bar{\gamma} = 0.125$ ($\gamma = 19/12$)
		$\bar{\gamma} = 0.4$ ($\gamma = 7/5$)
		$\bar{\gamma} = 0.625$ ($\gamma = 5/4$)
Real gases Figs. 20, 21	Argon: $f_b = 0.0$	$\bar{\gamma} = 0.0$ ($\gamma = 5/3$)
	Nitrogen: $f_b = 0.8$	$\bar{\gamma} = 0.4$ ($\gamma = 7/5$)
	Methane: $f_b = 1.33$	$\bar{\gamma} = 0.531$ ($\gamma = 1.312$)

4.3.1 Varying nonequilibrium quantity: bulk viscosity ratio f_b

The thermo-physical characteristics of the gases are investigated by firstly varying the bulk viscosity ratio ($f_b = 0.0, 0.5, 1.0$) in a highly rarefied flow regime. The specific heat ratio is fixed as $\bar{\gamma} = 0.4$ (equivalently, $\gamma = 1.4$) to isolate the effect of the bulk viscosity ratio.

Figure 16 compares the profiles of the conserved (pressure, density, temperature) and non-conserved (excess normal stress) variables of the gases with varying bulk viscosity ratio ($f_b = 0.0, 0.5, 1.0$) in the radial direction at $\text{Kn} = 1.0$, $\beta = 0.0$. The slope of the pressure distribution in the radial direction reduces with increasing bulk viscosity ratio, thereby increasing the pressure at the inner cylinder wall. This phenomenon can be explained by examining the five terms in the conservation law of radial momentum (23):

$$-\rho \frac{u_\theta^2}{r} + \frac{dp}{dr} + \frac{d\Delta}{dr} + \frac{d\Pi_{rr}}{dr} + \frac{\Pi_{rr} - \Pi_{\theta\theta}}{r} = 0.$$

As the bulk viscosity ratio increases, the normal stress difference with positive sign, $(\Pi_{rr} - \Pi_{\theta\theta})/r$, increases and competes with the centripetal force term $-\rho u_\theta^2/r$. To balance this change in the conservation law, the non-viscous term dp/dr should be reduced, thereby increasing the pressure at the inner cylinder wall. The reduction in the slope of the pressure distribution is amplified more in the second-order model than in the first-order model because of the shear-thinning characteristic of the former [88]. Note that the trend in the density profiles is the same as that in the pressure profiles. As the bulk viscosity increases, the density profiles of the second-order constitutive model are flattened more than are those of the first-order constitutive model. This is because the density is directly proportional to the pressure through the equation of state.

The rotational energy of the diatomic and polyatomic gases deviates from thermal equilibrium when subjected to strong non-equilibrium, and the process of relaxation to equilibrium conditions can be represented in terms of the bulk viscosity [110]. Such relaxation is effectively absorbed by the excess normal stress term, as shown in Fig. 16 (c). In the present theory, non-zero excess normal stress can be explained by a second-order relation, $\Delta = -9f_b\Pi_{\theta\theta}/2$, in Eqs. (49) and (50), indicating the direct relationship with the normal stress. Note that the excess normal stress remains finite in the second-order theory, even if the divergence of velocity vanishes. In contrast, the excess normal stress always remains zero when the Stokes' hypothesis [111] is adopted or the divergence of velocity vanishes, as in the present CCF.

Figure 16 (d) shows that the temperature distributions remain similar for increasing bulk

viscosity ratio. In addition, the second-order constitutive model predicted only marginal increase in the gas temperature compared to the first-order model.

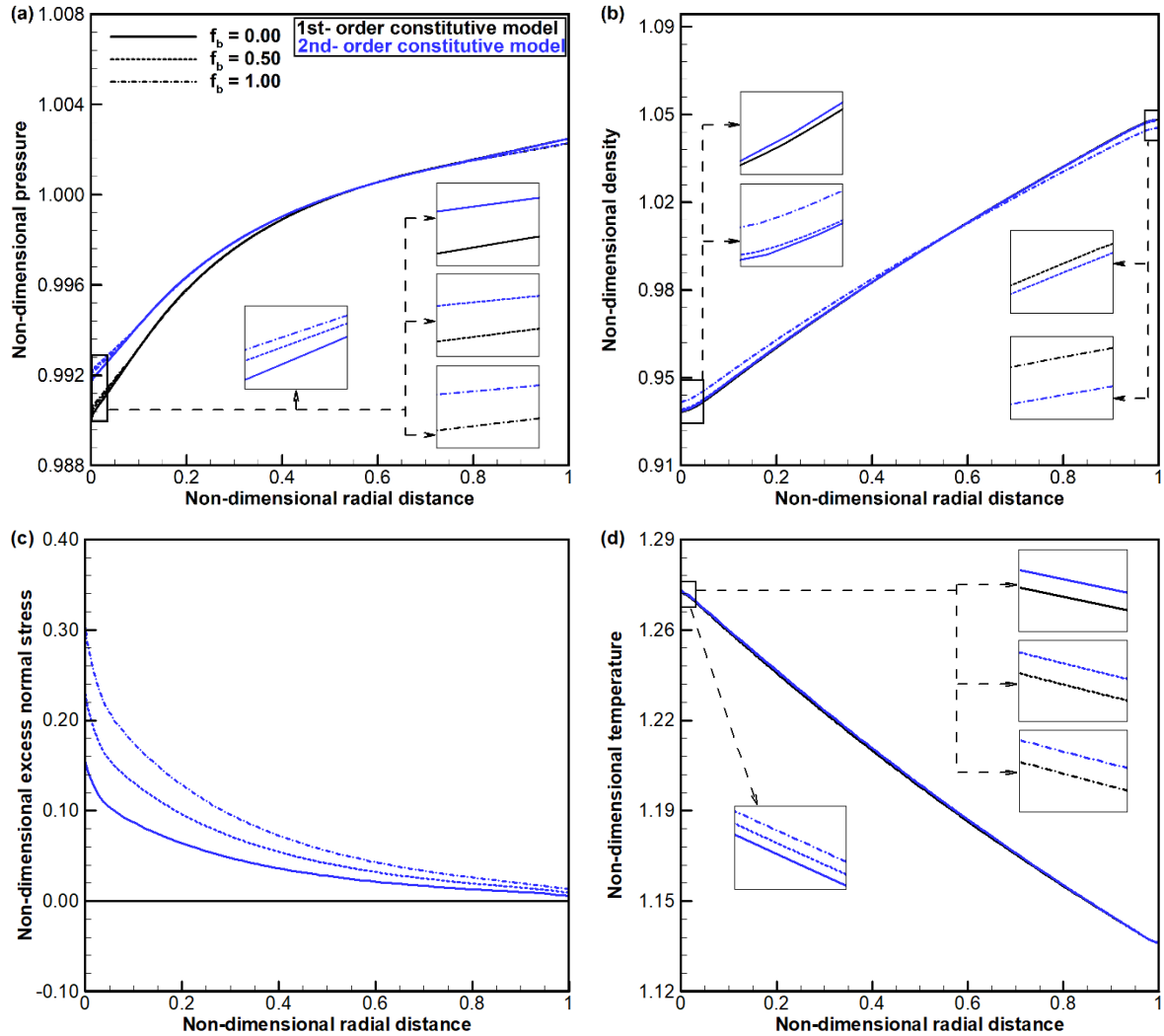


Fig. 16. Profiles of conserved and non-conserved variables of gases ($\bar{\gamma} = 0.4$) with varying bulk viscosity ratio ($f_b = 0.0, 0.5, 1.0$) in radial direction at $Kn = 1.0$, $\beta = 0.0$: (a) pressure; (b) density; (c) excess normal stress; (d) temperature.

Figure 17 shows the trends of the integrated quantities (torque coefficient and Stanton number at the inner rotating cylinder) of gases with fixed $\bar{\gamma} = 0.4$ and varying bulk viscosity ratio ($f_b = 0.0, 0.5$, and 1.0) for different values of the Knudsen number. The torque coefficient increases slightly with increasing bulk viscosity ratio, and the increase is amplified with increasing Knudsen number. In addition, a negligible increase was found in the Stanton number with increasing bulk viscosity ratio, even at the high Knudsen number of $Kn=1.0$.

Moreover, it was observed that the temperature difference has no impact on the role of the bulk viscosity ratio. A theoretical explanation for the slight increase of torque coefficient and Stanton number is possible when recalling the second and fifth equations of the NCCR (50). Specifically, the factor $[3q(c\hat{R}) + (2 - 9f_b)\hat{\Pi}_{r_0}^2 / 3 / q(c\hat{R})]^{-1}$ increases with increasing bulk viscosity ratio f_b , thereby increasing the viscous shear stress and radial heat flux at the inner cylinder wall.

4.3.2 Varying equilibrium quantity: specific heat ratio γ

The thermo-physical characteristics of gases are investigated further by varying the specific heat ratio in a highly rarefied flow regime. This time, the bulk viscosity ratio is fixed a $f_b = 0.0$ to isolate the effect of the specific heat ratio. As summarized in Table I, only those parameters that depend on the specific heat ratio are varied, and the other gas parameters such as the viscosity index s are kept the same as those of nitrogen gas.

Figure 18 compares the profiles of the tangential velocity and temperature of gases with different specific heat ratio ($\bar{\gamma} = 0.125, 0.4, 0.625$) in the radial direction at $\text{Kn} = 1.0$, $\beta = 0.0$. As the normalized specific heat ratio increases (or the actual value of the specific heat ratio decreases), both the tangential velocity and temperature decrease. This reduction can be explained by checking the terms in the conservation law of energy (13):

$$\Pi^* \cdot \mathbf{u}^* / (M \sqrt{\gamma RT_r}) + \mathbf{Q}^* / (\text{Ec Pr}) = \text{constant} .$$

Because the specific heat ratio γ is an equilibrium quantity and appears in the definitions of the Eckert number and the Prandtl number, it directly affects the overall flow field. For a given Mach number ($M=0.5$), the parameter $1/\text{EcPr}$ in the conservation law of energy increases via $(9\gamma-5)/(\gamma-1)/\gamma$ with decreasing specific heat ratio γ , thereby resulting in smaller heat flux \mathbf{Q}^* and lower temperature near the inner cylinder. Similarly, the reduced specific heat ratio results in smaller viscous stress Π^* and lower velocity near the inner cylinder. As in the previous cases, compared to the first-order constitutive model, the second-order constitutive model with its shear-thinning property predicted larger tangential velocity near the inner cylinder.

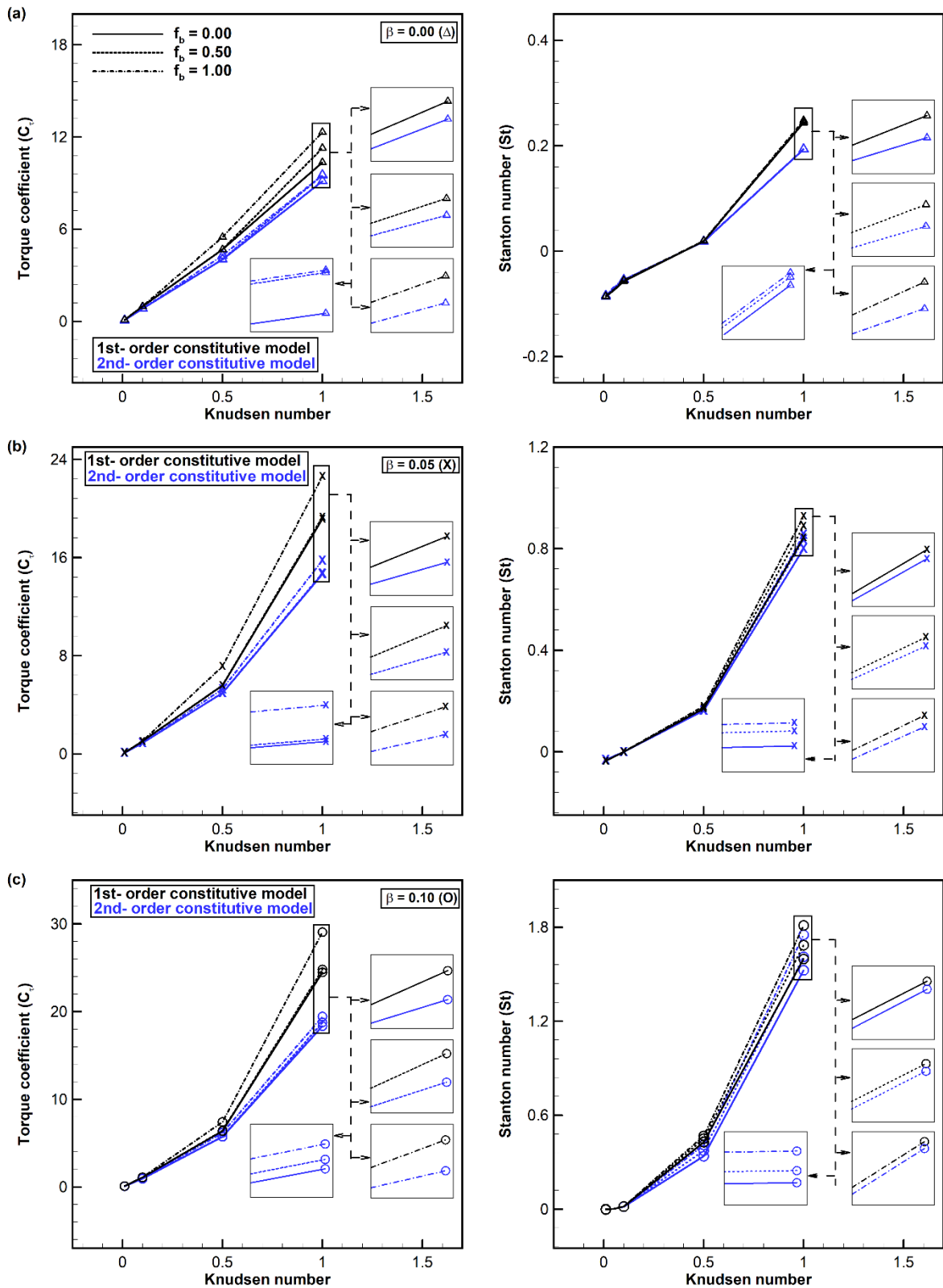


Fig. 17. Trends of integrated quantities of gases ($\bar{\gamma} = 0.4$) with bulk viscosity ratio ($f_b = 0.0, 0.5, 1.0$) for different Knudsen number: (a) $\beta = 0.0$; (b) $\beta = 0.05$; (c) $\beta = 0.1$.

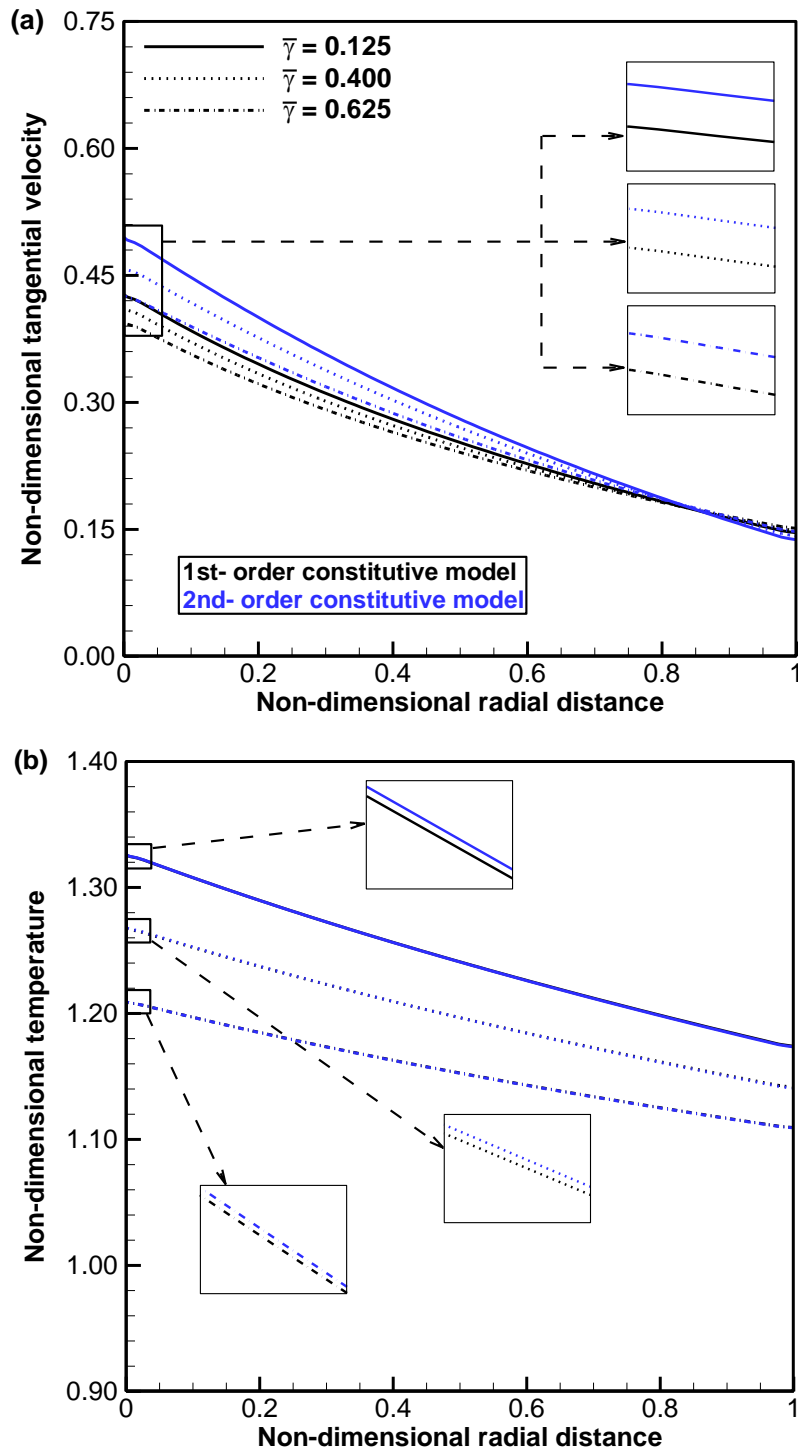


Fig. 18. Profiles of tangential velocity and temperature of gases ($f_b = 0.0$) with normalized specific heat ratio ($\bar{\gamma} = 0.125, 0.4, 0.625$) in radial direction at $Kn = 1.0$, $\beta = 0.0$.

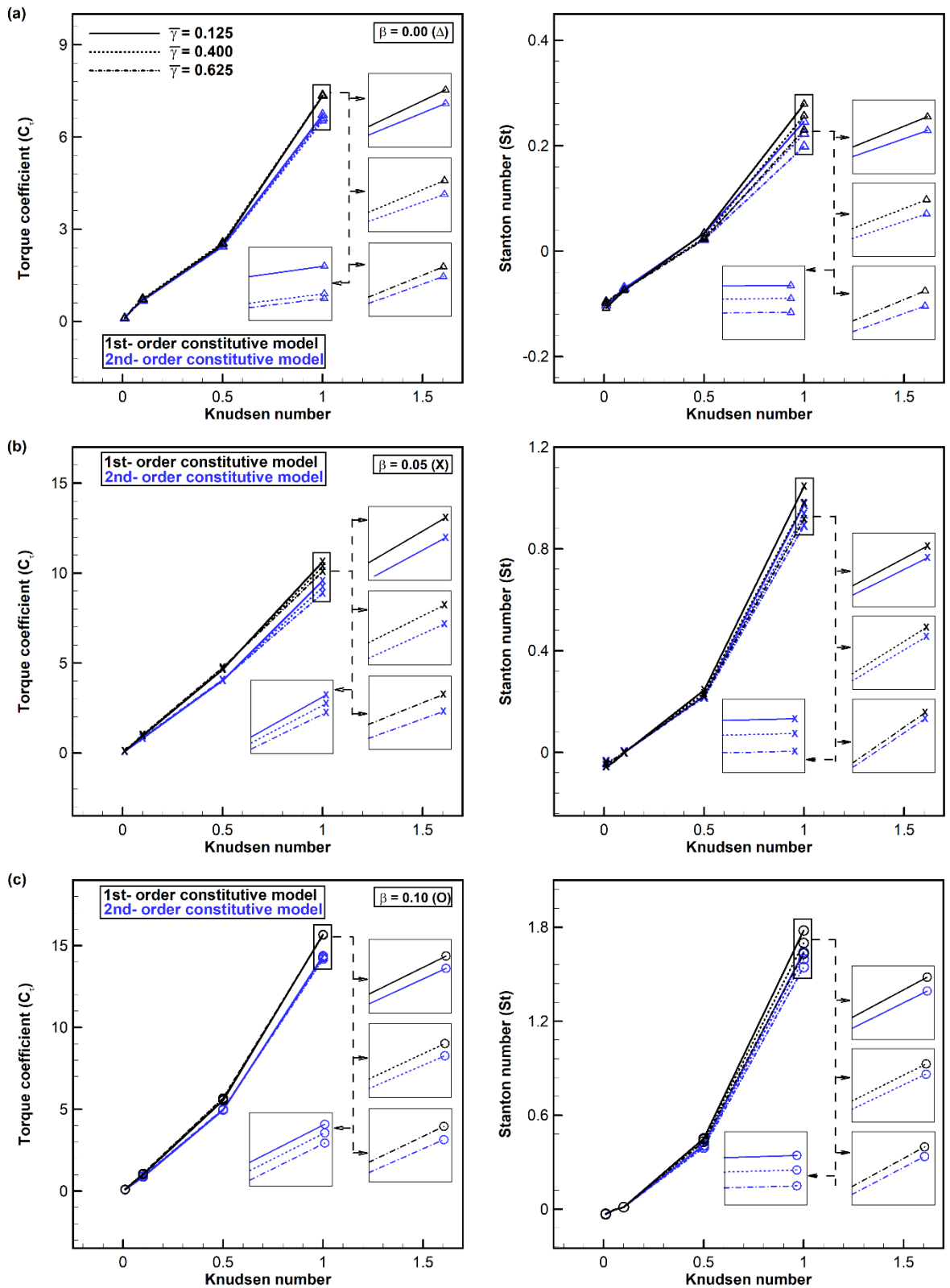


Fig. 19. Trends of integrated quantities of gases ($f_b = 0.0$) with normalized specific heat ratio ($\bar{\gamma} = 0.125, 0.4, 0.625$) for varying Knudsen number: (a) $\beta = 0.0$; (b) $\beta = 0.05$; (c) $\beta =$

0.1.

Figure 19 compares the trends of the integrated quantities (torque coefficient and Stanton number at the inner rotating cylinder) of gases ($f_b = 0.0$) with varying specific heat ratio (0.125, 0.4, 0.625). The torque coefficient decreases slightly with increasing normalized specific heat ratio. Similarly, the Stanton number decreases slightly because of the reduced heat flux. Moreover, as the gases become more rarefied, the torque coefficient and the Stanton number increase significantly, especially in the case of a heated inner wall.

4.4 Real gases: monatomic, diatomic, and polyatomic gases

Thus far, to isolate the effects of the bulk viscosity ratio and the specific heat ratio, their values were selected arbitrarily. However, real gases are known to possess specific combinations of the two values, e.g., argon ($f_b = 0.0, \bar{\gamma} = 0.0$), nitrogen ($f_b = 0.8, \bar{\gamma} = 0.4$), and methane ($f_b = 1.33, \bar{\gamma} = 0.531$). To investigate the thermal and flow characteristics of real gases in CCF, three real gases (monatomic argon, diatomic nitrogen, and polyatomic methane) are considered. The aim is to examine the combined effects of the bulk viscosity ratio and the specific heat ratio of gases in a highly rarefied flow regime.

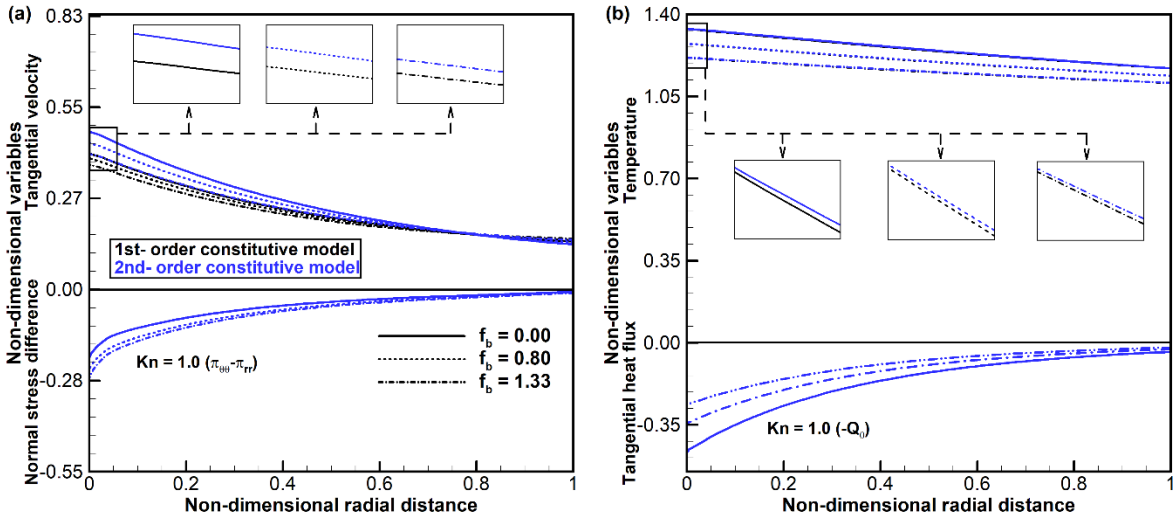


Fig. 20. Profiles of tangential velocity, normal stress difference, temperature, and tangential heat flux of argon ($f_b = 0.0, \bar{\gamma} = 0.0$ or $\gamma = 5/3$), nitrogen ($f_b = 0.8, \bar{\gamma} = 0.4$ or $\gamma = 7/5$), and methane ($f_b = 1.33, \bar{\gamma} = 0.531$ or $\gamma = 1.312$) gases in radial direction at $Kn = 1.0, \beta = 0.0$.

Figure 20 compares the tangential velocity, normal stress difference, temperature, and

tangential heat flux of the three gases in the radial direction at a Knudsen number of 1.0 and no temperature difference ($\beta = 0.0$). From monatomic to diatomic to polyatomic, both the normalized tangential velocity and temperature near the inner cylinder decrease, indicating the dominant role of the specific heat ratio in the velocity and temperature profiles. On the other hand, the normal stress difference ($\Pi_{\theta\theta} - \Pi_{rr}$) increases, while the tangential heat flux Q_θ decreases. This means that the bulk viscosity ratio and the specific heat ratio play a dominant role in the normal stress difference and the tangential heat flux, respectively.

As first explained in Fig. 13, the shear-thinning characteristic of the second-order constitutive model is again responsible for a smaller velocity slip and decrease of the tangential velocity at the inner cylinder, compared to the first-order constitutive model. The same mechanism explains the slight increase in temperature near the inner cylinder.

Figure 21 compares the trends of the integrated quantities (torque coefficient and Stanton number at the inner rotating cylinder) of the three representative gases. From monatomic to diatomic to polyatomic, the torque coefficient and Stanton number decrease. The decrease is amplified with increasing Knudsen number. This trend is the same as that in the case of varying specific heat ratio (Fig. 19) but opposite to that in the case of varying bulk viscosity ratio (Fig. 17). This means that the specific heat ratio plays a more dominant role in the torque coefficient and the Stanton number than does the bulk viscosity ratio. Again, the shear-thinning characteristic of the second-order constitutive model is responsible for the reduced torque and radial heat flux (or Stanton number) at the inner cylinder, compared to the first-order constitutive model.

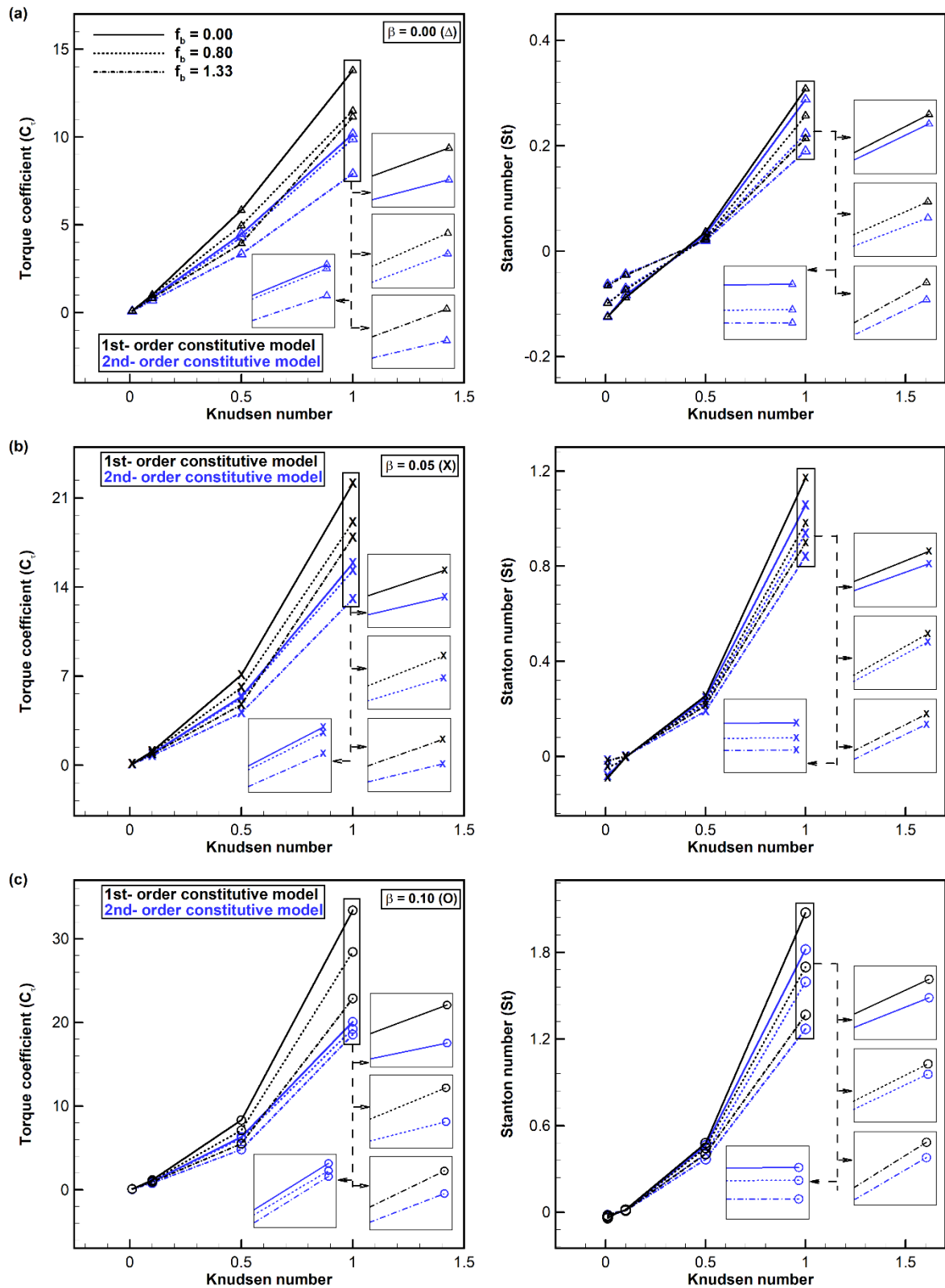


Fig. 21. Trends of integrated quantities of argon ($f_b = 0.0$, $\bar{\gamma} = 0.0$ or $\gamma = 5/3$), nitrogen ($f_b = 0.8$, $\bar{\gamma} = 0.4$ or $\gamma = 7/5$), and methane ($f_b = 1.33$, $\bar{\gamma} = 0.531$ or $\gamma = 1.312$)

gases for varying Knudsen number: (a) $\beta = 0.0$; (b) $\beta = 0.05$; (c) $\beta = 0.1$.

4.5 Summary of thermo-physical characteristics of rarefied and microscale gas flows in cylindrical Couette flow including diatomic and polyatomic gases

In addition to well-known quantities such as the temperature-dependent transport coefficient and accommodation coefficients, focus is given to the effects of the bulk viscosity ratio in combination with the specific heat ratio in CCF in the rarefied and microscale gas regimes. In highly nonequilibrium flow regimes, the thermal and heat transfer characteristics of gas flows become more critical [112-114].

Based on numerical calculations and theoretical results for the second-order constitutive model in one-dimensional CCF in (r, θ) coordinates [Eqs. (47)-(50)], the underlying mechanisms behind several intriguing non-classical properties in gaseous CCF are summarized in Table III.

Table III. Summary of thermal and flow characteristics of nonequilibrium monatomic, diatomic, and polyatomic gases in CCF.

Non-classical behavior	Explanations based on second-order constitutive model	Figures
Smaller velocity slip	<ul style="list-style-type: none"> The shear-thinning property of the second-order constitutive model is responsible for a smaller velocity slip because smaller shear stress for a given shear rate allows for a higher velocity gradient: $\Pi_{r\theta} / \Pi_{r\theta_0} = \left[q^2(c\hat{R}) + (2 - 9f_b)\hat{\Pi}_{r\theta_0}^2 / 3 / q(c\hat{R}) \right]^{-1}.$	7, 13, 18 (a), 20 (a)
Reduced wall shear stress and torque coefficient	<ul style="list-style-type: none"> The shear-thinning property or equivalently the vanishing effective viscosity of the second-order constitutive model in the high Knudsen-number regime is responsible for the reduced wall shear stress and torque coefficient. 	8, 15 (a), 17, 19, 21

Non-zero normal stress	<ul style="list-style-type: none"> The quadratic functional form of the second-order constitutive model is responsible for non-zero normal stress and normal stress difference in states away from thermal equilibrium: $\hat{\Pi}_{\theta\theta} = (-)2\hat{\Pi}_{r\theta_0}^2 / [3q^2(c\hat{R}) + (2 - 9f_b)\hat{\Pi}_{r\theta_0}^2],$ $\hat{\Pi}_{\theta\theta} - \hat{\Pi}_{rr} = 3\hat{\Pi}_{\theta\theta} = -2\hat{\Pi}_{r\theta}\hat{\Pi}_{r\theta_0}.$ <p>In contrast, the first-order constitutive model cannot describe this abnormal property at all because all the second-order coupling effects were ignored from the outset.</p>	13, 20 (a)
Non-zero excess normal stress	<ul style="list-style-type: none"> The direct relationship with the normal stress in the second-order constitutive model is responsible for non-zero excess normal stress: $\Delta = -9f_b\Pi_{\theta\theta} / 2.$ <p>Note that the excess normal stress remains finite in the second-order theory, even if the divergence of velocity vanishes. In contrast, the excess normal stress remains strictly zero in the first-order theory because the divergence of velocity vanishes in CCF.</p>	16
Non-zero tangential heat flux	<ul style="list-style-type: none"> The second-order coupling term is responsible for non-zero tangential heat flux in states away from thermal equilibrium: $\hat{Q}_\theta q(c\hat{R}) = \hat{\Pi}_{r\theta}\hat{Q}_{r_0}.$ <p>In contrast, it remains strictly zero in the case of the first-order constitutive model because the second-order coupling terms were ignored from the outset.</p>	14, 20 (b)
Flattened pressure and density profiles	<ul style="list-style-type: none"> The non-zero viscous normal stress difference with positive sign, $(\Pi_{rr} - \Pi_{\theta\theta}) / r$, which competes with the pressure slope dp/dr, is responsible for the flattened pressure and density profiles. The finite bulk viscosity of diatomic and polyatomic gases further flattens the density and pressure profiles because of the increased normal stress difference. 	6, 16
Reduced heat flux and Stanton number	<ul style="list-style-type: none"> The non-linearity of the second-order constitutive model is responsible for the reduced heat flux and Stanton number: $\hat{Q}_r / \hat{Q}_{r_0} = [1 + 6\hat{\Pi}_{r\theta_0}^2 / q^2(c\hat{R})] / [q(c\hat{R}) + 2\hat{\Pi}_{r\theta_0}^2 / 3 / q(c\hat{R})].$ 	15 (b), 17, 19, 21

5 Conclusions

The main motivation for this study was a recent realization of the increasing importance of thermal physics in monatomic, diatomic, and polyatomic gases in states away from thermal equilibrium, such as rarefied and microscale gas flows. To investigate in detail the role of thermal physics in these gas flows, compressible CCF was selected, because of its fundamental role in the study of fluid dynamics and heat transfer. Even though the geometry is a two-dimensional one, the flow problem is reduced to one-dimension because of the circumferential symmetry, and it is easily testable by experiments using a configuration with high length-to-diameter ratio.

Identified first were four important aspects of physics that might play a critical role in monatomic, diatomic, and polyatomic gases in strong nonequilibrium: (i) the temperature dependence of the transport coefficients in compressible gas flow, (ii) the nonlinearity and coupling in the constitutive relations of gases in strong nonequilibrium, (iii) the bulk viscosity of diatomic and polyatomic gases and its subtle interplay with the nonlinear coupled constitutive relations, and (iv) the temperature jump at a solid wall. As a computational method, the DG method developed previously by the author's research group was used because of its ability to compute low- and high-Mach-number flows with a single framework and its extensibility to handle a three-dimensional configuration of rotating CCF, which can be used in experimental study. The computational method was verified using new analytic solutions for CCF of a compressible gas with the Maxwell slip and Smoluchowski jump conditions including the temperature profile. In addition, the second-order (non-Navier–Fourier) nonlinear coupled constitutive relations (50) were derived for the cylindrical coordinates.

In general, the physical mechanisms behind abnormal behavior were found to be very similar to the Knudsen layer in planar Couette gas flow, and the curvature of the cylindrical geometry did not affect the fundamental physics. For instance, the shear-thinning property of the second-order constitutive model was responsible for a smaller velocity slip. Moreover, the quadratic functional form of the second-order constitutive model was responsible for non-vanishing normal stress and normal stress difference in states away from thermal equilibrium.

However, two new abnormal mechanisms were found in diatomic and polyatomic gases. The first was the subtle interplay of excess normal stress (and bulk viscosity) with the nonlinear

coupled constitutive relations. In the present one-dimensional flow, the divergence of velocity remains strictly zero because the radial velocity is zero and the tangential velocity does not change in the circumferential direction. Consequently, the excess normal stress remains zero in the first-order Navier–Fourier constitutive laws, irrespective of the bulk viscosity. However, through the direct relationship with the normal stress, the excess normal stress remains finite in the second-order theory, even if the divergence of velocity vanishes. Another mechanism was the combined role of the bulk viscosity ratio and the specific heat ratio in diatomic and polyatomic gases. Both ratios played an important role in diatomic and polyatomic gases, but the specific heat ratio played a more dominant role in the torque coefficient and the Stanton number than did the bulk viscosity ratio.

During the present investigation, a subject of debate was identified regarding whether a weak minimum in density indeed exists near the rotating inner cylinder in gaseous CCF in strong nonequilibrium. Because the experiments conducted by Alofs *et al.* in 1971 involved cylinders with low length-to-diameter ratio, it will be necessary to investigate the three-dimensional end effects, and it is hoped that results from studying this problem will be reported in the future.

Acknowledgements

This work was supported by the National Research Foundation of Korea funded by the Ministry of Education, Science and Technology (NRF 2017-R1A5A1015311 and 2017-R1A2B2007634), South Korea.

Appendix: Analytic solutions for cylindrical Couette flow of compressible gas with Maxwell slip and Smoluchowski jump conditions including temperature profile

The conservation laws of momentum and total energy in a steady-state compressible one-dimensional gaseous CCF [Eq. (23)] reduce to the following forms when coupled with the linear Navier–Fourier constitutive laws:

$$-\frac{\rho u_\theta^2}{r} + \frac{dp}{dr} = 0, \quad (\text{A1})$$

$$\frac{1}{r^2} \frac{d}{dr} (r^2 \Pi_{r\theta}) = 0, \text{ where } \Pi_{r\theta} = -\mu r \frac{d}{dr} \left(\frac{u_\theta}{r} \right), \quad (\text{A2})$$

$$r \Pi_{r\theta} \frac{d}{dr} \left(\frac{u_\theta}{r} \right) + \frac{1}{r} \frac{d}{dr} (r Q_r) = 0, \text{ where } Q_r = -k \frac{dT}{dr}. \quad (\text{A3})$$

Note that the excess normal stress Δ vanishes in one-dimensional gaseous CCF when coupled with the linear Navier constitutive law because the divergence of velocity $\partial u_r / \partial r + (1/r) \partial u_\theta / \partial \theta$ vanishes in CCF. These equations yield analytical solutions for the velocity, temperature, pressure, and density fields.

By assuming the transport coefficient μ to be constant, Eq. (A2) reduces to

$$\frac{d}{dr} \left[r^3 \frac{d}{dr} \left(\frac{u_\theta}{r} \right) \right] = 0. \quad (\text{A4})$$

After integrating twice, we obtain the following analytical solution for the velocity field with two undermined constants a and b :

$$u_\theta = ar + \frac{b}{r}. \quad (\text{A5})$$

This velocity profile yields the following shear stress:

$$\Pi_{r\theta} = 2\mu b \frac{1}{r^2}. \quad (\text{A6})$$

The Maxwell slip condition (42) for the gas–surface interactions at the inner and outer cylinders determines the tangential velocity at the wall as follows:

$$u_\theta = u_{\theta_w} - \frac{\omega_M \lambda}{\mu} \Pi_{r\theta} \Big|_w, \text{ where } \omega_M = \frac{2 - \sigma_u}{\sigma_u}. \quad (\text{A7})$$

The tangential velocity at the inner ($r = r_i$) and outer ($r = r_o$) walls reduces to

$$u_{\theta_i} = \Omega_i r_i - \frac{\omega_{M_1} \lambda_1}{\mu} \left[-\mu r \frac{d}{dr} \left(\frac{u_\theta}{r} \right) \right]_{r=r_i}, \quad u_{\theta_o} = \Omega_o r_o + \frac{\omega_{M_2} \lambda_2}{\mu} \left[-\mu r \frac{d}{dr} \left(\frac{u_\theta}{r} \right) \right]_{r=r_o}. \quad (\text{A8})$$

Using the velocity relation (A5), Eq. (A8) can be re-written in terms of non-dimensional variables [20]:

$$u_{\theta_i}^* = 1 - \frac{(1 - \alpha_{M_1}) (\chi^{-1} u_{\theta_i}^* - u_{\theta_o}^*)}{\alpha_{M_1} 2(1 + \chi)}, \quad u_{\theta_o}^* = \chi^{-1} \bar{\Omega} + \frac{(1 - \alpha_{M_2}) (\chi^{-1} u_{\theta_i}^* - u_{\theta_o}^*)}{\alpha_{M_2} 2(1 + \chi)} \chi^2, \quad (\text{A9})$$

where $\chi = \frac{r_i}{r_o}$, $\bar{\Omega} = \frac{\Omega_o}{\Omega_i}$, $u_\theta^* = \frac{u_\theta}{r_i \Omega_i}$, $\text{Kn} = \frac{\lambda}{r_o - r_i}$, and $\alpha_M = \frac{1}{1 + 4\omega_M \text{Kn}}$. By solving Eq. (A9) for u_θ^* , we obtain

$$u_{\theta_i}^* = 1 - (1 - \bar{\Omega}) \chi^{-1} \alpha_{M_2} \frac{(1 - \alpha_{M_1})}{D_M}, \quad (\text{A10})$$

$$u_{\theta_o}^* = \chi^{-1} \left\{ 1 - (1 - \bar{\Omega}) \alpha_{M_2} \frac{[2(1 + \chi) \alpha_{M_1} + \chi^{-1} (1 - \alpha_{M_2})]}{D_M} \right\},$$

where $D_M = 2(1 + \chi) \alpha_{M_1} \alpha_{M_2} + \chi^{-1} \alpha_{M_2} (1 - \alpha_{M_1}) + \chi^2 \alpha_{M_1} (1 - \alpha_{M_2})$. When we further assume $\bar{\Omega} = 0$ and $\alpha_{M_1} = \alpha_{M_2} (= \alpha_M)$, the tangential velocity at the inner and outer walls reduces to

$$u_{\theta_i}^* = \frac{2\alpha_M \chi (1 + \chi) + (1 - \alpha_M) \chi^3}{2\alpha_M \chi (1 + \chi) + (1 - \alpha_M) (1 + \chi^3)}, \quad (\text{A11})$$

$$u_{\theta_o}^* = \frac{(1 - \alpha_M) \chi^2}{2\alpha_M \chi (1 + \chi) - (1 - \alpha_M) (1 + \chi^3)}.$$

By combining Eqs. (A5) and (A11), we can determine the two constants in Eq. (A5) when $\bar{\Omega} = 0$ and $\alpha_{M_1} = \alpha_{M_2} (= \alpha_M)$ as follows:

$$\begin{aligned}
a &= \frac{\Omega_i}{(\chi - \chi^{-1})} \left\{ \frac{\chi^2(1+\chi)[2\alpha_M - (1-\alpha_M)(1-\chi)]}{2\alpha_M\chi(1+\chi) + (1-\alpha_M)(1+\chi^3)} \right\}, \\
b &= -\frac{r_i^2\Omega_i}{(\chi - \chi^{-1})} \left[\frac{2\alpha_M(1+\chi)}{2\alpha_M\chi(1+\chi) + (1-\alpha_M)(1+\chi^3)} \right].
\end{aligned} \tag{A12}$$

On the other hand, the analytical solution for the temperature field can be derived from Eqs. (A3) and (A6):

$$\frac{1}{r} \frac{d(rQ_r)}{dr} = -r\Pi_{r\theta} \frac{d}{dr} \left(\frac{u_\theta}{r} \right) = \frac{4\mu b^2}{r^4}. \tag{A13}$$

By assuming the transport coefficient μ to be constant and integrating Eq. (A13), we obtain

$$Q_r = -\frac{2\mu b^2}{r^3} + \text{constant} \frac{1}{r}. \tag{A14}$$

Upon inserting the linear Fourier law (16) (with constant thermal conductivity k) into Eq. (A14) and integrating once, we obtain

$$T = -\frac{\mu}{k} b^2 \frac{1}{r^2} + c \ln r + d. \tag{A15}$$

Note that the ratio of transport coefficients μ/k is related to Pr, γ , and R . The new constants c and d are determined by applying boundary conditions on the walls as follows:

$$\begin{aligned}
c &= \frac{1}{\ln \chi} \left[T_1 - T_2 - \frac{\mu}{k} b^2 (r_o^{-2} - r_i^{-2}) \right], \\
d &= T_1 + \frac{\mu}{k} b^2 r_i^{-2} + \frac{\ln r_i}{\ln \chi} \left[T_2 - T_1 + \frac{\mu}{k} b^2 (r_o^{-2} - r_i^{-2}) \right].
\end{aligned} \tag{A16}$$

With the constants c and d determined, the radial heat flux (A14) now becomes

$$Q_r = -\frac{2\mu b^2}{r^3} - \frac{c}{r}. \tag{A17}$$

The Smoluchowski jump condition (44) for the gas–surface interactions at the inner and outer cylindrical walls affects the temperature field. The temperature at the walls is given by

$$T = T_w + \omega_T \lambda \left(-\frac{dT}{dr} \right) \Big|_w, \text{ where } \omega_r = \omega_{r_c} \frac{2\gamma}{(\gamma+1)} \frac{1}{\text{Pr}}. \quad (\text{A18})$$

The temperature at the inner ($r = r_i$) and outer ($r = r_o$) walls then becomes

$$T_1 = T_{w_1} + \omega_{T_1} \lambda_1 \frac{1}{k} \left(-\frac{2\mu b^2}{r_i^3} - \frac{c}{r_i} \right), \quad T_2 = T_{w_2} + \omega_{T_2} \lambda_2 \frac{1}{k} \left(-\frac{2\mu b^2}{r_o^3} - \frac{c}{r_o} \right). \quad (\text{A19})$$

If we introduce $\omega_T \lambda = \frac{1-\alpha_T}{4\alpha_T} (r_o - r_i) = \frac{1-\alpha_T}{4\alpha_T} r_i (\chi^{-1} - 1)$ and combine Eqs. (A16) and (A19), they become

$$\begin{aligned} & \left[1 + \frac{(1-\alpha_{T_1})(\chi^{-1}-1)}{\alpha_{T_1} 4 \ln \chi} \right] T_1 - \frac{(1-\alpha_{T_1})(\chi^{-1}-1)}{\alpha_{T_1} 4 \ln \chi} T_2 = T_{w_1} - \\ & \frac{(1-\alpha_{T_1})(\chi^{-1}-1)}{\alpha_{T_1} 4} \frac{\mu}{k} b^2 r_i^{-2} \left[2 - \frac{(\chi^2-1)}{\ln \chi} \right], \\ & \frac{(1-\alpha_{T_2})(1-\chi)}{\alpha_{T_2} 4 \ln \chi} T_1 + \left[1 - \frac{(1-\alpha_{T_2})(1-\chi)}{\alpha_{T_2} 4 \ln \chi} \right] T_2 = T_{w_2} - \\ & \frac{(1-\alpha_{T_2})(1-\chi)}{\alpha_{T_2} 4} \frac{\mu}{k} b^2 r_o^{-2} \left[2 - \frac{(1-\chi^{-2})}{\ln \chi} \right]. \end{aligned} \quad (\text{A20})$$

By solving Eq. (A20) for T_1, T_2 , we obtain

$$\begin{aligned} T_1 &= \frac{1}{D_r} \left\{ B_1 \left[1 - \frac{(1-\alpha_{T_2})(1-\chi)}{\alpha_{T_2} 4 \ln \chi} \right] + B_2 \frac{(1-\alpha_{T_1})(\chi^{-1}-1)}{\alpha_{T_1} 4 \ln \chi} \right\}, \\ T_2 &= \frac{1}{D_r} \left\{ B_2 \left[1 + \frac{(1-\alpha_{T_1})(\chi^{-1}-1)}{\alpha_{T_1} 4 \ln \chi} \right] - B_1 \frac{(1-\alpha_{T_2})(1-\chi)}{\alpha_{T_2} 4 \ln \chi} \right\}, \end{aligned} \quad (\text{A21})$$

where

$$\begin{aligned}
D_T &= \left[1 + \frac{(1-\alpha_{T_1})(\chi^{-1}-1)}{\alpha_{T_1} 4 \ln \chi} \right] \left[1 - \frac{(1-\alpha_{T_2})(1-\chi)}{\alpha_{T_2} 4 \ln \chi} \right] + \frac{(1-\alpha_{T_1})(1-\alpha_{T_2})(\chi^{-1}-1)(1-\chi)}{\alpha_{T_1} \alpha_{T_2} 4 \ln \chi 4 \ln \chi}, \\
B_1 &= T_{w_1} - \frac{(1-\alpha_{T_1})(\chi^{-1}-1)}{\alpha_{T_1} 4} \frac{\mu}{k} b^2 r_i^{-2} \left[2 - \frac{(\chi^2-1)}{\ln \chi} \right], \\
B_2 &= T_{w_2} - \frac{(1-\alpha_{T_2})(1-\chi)}{\alpha_{T_2} 4} \frac{\mu}{k} b^2 r_o^{-2} \left[2 - \frac{(1-\chi^{-2})}{\ln \chi} \right].
\end{aligned}$$

Lastly, the analytical solution for the pressure field can be derived from Eq. (A1) and the equation of state:

$$\frac{dp}{dr} = \frac{p}{RT} \frac{u_\theta^2}{r}. \quad (\text{A22})$$

Using Eqs. (A5) and (A15), we obtain

$$\begin{aligned}
\frac{1}{p} \frac{dp}{dr} &= F(r), \\
F(r) &\equiv \frac{u_\theta^2/r}{RT} = \left(ar + \frac{b}{r} \right)^2 \left/ \left[rR \left(-\frac{\mu}{k} b^2 r^{-2} + c \ln r + d \right) \right] \right. .
\end{aligned} \quad (\text{A23})$$

After integrating once, we obtain

$$p(r) = C \exp \left\{ \int_0^r F(r) dr \right\}. \quad (\text{A24})$$

Alternatively, when we express the pressure profile based on the pressure (p_c) at the center of the channel $\bar{r} = \frac{r_i+r_o}{2}$, we obtain

$$p(r) = p_c \exp \left\{ \int_{\bar{r}}^r F(r) dr \right\}. \quad (\text{A25})$$

The density field is then calculated by the equation of state:

$$\rho(r) = \frac{p_c}{RT(r)} \exp \left\{ \int_{\bar{r}}^r F(r) dr \right\} \text{ where } T(r) = -\frac{\mu}{k} b^2 r^{-2} + c \ln r + d. \quad (\text{A26})$$

Equivalently, the analytical solutions for the pressure and density fields can be derived based

on the initial average steady-state density (or the initial uniform experimental density) given by [21]

$$\langle \rho(r) \rangle = \rho_{initial} = \frac{2\pi \int_{r_i}^{r_o} r \rho dr}{\pi (r_o^2 - r_i^2)}. \quad (A27)$$

Note that the mass of gas between the two cylinders is conserved in time. From Eq. (A24) and the equation of state, we obtain

$$\rho(r) = \frac{C \exp\left\{\int_0^r F(r) dr\right\}}{RT(r)}. \quad (A28)$$

By combining Eqs. (A27) and (A28), we derive

$$\rho(r) = \langle \rho \rangle \frac{(r_o^2 - r_i^2)/2}{T(r)} \exp\left\{\int_0^r F(r) dr\right\} \left[\int_{r_i}^{r_o} \left\{ \frac{r}{T(r)} \exp\left\{\int_0^r F(r) dr\right\} \right\} dr \right]^{-1}. \quad (A29)$$

The present analytical solutions for the temperature, pressure, and density fields are believed to be new.

REFERENCES

- [1] F. Völklein, M. Grau, A. Meier, G. Hemer, L. Breuer, P. Woias, Optimized MEMS Pirani sensor with increased pressure measurement sensitivity in the fine and high vacuum regime, *Journal of Vacuum Science & Technology A: Vacuum, Surfaces, and Films*, 31(6) (2013) 061604.
- [2] R. Ellefson, A. Miiller, Recommended practice for calibrating vacuum gauges of the thermal conductivity type, *Journal of Vacuum Science & Technology A: Vacuum, Surfaces, and Films*, 18(5) (2000) 2568-2577.
- [3] H. Xiao, Q.J. He, Aero-heating in hypersonic continuum and rarefied gas flows, *Aerospace Science and Technology*, 82 (2018) 566-574.
- [4] J. Wang, Y. Li, X. Liu, C. Shen, H. Zhang, K. Xiong, Recent active thermal management technologies for the development of energy-optimized aerospace vehicles in China, *Chinese Journal of Aeronautics*, (2020).
- [5] S.-J. Chen, Y.-C. Wu, A new macro-model of gas flow and parameter extraction for a CMOS-MEMS vacuum sensor, *Symmetry*, 12(10) (2020) 1604.
- [6] G. Tunc, Y. Bayazitoglu, Heat transfer in microtubes with viscous dissipation, *International Journal of Heat and Mass Transfer*, 44(13) (2001) 2395-2403.
- [7] D.J. Alofs, G.S. Springer, Cylindrical Couette flow experiments in the transition regime, *The Physics of Fluids*, 14(2) (1971) 298-305.
- [8] C. Tantos, D. Valougeorgis, M. Pannuzzo, A., Frezzotti, G.L. Morini, Conductive heat transfer in a rarefied polyatomic gas confined between coaxial cylinders, *International Journal of Heat and Mass Transfer*, 79 (2014) 378-389.
- [9] A. D'Orazio, A. Karimipour, A useful case study to develop lattice Boltzmann method performance: gravity effects on slip velocity and temperature profiles of an air flow inside a microchannel under a constant heat flux boundary condition, *International Journal of Heat and Mass Transfer*, 136 (2019) 1017-1029.
- [10] W.P. Teagan, G.S. Springer, Heat-transfer and density-distribution measurements between parallel plates in the transition regime, *The Physics of Fluids*, 11(3) (1968) 497-506.
- [11] S. Naris, D. Valougeorgis, The driven cavity flow over the whole range of the Knudsen number, *Physics of Fluids*, 17(9) (2005) 097106.
- [12] S. Chadha, R. Jefferson-Loveday, T. Hussain, Modelling Knudsen number effects in suspension high velocity oxy fuel thermal spray, *International Journal of Heat and Mass Transfer*, 152 (2020) 119454.
- [13] K. Farber, P. Farber, J. Gräbel, S. Krick, J. Reitz, P. Ueberholz, A hybrid Navier-Stokes/DSMC simulation for rarefied gas flow for the deposition of nano layers for OLEDs, in: *AIP Conference Proceedings*, AIP Publishing LLC, 2015, pp. 030017.
- [14] R.S. Myong, Theoretical description of the gaseous Knudsen layer in Couette flow based on the second-order constitutive and slip-jump models, *Physics of Fluids*, 28(1) (2016) 012002.
- [15] A. Rostami, A.S. Mujumdar, N. Saniei, Flow and heat transfer for gas flowing in microchannels: a review, *Heat and Mass Transfer*, 38(4-5) (2002) 359-367.
- [16] Y. Jung, Velocity inversion in nanochannel flow, *Physical Review E*, 75(5) (2007) 051203.

- [17] R.S. Myong, A full analytical solution for the force-driven compressible Poiseuille gas flow based on a nonlinear coupled constitutive relation, *Physics of Fluids*, 23(1) (2011) 012002.
- [18] A. Rana, R. Ravichandran, J.H. Park, R.S. Myong, Microscopic molecular dynamics characterization of the second-order non-Navier-Fourier constitutive laws in the Poiseuille gas flow, *Physics of Fluids*, 28(8) (2016) 082003.
- [19] H. Gijare, A. Bhagat, N. Dongari, Effect of Knudsen layer on the heat transfer in hypersonic rarefied gas flows, *International Journal of Thermal Sciences*, 142 (2019) 134-141.
- [20] R.S. Myong, J.M. Reese, R.W. Barber, D.R. Emerson, Velocity slip in microscale cylindrical Couette flow: the Langmuir model, *Physics of Fluids*, 17(8) (2005) 087105.
- [21] R. Khayat, B.C. Eu, Nonlinear transport processes and fluid dynamics: Cylindrical Couette flow of Lennard-Jones fluids, *Physical Review A*, 38(5) (1988) 2492.
- [22] M. Fardin, C. Perge, N. Taberlet, “The hydrogen atom of fluid dynamics”—introduction to the Taylor–Couette flow for soft matter scientists, *Soft Matter*, 10(20) (2014) 3523-3535.
- [23] K.W. Tibbs, F. Baras, A.L. Garcia, Anomalous flow profile due to the curvature effect on slip length, *Physical Review E*, 56(2) (1997) 2282.
- [24] R. Barber, D. Emerson, The influence of Knudsen number on the hydrodynamic development length within parallel plate micro-channels, *WIT Transactions on Engineering Sciences*, 36 (2002).
- [25] S. Yuhong, R.W. Barber, D.R. Emerson, Inverted velocity profiles in rarefied cylindrical Couette gas flow and the impact of the accommodation coefficient, *Physics of Fluids*, 17(4) (2005) 047102.
- [26] N. Dongari, R.W. Barber, D.R. Emerson, S.K. Stefanov, Y. Zhang, J.M. Reese, The effect of Knudsen layers on rarefied cylindrical Couette gas flows, *Microfluidics and Nanofluidics*, 14 (2013) 31-43.
- [27] Z. Guo, B. Shi, C. Zheng, Velocity inversion of micro cylindrical Couette flow: A lattice Boltzmann study, *Computers & Mathematics with Applications*, 61(12) (2011) 3519-3527.
- [28] N. Dongari, C. White, T.J. Scanlon, Y. Zhang, J.M. Reese, Effects of curvature on rarefied gas flows between rotating concentric cylinders, *Physics of Fluids*, 25(5) (2013) 052003.
- [29] H. Akhlaghi, K. Javadi, Torque data on non-isothermal rarefied cylindrical Couette flow, *Vacuum*, 121 (2015) 56-63.
- [30] A. Abramov, V.Y. Alexandrov, A.V. Butkovskii, The longitudinal cylindrical Couette problem for rarefied gas: Energy fluxes maximums, *International Journal of Heat and Mass Transfer*, 111 (2017) 608-613.
- [31] A. Abramov, V.Y. Alexandrov, A.V. Butkovskii, Rarefied cylindrical Couette flow: Shear stress and energy flux maxima, *International Journal of Heat and Mass Transfer*, 123 (2018) 192-200.
- [32] K. Nanbu, Analysis of cylindrical Couette flows by use of the direction simulation method, *The Physics of fluids*, 27(11) (1984) 2632-2635.
- [33] C. Cercignani, F. Sernagiotto, Cylindrical Couette flow of a rarefied gas, *The Physics of Fluids*, 10(6) (1967) 1200-1204.
- [34] M. Torrilhon, Modeling nonequilibrium gas flow based on moment equations, *Annual Review of Fluid Mechanics*, 48 (2016) 429-458.

- [35] W. Su, P. Wang, H. Liu, L. Wu, Accurate and efficient computation of the Boltzmann equation for Couette flow: Influence of intermolecular potentials on Knudsen layer function and viscous slip coefficient, *Journal of Computational Physics*, 378 (2019) 573-590.
- [36] H. Akhlaghi, E. Roohi, Generalized description of the Knudsen layer thickness in rarefied gas flows, *Physics of Fluids*, 33(6) (2021) 061701.
- [37] B. Goshayeshi, E. Roohi, S. Stefanov, DSMC simulation of hypersonic flows using an improved SBT-TAS technique, *Journal of Computational Physics*, 303 (2015) 28-44.
- [38] A. Amiri-Jaghargh, E. Roohi, H. Niazmand, S. Stefanov, DSMC simulation of low Knudsen micro/nanoflows using small number of particles per cells, *Journal of Heat Transfer*, 135(10) (2013).
- [39] A. Lotfian, E. Roohi, Radiometric flow in periodically patterned channels: Fluid physics and improved configurations, *Journal of Fluid Mechanics*, 860 (2019) 544-576.
- [40] E. Roohi, S. Stefanov, A. Shoja-Sani, H. Ejraei, A generalized form of the Bernoulli Trial collision scheme in DSMC: Derivation and evaluation, *Journal of Computational Physics*, 354 (2018) 476-492.
- [41] J.C. Maxwell, On stresses in rarefied gases arising from inequalities of temperature, *Proceedings of the Royal Society of London*, 27(185-189) (1878) 304-308.
- [42] R.S. Myong, Gaseous slip models based on the Langmuir adsorption isotherm, *Physics of Fluids*, 16(1) (2004) 104-117.
- [43] V.S. Smoluchowski, Ueber wärmeleitung in verdünnten gasen, *Annalen der Physik*, 300(1) (1898) 101-130.
- [44] N.T.P. Le, N.H. Tran, T.N. Tran, Modified Patterson temperature jump condition considering viscous heat generation, *International Journal of Heat and Mass Transfer*, 126 (2018) 1267-1274.
- [45] K.K. Kammara, R. Kumar, Development of empirical relationships for surface accommodation coefficients through investigation of nano-poiseuille flows using molecular dynamics method, *Microfluidics and Nanofluidics*, 24(9) (2020) 1-14.
- [46] T.P.L. Nam, C. White, J.M. Reese, R.S. Myong, Langmuir–Maxwell and Langmuir–Smoluchowski boundary conditions for thermal gas flow simulations in hypersonic aerodynamics, *International Journal of Heat and Mass Transfer*, 55(19-20) (2012) 5032-5043.
- [47] R.S. Myong, Thermodynamically consistent hydrodynamic computational models for high-Knudsen-number gas flows, *Physics of Fluids*, 11(9) (1999) 2788-2802.
- [48] Z. Jiang, W. Chen, W. Zhao, Numerical analysis of the micro-Couette flow using a non-Newton–Fourier model with enhanced wall boundary conditions, *Microfluidics and Nanofluidics*, 22(1) (2018) 10.
- [49] Z. He, Z. Jiang, H. Zhang, W. Chen, Analytical method of nonlinear coupled constitutive relations for rarefied non-equilibrium flows, *Chinese Journal of Aeronautics*, 34(2) (2021) 136-153.
- [50] Z. Jiang, W. Zhao, Z. Yuan, W. Chen, R.S. Myong, Computation of hypersonic flows over flying configurations using a nonlinear constitutive model, *AIAA Journal*, 57(12) (2019) 5252-5268.
- [51] Z. Yuan, W. Zhao, Z. Jiang, W. Chen, Numerical simulation of hypersonic reaction flows with nonlinear coupled constitutive relations, *Aerospace Science and Technology*, 112 (2021) 106591.
- [52] Z. Jiang, W. Zhao, W. Chen, R.K. Agarwal, Computation of shock wave structure using a simpler set of generalized hydrodynamic equations based on nonlinear coupled constitutive relations, *Shock*

Waves, 29(8) (2019) 1227-1239.

[53] Z. Jiang, W. Zhao, W. Chen, R.K. Agarwal, An undecomposed hybrid algorithm for nonlinear coupled constitutive relations of rarefied gas dynamics, *Commun. Comput. Phys.*, 26 (2019) 880.

[54] M. Torrilhon, Modeling nonequilibrium gas flow based on moment equations, *Annual review of fluid mechanics*, 48 (2016) 429-458.

[55] T.F. Morse, Kinetic model for gases with internal degrees of freedom, *The Physics of Fluids*, 7(2) (1964) 159-169.

[56] L.H. Holway Jr, New statistical models for kinetic theory: methods of construction, *The Physics of Fluids*, 9(9) (1966) 1658-1673.

[57] F.B. Hanson, T.F. Morse, Kinetic models for a gas with internal structure, *The Physics of Fluids*, 10(2) (1967) 345-353.

[58] S.K. Hsu, T.F. Morse, Kinetic theory of parallel plate heat transfer in a polyatomic gas, *The Physics of Fluids*, 15(4) (1972) 584-591.

[59] N. Pazooki, S.K. Loyalka, Heat transfer in a rarefied polyatomic gas—I. Plane parallel plates, *International Journal of Heat and Mass Transfer*, 28(11) (1985) 2019-2027.

[60] V.A. Rykov, A model kinetic equation for a gas with rotational degrees of freedom, *Fluid Dynamics*, 10(6) (1975) 959-966.

[61] C. Tantos, G.P. Ghiroldi, D. Valougeorgis, A. Frezzotti, Effect of vibrational degrees of freedom on the heat transfer in polyatomic gases confined between parallel plates, *International Journal of Heat and Mass Transfer*, 102 (2016) 162-173.

[62] C. Tantos, D. Valougeorgis, A. Frezzotti, Conductive heat transfer in rarefied polyatomic gases confined between parallel plates via various kinetic models and the DSMC method, *International Journal of Heat and Mass Transfer*, 88 (2015) 636-651.

[63] C. Tantos, D. Valougeorgis, Conductive heat transfer in rarefied binary gas mixtures confined between parallel plates based on kinetic modeling, *International Journal of Heat and Mass Transfer*, 117 (2018) 846-860.

[64] P.F. Hwang, A kinetic theory description of rarefied gas flows with the effect of rotational relaxation, Georgia Institute of Technology, USA, 1971.

[65] I.N. Larina, V.A. Rykov, Boundary conditions for gases on a body surface, *Fluid Dynamics*, 21(5) (1986) 795-801.

[66] H. Chalabi, O. Buchina, L. Saraceno, M. Lorenzini, D. Valougeorgis, G.L. Morini, Experimental analysis of heat transfer between a heated wire and a rarefied gas in an annular gap with high diameter ratio, in: *Journal of Physics: Conference Series*, IOP Publishing, 2012, pp. 012028.

[67] Y.G. Semyonov, S.F. Borisov, P.E. Suetin, Investigation of heat transfer in rarefied gases over a wide range of Knudsen numbers, *International Journal of Heat and Mass transfer*, 27(10) (1984) 1789-1799.

[68] C.F. Curtiss, The classical Boltzmann equation of a gas of diatomic molecules, *The Journal of Chemical Physics*, 75(1) (1981) 376-378.

[69] B.C. Eu, Y.G. Ohr, Generalized hydrodynamics, bulk viscosity, and sound wave absorption and dispersion in dilute rigid molecular gases, *Physics of Fluids*, 13(3) (2001) 744-753.

- [70] R.S. Myong, A generalized hydrodynamic computational model for rarefied and microscale diatomic gas flows, *Journal of Computational Physics*, 195(2) (2004) 655-676.
- [71] R.S. Myong, On the high Mach number shock structure singularity caused by overreach of Maxwellian molecules, *Physics of Fluids*, 26(5) (2014) 056102.
- [72] H. Xiao, R.S. Myong, Computational simulations of microscale shock–vortex interaction using a mixed discontinuous galerkin method, *Computers & Fluids*, 105 (2014) 179-193.
- [73] N.T.P. Le, H. Xiao, R.S. Myong, A triangular discontinuous Galerkin method for non-Newtonian implicit constitutive models of rarefied and microscale gases, *Journal of Computational Physics*, 273 (2014) 160-184.
- [74] B.Q. Li, *Discontinuous finite elements in fluid dynamics and heat transfer*, Springer Science & Business Media, 2006.
- [75] F. Bassi, S. Rebay, A high-order accurate discontinuous finite element method for the numerical solution of the compressible Navier–Stokes equations, *Journal of Computational Physics*, 131(2) (1997) 267-279.
- [76] S. Singh, R.S. Myong, A computational study of bulk viscosity effects on shock-vortex interaction using discontinuous Galerkin method, *Journal of Computational Fluids Engineering*, 22(2) (2017) 86-95.
- [77] S. Singh, A. Karchani, R.S. Myong, Non-equilibrium effects of diatomic and polyatomic gases on the shock-vortex interaction based on the second-order constitutive model of the Boltzmann-Curtiss equation, *Physics of Fluids*, 30(1) (2018) 016109.
- [78] H.-S. Tsien, Superaerodynamics, mechanics of rarefied gases, *Journal of the Aeronautical Sciences*, 13(12) (1946) 653-664.
- [79] S. Singh, Development of a 3D discontinuous Galerkin method for the second-order Boltzmann-Curtiss based hydrodynamic models of diatomic and polyatomic gases, Ph.D. Thesis, Gyeongsang National University, South Korea, 2018,02.
- [80] L.P. Raj, S. Singh, A. Karchani, R.S. Myong, A super-parallel mixed explicit discontinuous Galerkin method for the second-order Boltzmann-based constitutive models of rarefied and microscale gases, *Computers & Fluids*, 157 (2017) 146-163.
- [81] R.S. Myong, A computational method for Eu's generalized hydrodynamic equations of rarefied and microscale gasdynamics, *Journal of Computational Physics*, 168(1) (2001) 47-72.
- [82] B.C. Eu, *Kinetic theory and irreversible thermodynamics*, in, Wiley-Interscience, 1992.
- [83] M.S. Cramer, Numerical estimates for the bulk viscosity of ideal gases, *Physics of fluids*, 24(6) (2012) 066102.
- [84] B.C. Eu, A modified moment method and irreversible thermodynamics, *The Journal of Chemical Physics*, 73(6) (1980) 2958-2969.
- [85] H. Grad, On the kinetic theory of rarefied gases, *Communications on Pure and Applied Mathematics*, 2(4) (1949) 331-407.
- [86] S. Singh, A. Karchani, T. Chourushi, R.S. Myong, A three-dimensional modal discontinuous Galerkin method for the second-order Boltzmann-Curtiss-based constitutive model of rarefied and microscale gas flows, In Review.

- [87] S. Chapman, T.G. Cowling, D. Burnett, *The mathematical theory of non-uniform gases: an account of the kinetic theory of viscosity, thermal conduction and diffusion in gases*, Cambridge university press, 1990.
- [88] S. Singh, A. Karchani, K. Sharma, R.S. Myong, Topology of the second-order constitutive model based on the Boltzmann–Curtiss kinetic equation for diatomic and polyatomic gases, *Physics of Fluids*, 32(2) (2020) 026104.
- [89] H.-T. Yang, L. Lester, Plane Couette flow at low Mach number according to the kinetic theory of gases, GALCIT Hypersonic Research Project, Memorandum No. 36 (1957).
- [90] J.D. Anderson Jr, *Hypersonic and High-temperature Gas Dynamics*, American Institute of Aeronautics and Astronautics, 2006.
- [91] T. Chourushi, A. Rahimi, S. Singh, R.S. Myong, Computational simulations of near-continuum gas flow using Navier-Stokes-Fourier equations with slip and jump conditions based on the modal discontinuous Galerkin method, *Advances in Aerodynamics*, 2 (2020) 1-37.
- [92] M. Dubiner, Spectral methods on triangles and other domains, *Journal of Scientific Computing*, 6(4) (1991) 345-390.
- [93] G. Karniadakis, S. Sherwin, *Spectral/hp Element Methods for Computational Fluid Dynamics*, Oxford University Press, 2013.
- [94] S. Singh, M. Battiato, Strongly out-of-equilibrium simulations for electron Boltzmann transport equation using modal discontinuous Galerkin approach, *International Journal of Applied and Computational Mathematics*, 6(5) (2020) 133.
- [95] B. Cockburn, Shu C-W, The Runge–Kutta discontinuous Galerkin method for conservation laws V: multidimensional systems, *Journal of Computational Physics*, 141(2) (1998) 199-224.
- [96] R.S. Myong, D.A. Lockerby, J.M. Reese, The effect of gaseous slip on microscale heat transfer: An extended Graetz problem, *International Journal of Heat and Mass Transfer*, 49(15-16) (2006) 2502-2513.
- [97] W.-M. Zhang, G. Meng, X. Wei, A review on slip models for gas microflows, *Microfluidics and Nanofluidics*, 13(6) (2012) 845-882.
- [98] W. Song, J. Yao, Y. Li, H. Sun, Y. Yang, Fractal models for gas slippage factor in porous media considering second-order slip and surface adsorption, *International Journal of Heat and Mass Transfer*, 118 (2018) 948-960.
- [99] Z. Liehui, S. Baochao, Z. Yulong, G. Zhaoli, Review of micro seepage mechanisms in shale gas reservoirs, *International Journal of Heat and Mass Transfer*, 139 (2019) 144-179.
- [100] L. Zhang, B. Shan, Y. Zhao, J. Du, J. Chen, X. Tao, Gas transport model in organic shale nanopores considering Langmuir slip conditions and diffusion: Pore confinement, real gas, and geomechanical effects, *Energies*, 11(1) (2018) 223.
- [101] T. Huang, L. Cao, C. Yuan, P. Chen, A novel numerical model of gas transport in multiscale shale gas reservoirs with considering surface diffusion and Langmuir slip conditions, *Energy Science & Engineering*, 7(4) (2019) 1315-1332.
- [102] E.H. Kennard, *Kinetic Theory of Gases with an Introduction to Statistical Mechanics*, McGraw-Hill, London, 1938.
- [103] T. Chourushi, S. Singh, R.S. Myong, Computational study of rarefied flow inside a lid driven

cavity using a mixed modal discontinuous galerkin method, *Journal of Computational Fluids Engineering*, 23(3) (2018) 62-71.

[104] O. Ejtehadi, A. Rahimi, A. Karchani, R.S. Myong, Complex wave patterns in dilute gas–particle flows based on a novel discontinuous Galerkin scheme, *International Journal of Multiphase Flow*, 104 (2018) 125-151.

[105] O. Ejtehadi, A. Rahimi, R.S. Myong, Investigation of a trifold interaction mechanism of shock, vortex, and dust using a DG method in a two-fluid model framework, *Powder Technology*, 374 (2020) 121-138.

[106] R.S. Myong, A. Karchani, O. Ejtehadi, A review and perspective on a convergence analysis of the direct simulation Monte Carlo and solution verification, *Physics of Fluids*, 31(6) (2019) 066101.

[107] N.T.P. Le, E. Roohi, A new form of the second order temperature jump boundary condition in the low-speed nano/microscale and hypersonic rarefied gas flow simulations, *International Journal of Thermal Science*, 89 (2015) 51-59.

[108] N.T.P. Le, E. Roohi, T.N. Tran, Comprehensive assessment of newly-developed slip-jump boundary conditions in high-speed rarefied gas flow simulations, *Aerospace Science and Technology*, 91 (2019) 656-668.

[109] M.A. Gallis, J.R. Torczynski, D.J. Rader, M. Tij, A. Santos, Normal solutions of the Boltzmann equation for highly nonequilibrium Fourier flow and Couette flow, *Physics of Fluids*, 18(1) (2006) 017104.

[110] J. Lin, C. Scalo, L. Hesselink, Bulk viscosity model for near-equilibrium acoustic wave attenuation, *arXiv preprint arXiv:1707.05876*, (2017).

[111] G.G. Stokes, On the theories of the internal friction of fluids in motion, and of the equilibrium and motion of elastic solids, *Transactions of the Cambridge Philosophical Society*, 8 (1880).

[112] O. Ejtehadi, E. Roohi, J.A. Esfahani, Investigation of basic molecular gas structural effects on hydrodynamics and thermal behaviors of rarefied shear driven micro/nano flow using DSMC, *International Communications in Heat and Mass Transfer*, 39(3) (2012) 439-448.

[113] T.K. Mankodi, U.V. Bhandarkar, R.S. Myong, Collision cross sections and nonequilibrium viscosity coefficients of N₂ and O₂ based on molecular dynamics, *Physics of Fluids*, 32(3) (2020) 036102.

[114] T.K. Mankodi, R.S. Myong, Boltzmann-based second-order constitutive models of diatomic and polyatomic gases including the vibrational mode, *Physics of Fluids*, 32(12) (2020) 126109.